ULTIMATE LOAD CAPACITY OF CAISSON FOUNDATIONS AND ANCHORS IN SAND

A Dissertation

by

ANAS SULIMAN M ALDAWWAS

Submitted to the Graduate and Professional School of
Texas A&M University
in partial fulfillment of the requirements for the degree of

DOCTOR OF PHILOSOPHY

Chair of Committee,	Charles P. Aubeny
Committee Members,	Robert Lytton
	Marcelo Sanchez
	Alan Palazzolo
Head of Department,	Zachary Grasley

May 2022

Major Subject: Civil Engineering

ABSTRACT

Caisson foundation is a promising alternative and a primary anchoring candidate for offshore floating wind turbine. Although suction caisson is a common foundation solution that has been used in the oil and gas industry, its application in offshore floating wind turbine differs significantly in terms of the anchor aspect ratio, load magnitude, and soil type.

Most of the practical experience from the oil and gas industry and studies in the literature have largely focused on caissons capacity in cohesive soils.

In this study, a three-dimensional finite element model is developed to estimate the capacity of caisson anchors in sand where the drained condition is of prime importance. After the model is validated by comparing its results to measured data from centrifuge tests, the model then is utilized in the scope of a parametric study to investigate the effect of load attachment depth (L_i), Load inclination angle (θ), aspect ratio and soil relative density (D_r). Mohr-coulomb constitutive model has been the primary model that is used to model the soil in this study and two of its parameters friction angle (ϕ) and dilation angle(ψ) have been assessed to evaluate their effect on the ultimate capacity and failure behavior.

A simplified method using an upper bound formulation of plasticity limit analysis is proposed to estimate the lateral load capacity of suction anchor in sand. The plastic limit analysis model offers a quick estimate of lateral load capacity for the caisson anchor, and it provides an uncomplicated way to assess the effect of key parameters on the caisson anchor capacity. In addition to the main project, two projects are considered in this study. First project is the lateral capacity of multiline ring anchor in sand. The second project is bucket foundation under high moment demands for fixed foundation offshore wind towers.

ACKNOWLEDGEMENTS

I am extremely grateful to my supervisor Dr. Charles Aubeny, without whom I would not have been able to complete this research. I was really privileged to have the opportunity to work under his supervision so I would like to thank him for his invaluable advice, continuous support, and patience during my graduate study. Also, I want to thank him for introducing me to this field the field of offshore geotechnics where his immense knowledge and plentiful experience of the field have steered and motivated me through this research.

Also, I would like to express my deep appreciation and gratitude to Dr. Robert L. Lytton, Dr. Marcelo Sanchez, and Dr. Alan Palazzolo for contributing as members of my committee and for their guidance and support throughout the course of this research.

To my friends and colleagues at Dwight Look Engineering Building thank you for the stimulating conversations and welcomed distractions to rest my mind outside of my research.

I would like to thank the High-Performance Research Computing (HPRC) center for providing me with the necessary computing power to perform numerical simulations.

Finally, I want to thank my parents Sulaiman and Hessa for their unwavering support and belief in me.

CONTRIBUTORS AND FUNDING SOURCES

This work was supervised by a dissertation committee consisting of the following:

• Dr. Charles P. Aubeny, Professor, Zachry Department of Civil and Environmental Engineering, Texas A&M University, College Station, Texas, USA [Chair],

• Dr. Marcelo Sanchez, Professor Zachry Department of Civil and Environmental Engineering, Texas A&M University, College Station, Texas, USA [Member],

• Dr. Robert L. Lytton, Professor Zachry Department of Civil and Environmental Engineering, Texas A&M University, College Station, Texas, USA [Member],

• Dr. Alan Palazzolo, Professor, J. Mike Walker '66 Department of Mechanical Engineering, Texas A&M University, College Station, Texas, USA [Member].

All the work conducted for this dissertation was completed independently by the student. Graduate study was partially supported by SACM.

TABLE OF CONTENTS

Page

LIST OF FIGURES

Page

LIST OF TABLES

Page

CHAPTER I

INTRODUCTION

1.1 Background

As part of Net-Zero goals and energy transition objectives, offshore wind projects are expanding in the United States and around the world. Floating offshore wind (FOWT) in particular has enormous potential to be the next wave in renewable energy since most of the United States offshore wind resources are in deep waters. in the context of renewable energy development, deep water can be defined by water depths greater than 60 meters which is approximately the limit for fixed-bottom system in which the technology can still be feasible. The majority of the existing offshore wind turbine projects utilize a fixed-bottom system where they are built in water depths less than 60 meters. The fixed-bottom technology is more mature than the floating offshore wind technology, Figure 1.1 shows different foundation types for fixed-bottom system. In 2018, the typical turbine size was 6.8 Megawatt while in 2021 GE introduced the 12-Megawatt Haliade-X offshore wind turbine to market (Gaertner *et al*., 2020). Offshore wind turbine size will continue to increase because larger turbines yield more energy at a lower rate.

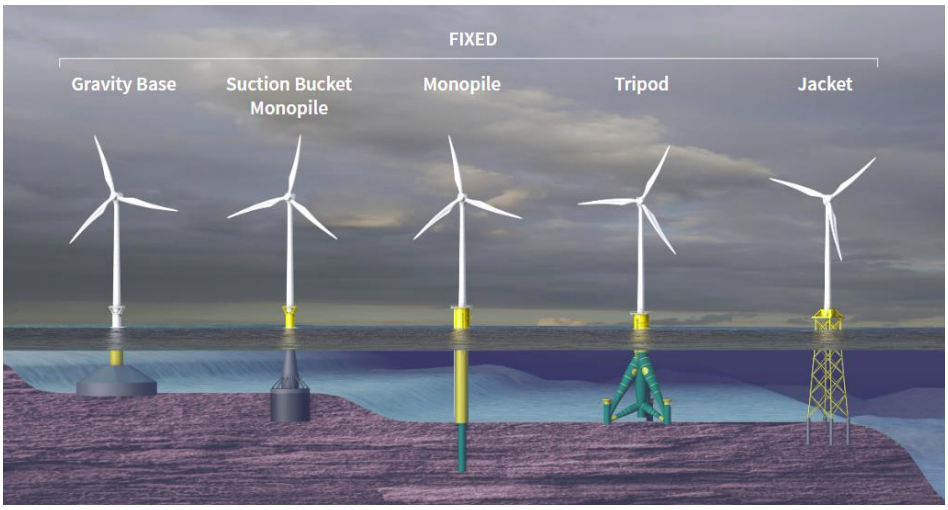

Figure 1.1: Fixed wind foundation types. Reprinted from [US Department of Energy, 2015]

Floating offshore wind turbines (FOWT) can be installed farther offshore where wind speed tends to be faster and steadier. The technology is still in a precommercial phase, a report from National Renewable Energy Laboratory (NREL) shows at the end of 2019 the total installed FOWTs is around 84 megawatts. Worldwide there are over 7 GW in planning and permitting phases of development, with the first commercial-scale projects anticipated to be operational in 2024 (Beiter et al., 2020).

The levelized cost of energy (LCOE) for the floating offshore wind is currently higher than that of onshore and nearshore fixed-bottom wind turbine projects. However, LCOE for fixed-bottom technology has not been always that low, but it has undergone significant reduction since 2014 with the rapid evolution in the technology. The emerging floating offshore technology is expected to experience similar trends with research projects focusing on optimizing all aspects of the new technology. The foundation system cost is a main component of the overall cost thus more research is needed to help optimize the design, fabrication, and installation processes to accelerate the cost reduction of the technology.

FOWTs have a foundation system that includes a floating platform and an anchor system connecting to the seabed using mooring lines. Spar floater, tension leg platform and semi-submersible foundation are main types of offshore floating structures, as shown in Figure 1.2. Caisson foundations are a desirable option for offshore wind turbines, with many advantages including a quick installation process and easy decommissioning in addition to its applicability to deeper waters, as well as larger turbines (Wang et al., 2018).

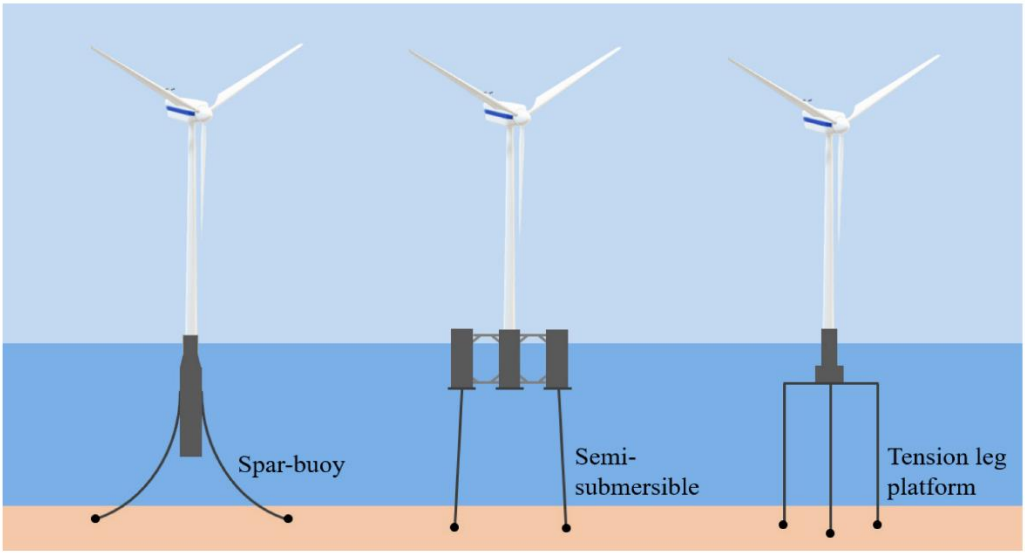

Figure 1.2: Floating offshore wind types. Reprinted from [Jung et al, 2021]

Most of the practical experience in the literature comes from the oil and gas industry and these studies have largely focused on caisson capacity in cohesive soils. Many researchers examined the effect of aspect ratio, pad-eye location, and load inclination angle of caisson foundation in clay (Aubeny et al. 2001; Randolph and House 2002; Aubeny et al. 2003; Clukey et al. 2003) . However, that is not the case for caisson foundations in sands, for which information in the published literature is more limited.

The unexploited offshore wind resources in deep waters make FOWTs technology a primary choice for renewable energy. However, the high LCOE for the technology needs to undergo significant reduction to be commercially competitive. Some new innovative anchoring solutions have been proposed in the literature including the Multiline Ring Anchor (MRA) concept. MRA is a novel shared anchor concept comprising of an embedded tubular anchor connected to multiple mooring lines, which permits a reduction in the total number of anchors. The MRA concept is shown in Figure1.3. The MRA has the applicability to be installed in wide range of soil type (Lee and Aubeny, 2020). MRA capacity in sand can theoretically be increased

by increasing its diameter or installing it deeper.

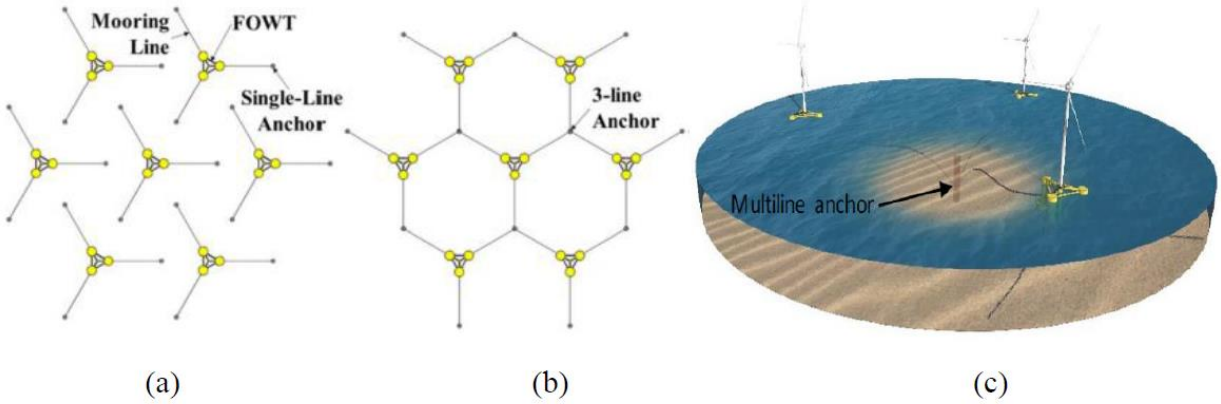

Figure 1.3: Layout of (a) single-line; (b) 3-line anchor; (c) multiline anchor concept. Reprinted from [Fontana et al., 2018]

1.2 Research Objectives

This research aims to fill the gap in the literature on caisson anchor capacity in medium and dense sand especially for caisson anchors with aspect ratios greater than one. The main objective of this research is to evaluate caisson foundation in sand as an anchoring solution for offshore floating wind turbine. By means of numerical and plastic limit analyses, the caisson foundation behavior is investigated, and a research matrix is built to examine the effect of key parameters on the monotonic ultimate capacity of the caisson foundation. Moreover, the Multiline Ring Anchor (MRA) behavior in sand is examined where the anchor is evaluated as an anchoring solution for offshore floating wind turbines. Finally, a bucket foundation is considered as a foundation type for a fixed 15-Megawatt wind turbine.

1.3 Dissertation Structure

This dissertation consists of 6 chapters which can be summarized as follows:

Chapter 2: a literature review of earlier work on ultimate capacity of caisson anchors and MRA in sand. The work falls in different categories such as experimental studies, centrifuge studies, numerical studies, and field test studies.

Chapter 3: this chapter focuses on caisson anchor behavior in sand and aims to evaluate the foundation as an anchoring solution for offshore floating wind turbines. The lateral and inclined ultimate capacities of the caisson anchor are estimated by means of numerical and plastic limit analyses.

Chapter 4: this chapter focuses on MRA behavior in sand where details about the finite element model developed to model the MRA is discussed and differences between the anchor structure and the caisson anchor are outlined. In addition to the numerical model, a simplified plastic limit analysis (PLA) model is proposed to estimate the lateral load capacity of MRA in sand.

Chapter 5: the main objective of this chapter is to size a bucket foundation for a fixed-bottom wind turbine structure that supports the International Energy Agency (IEA) 15-megawatt offshore wind turbine. Two different soils were considered medium dense and dense sand where the allowable bucket capacity was of interest.

Chapter 6: this chapter contains the main conclusions for the research and recommendations for future work.

CHAPTER II

LITERATURE REVIEW

2.1 Introduction

Many researchers studied the ultimate capacity of caisson anchors in sand, however, most of the practical experience in the literature comes from the oil and gas industry and these studies have largely focused on caisson capacity in cohesive soils. Although suction caisson is a common foundation solution that has been used in the oil and gas industry, its application in offshore floating wind turbine differs significantly in terms of the anchor aspect ratio, load magnitude, and soil type. Additionally, caisson anchors with an aspect ratio of less than one has been the focus for most of the studies in examining the ultimate capacity of caisson anchors in sand. A comprehensive overview of studies related to ultimate capacities of caisson anchor, MRA, and bucket foundation will be presented.

2.2 Centrifuge Test Studies

Bang et al (2011)

Bang et al carried out a series of centrifuge test to examine the ultimate capacity of suction piles in sand. Two main parameters were examined closely in Bang tests which are load inclination angle and padeye position. Bang et al considered five load attachment depths along the pile length ranging from 5%L to 95%L, model suction pile for centrifuge test shown in Figure 2.1.

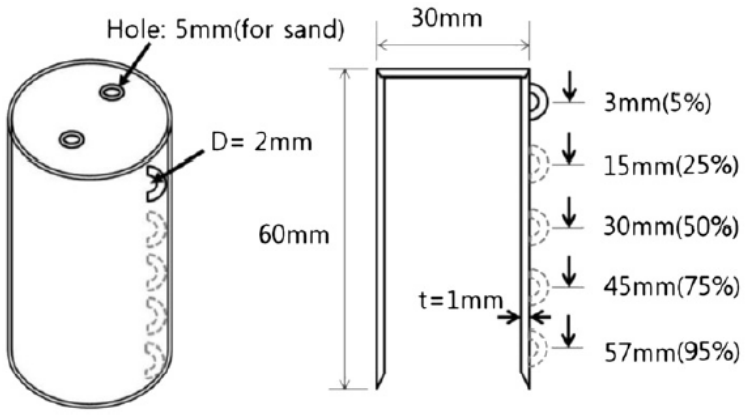

Figure 2.1: Model suction pile for centrifuge test. Reprinted from [Bang et al, 2011]

The centrifuge test facility at the Daewoo Institute of Construction Technology (DICT) permits an acceleration of 100g at the maximum payload, Pull-out loading system shown in Figure 2.2. The container and pull-out loading system are shown in Figure 2.2.

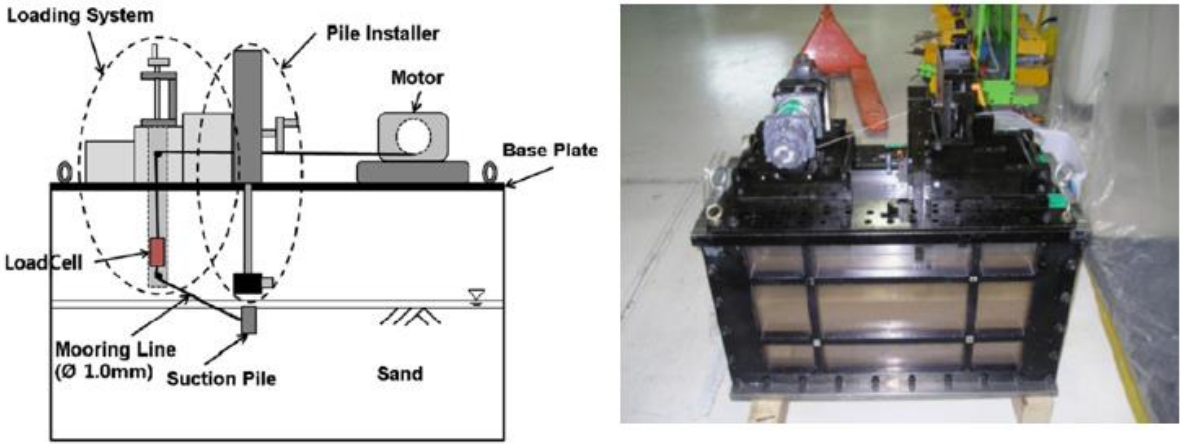

Figure 2.2: Pull-out loading system (left); container and pull-out loading system (right). Reprinted from [Bang et al, 2011]

Bang concluded that the ultimate capacity of the suction pile increased as the load attachment depth increased until it reaches a point located at 70-75%L where the suction pile at its maximum capacity. The effect of the padeye location is pronounced for small inclination angles (0 and 22.5).

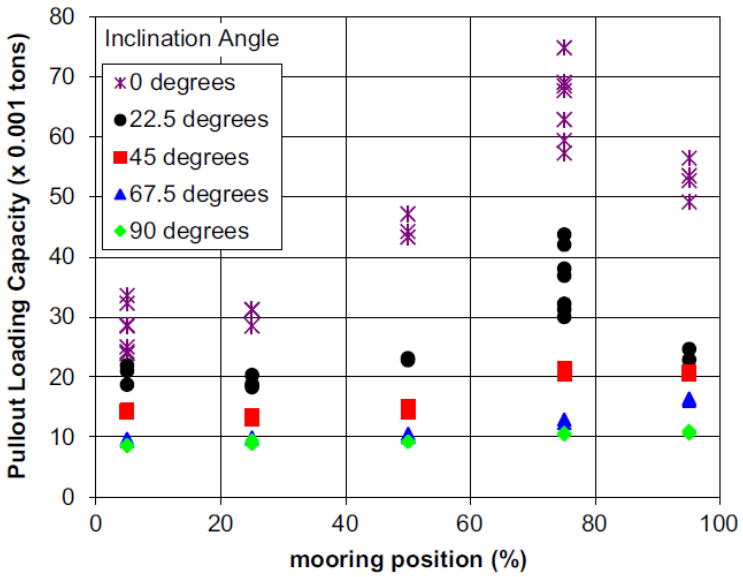

Figure 2.3: Centrifuge model test results. Reprinted from [Bang et al, 2011]

Jang and Kim 2012

Jang and Kim (2012) performed a series of centrifuge test to examine the ultimate lateral pullout capacity of suction pile in sand. In their tests Jang and Kim focused on one load attachment depth which is 75%L measured from the top, as shown in Figure 2.4. Jang and Kim (2012) chose the 75%L following the findings of Kim and Jang (2011) but varied the pile length and diameter to understand the effect of aspect ratio on the ultimate lateral pullout capacity of suction pile, Figure 2.4.

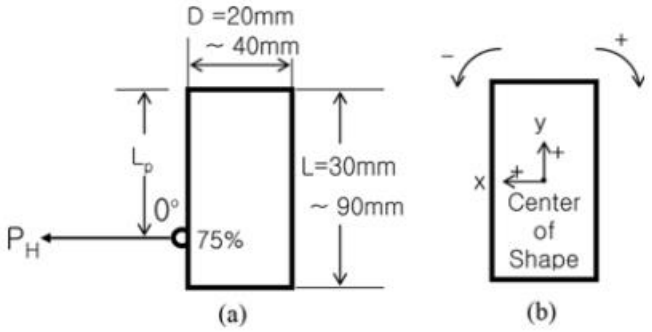

Figure 2.4: Experiment Parameters and Sign Convention: (a) Padeye Position, (b) Sign Convention. Reprinted from [Jang and Kim, 2012]

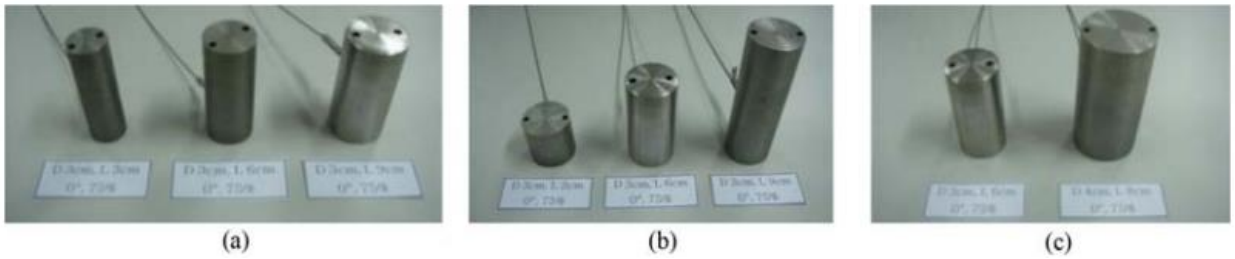

Figure 2.5: Schematics of Model Suction Piles: (a) Different Diameters, (b) Different Pile Length, (c) Suction Pile (L/D = 2). Reprinted from [Jang and Kim, 2012]

A summary of Jang and Kim (2012) results are shown in Table 2.1. The researchers concluded that the ultimate lateral capacity of the suction pile is a linear relationship with the pile diameter, and it is proportional to the square of the pile length.

Table 2.1: Test Results of Horizontal Capacity and Displacements.

Test No.	Inclination	Padeye Position (L0/L)	Pullout Capacity (MN)	Displacements (m)
A100-L60-D20-75	0	0.75	5.152	1.461
A100-L60-D25-75	0	0.75	5.899	1.109
A100-L30-D30-75	0	0.75	1.72	0.79
A100-L90-D30-75	0	0.75	17.205	0.975
A075-L80-D40-75	0	0.75	6.594	0.715

2.3 Experimental Test Studies

Villalobos et al (2009)

Villalobos et al (2009) carried out a series of lab testing using a loading ring with three degrees of freedom (Vertical, horizontal, and rotational), as shown in Figure 2.6. The tests were conducted on dry loose sand to emphasize on the drained response of the suction caisson.

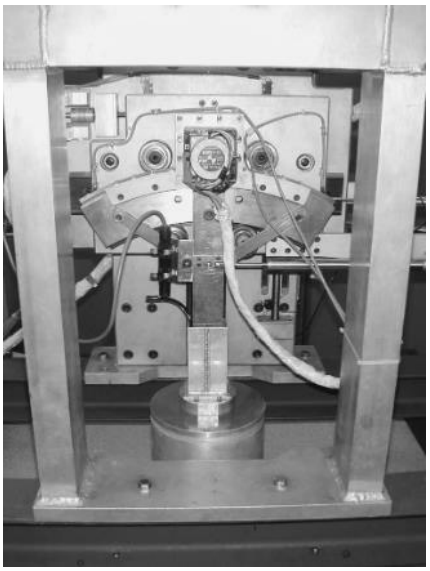

Figure 2.6: Three-degree-of-freedom loading rig at Oxford University. Reprinted from [Villalobos et al, 2009]

The vertical load was kept constant and low compared to the bearing capacity of the foundation and the caisson was subjected to rotational and translational loads. From the test results, Villalobos et al (2009) concluded that the caisson can mobilize a moment and/or horizontal resistance under tensile loads. Villalobos pointed out that importance of this finding especially for offshore wind turbines where the weight of the superstructure is low.

Gao et al (2013)

Gao et al (2013) performed a series of experimental studies to assess the behavior of suction caisson in sand. Gao focused on the effect of aspect ratio and load attachment depth on the ultimate capacity of suction caisson in sand. Three aspect ratios were considered 2,4, and 6 while the padeye locations considered in the tests are shown in Figure 2.7.

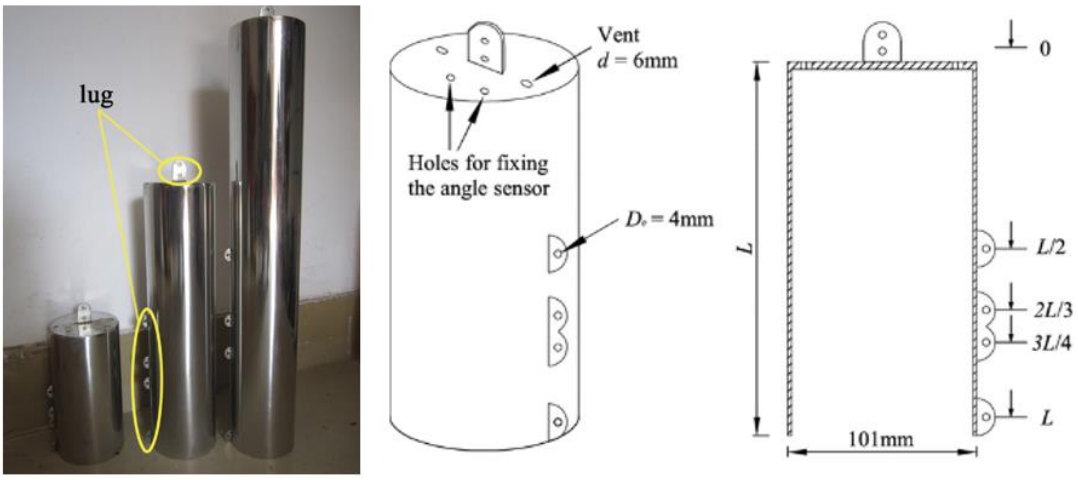

Figure 2.7: model suction caisson and padeye positions. Reprinted from [Gao et al, 2013]

Gao et al (2013) findings agree with Bang et al (2011), however, Gao found that influence of load inclination angle is not significant when load application point is at the top of the anchor. Additionally, Gao et al (2013) concluded that the optimum loading position is located between 2L/3 and 3L/4 where he explained that by the caisson movement mode. At 2L/3 the cession rotated

forward while it rotated backwards when the load attachment point was at 3L/4, as shown in Figure 2.8.

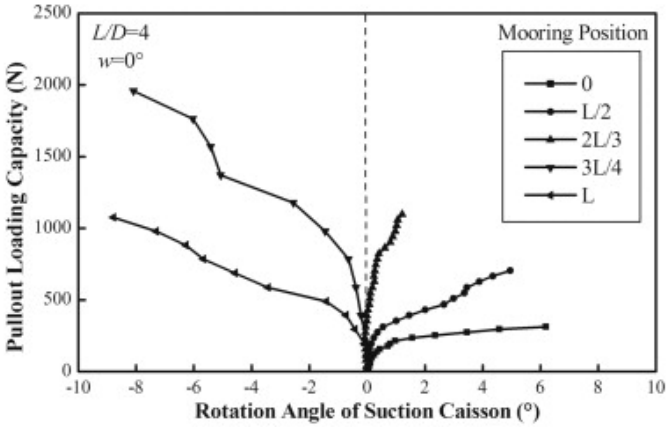

Figure 2.8: load–rotation angle curves of suction caissons under the conditions of L/D = 4 with different mooring positions. Reprinted from [Gao et al, 2013]

2.4 Finite Element Studies

Zhao et al (2018)

Zhao et al (2018) presented a numerical modeling study to evaluate the drained capacity of suction caisson in sand under inclined loading. The study assumes critical-state conditions which means the effect of dense sand dilation is not considered; Although, this approach is likely to underestimate the capacity as Randolph et al (2004) concluded; the study considered it appropriate for the parametric study. The study focused on suction caisson with aspect ratio less than one and considered three different aspect ratios 0.5, 0.8, and 1.

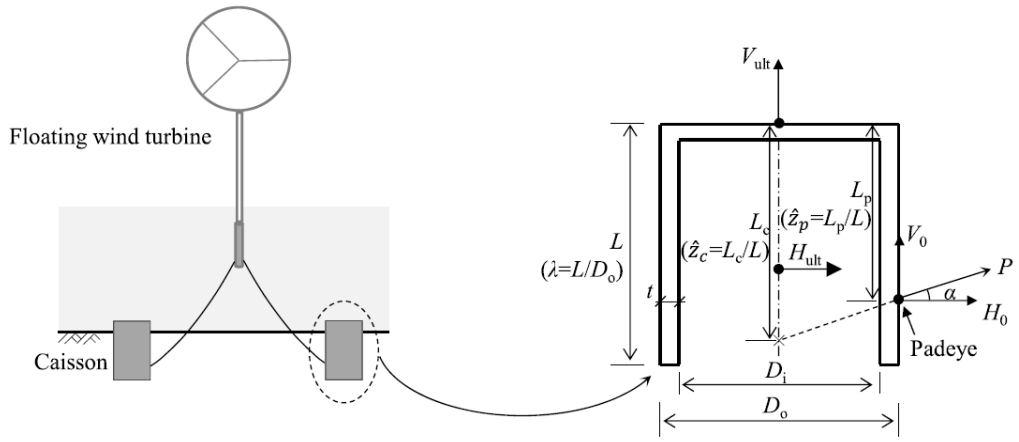

Figure 2.9: Floating wind turbine and notation for the caisson under inclined loading. Reprinted from [Zhao et al, 2018]

Mohr-Coulomb model was used in the numerical analysis to model the soil while the dilation angle was set to 2° as mentioned earlier the study considers a critical state condition and this value was used for numerical requirements to avoid any instability in the model by using 0°. Numerical results for the aspect ratios considered in the study are shown in Figure 2.10. From Figure 2.10, the maximum ultimate lateral capacity of the anchor (Inclination angle = 0°) corresponds to a padeye position that is located between 0.6 and 0.7 of the anchor length.

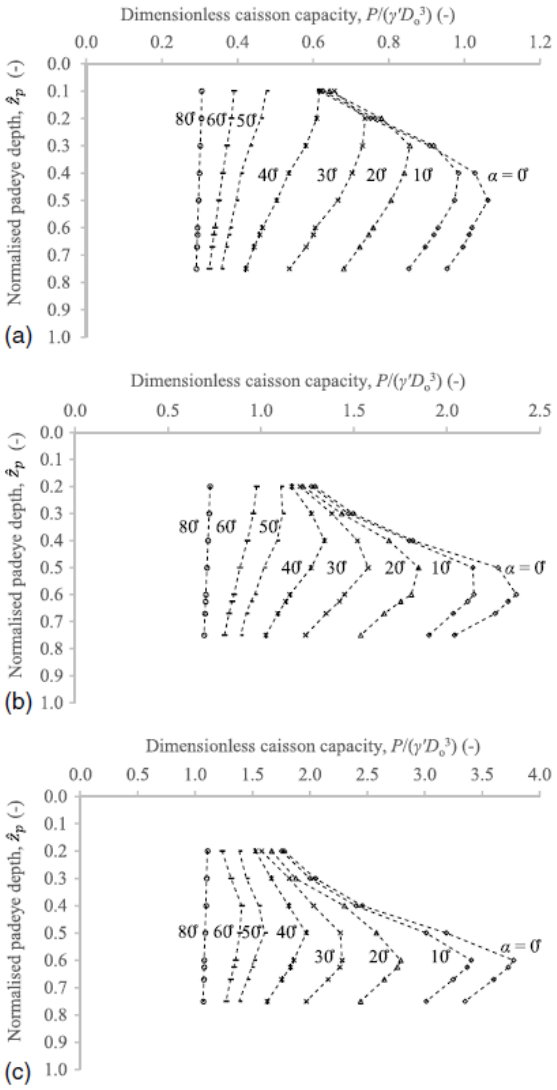

Figure 2.10. Caisson capacity at different load inclinations, padeye depths, and caisson aspect ratios: (a) L/D= 0.5; (b) L/D= 0.8; and (c) L/D= 1.0. Reprinted from [Zhao et al, 2018]

Zhao et al (2018) presented H-V yield envelopes in their study for caissons with aspect ratios <1 in sand, as shown in Figure 2.11. The interaction diagrams indicate that caisson anchors start losing capacity even at low inclination angles, as shown in Figure 2.11.

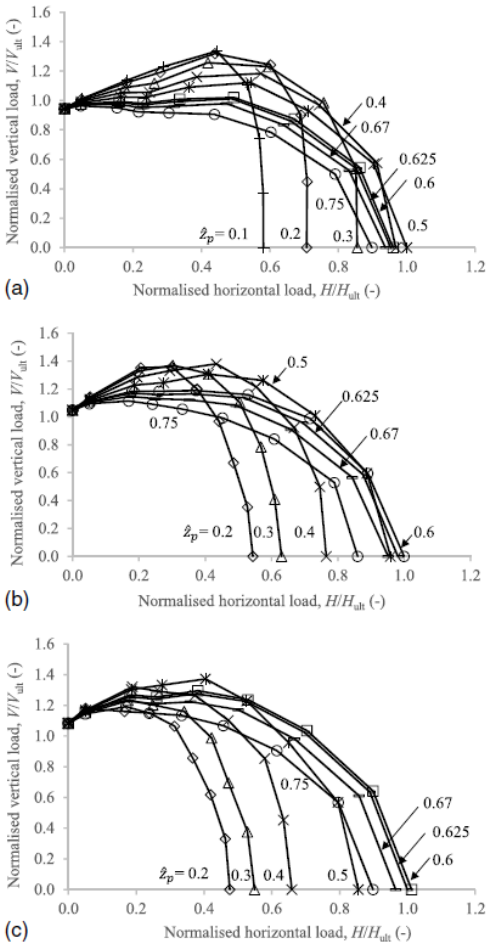

Figure 2.11: H-V yield envelopes for different pad-eye depths and caisson aspect ratios. Reprinted from [Zhao et al, 2018]

Aubeny et al (2003)

Aubeny et al (2003) proposed a simplified method to estimate the ultimate lateral capacity of suction caisson on clay. The study validated the model by comparing it to finite element solutions. Figure 2.12 shows the simplified model of suction Caisson and the failure mechanism assumed by Murff and Hamilton (1993). The proposed model employs the concept of generalized yield conditions where displacement and resistance are generalized stresses and strains,

respectively. As shown in Figure 2.12, the proposed model integrates unite lateral resistance at the side of the caisson and utilizes a spherical failure surface at the caisson tip.

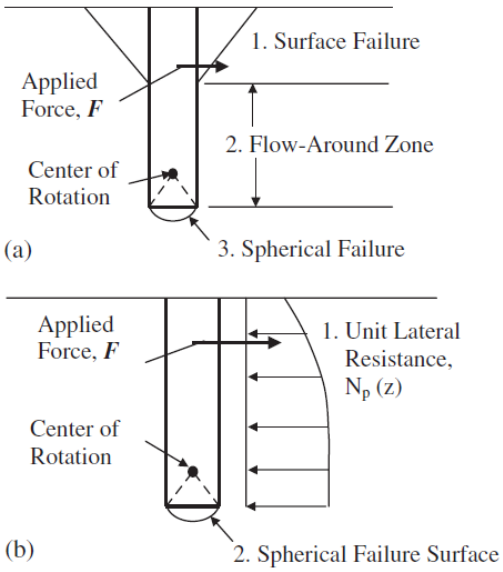

Figure 2.12: (a) failure mechanism assumed by Murff and Hamilton (1993); and (b) simplified analysis by Aubeny et al. (2001). Reprinted from [Aubeny et al, 2003]

Aubeny et al (2003) considered different aspect ratios between 2 and 10. The interaction diagrams presented in the study shows that the inclination angle is not significant for low inclination angles, as shown in Figure 2.13.

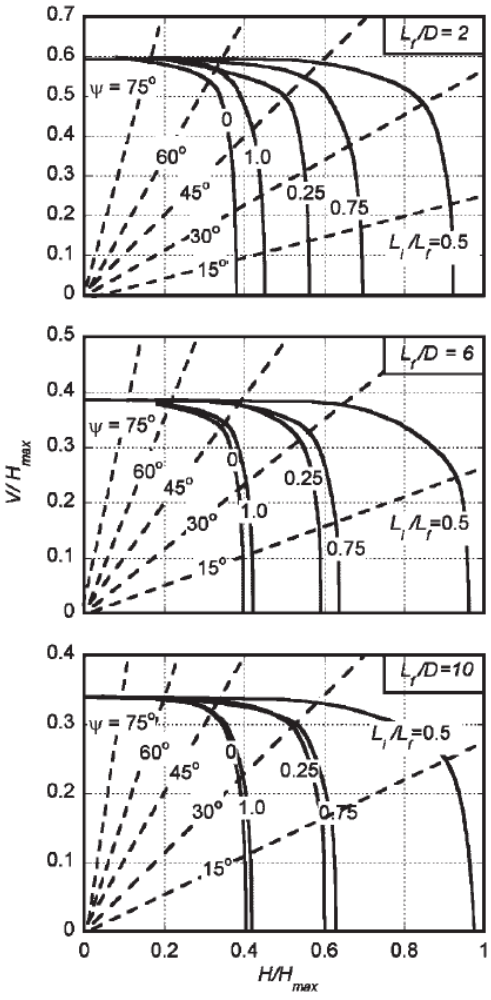

Figure 2.13: Vertical–horizontal load capacity interaction diagrams for uniform soil strength profiles. Reprinted from [Aubeny et al, 2003]

Achmus et al (2013)

Achmus et al (2013) conducted numerical studies to investigate the load-bearing behavior of suction bucket in dense sand. Achmus et al (2013) focused on the ultimate capacity of bucket foundation in sand but not the serviceability limit state. The study examined the effect of two main parameters which are the load eccentricity and the vertical load effect on the ultimate capacity. Figure 2.14 shows the ultimate capacity of the bucket at different load eccentricities.

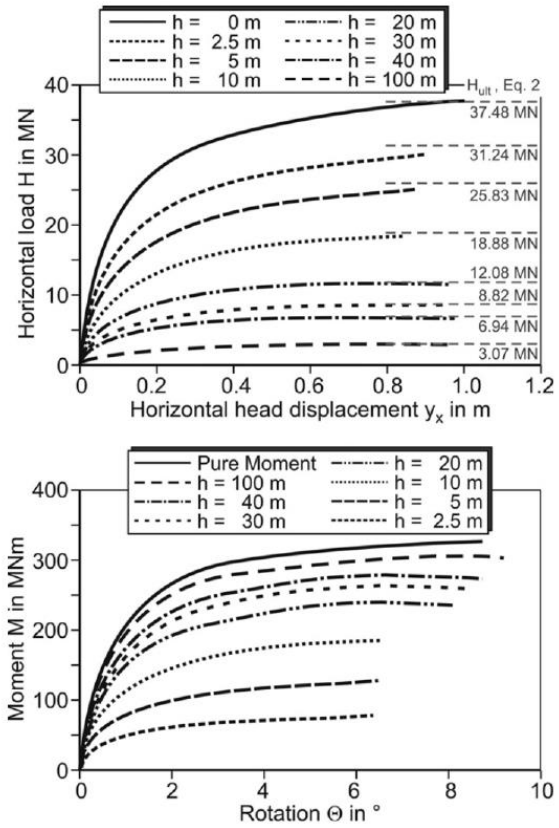

Figure 2.14: Horizontal load-head displacement and moment-rotation relations. Reprinted from [Achmus et al, 2013]

The effect of the superstructure weight or the vertical load on the ultimate capacity of the bucket foundation is shown in Figure 2.15. From Achmus et al (2013) study it can be noticed that the effect of the vertical loading can be significant.

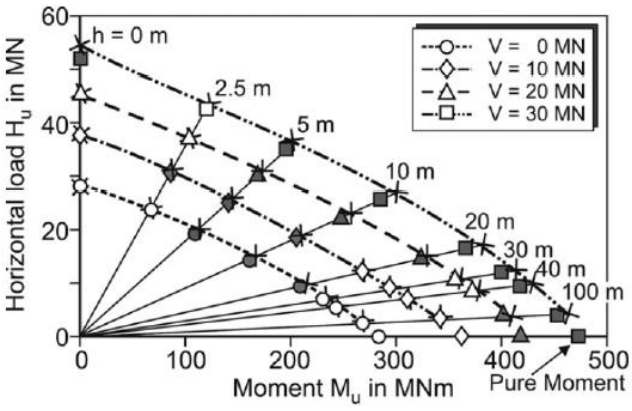

Figure 2.15: effect of vertical loading on the ultimate capacity of bucket foundation. Reprinted from [Achmus et al, 2013]

Deb and Singh (2018)

Deb and Singh (2018) conducted a series of numerical analysis studies to evaluate the capacity of monopod foundation under eccentric lateral loads in sand. Deb and Singh (2018) proposed two equations to estimate the ultimate and allowable load capacities of bucket foundations in sand which were developed by curve fitting to their numerical analysis studies.

The ultimate load capacity can be estimated using the following equation:

$$H_{ultimate} = \frac{\gamma' L D^2}{a+b\left(\frac{h}{L}\right)+c\left(\frac{h}{L}\right)^2} \quad (2.1)$$

The allowable load capacity which is defined at a bucket rotation of θ=0.5°

$$H_{Allowable} = a'(\gamma' L D^2) + b'(H_{ultimate}) + c' \frac{(H_{ultimate})^2}{\gamma' L D^2} \quad (2.2)$$

2.5 Plastic Limit Analysis

The upper bound plasticity limit analysis started with the early work of Drucker and Prager (1952) and later on with the work done by Chen (1975). To find an upper bound solution to the true limit load, the upper bound plasticity theory requires that the failure mechanism considered to be admissible. The theory states that for such a failure mechanism equating the internal rate of energy dissipation to the rate of work done by external forces yields an upper bound solution (Chen, 1975). For the development of the simplified method to estimate the ultimate lateral capacity of caisson anchors, estimating the ultimate lateral resistance per unit length that soils can exert is crucial and thus few methods from the literature were considered namely the equations developed by Broms (1964), Petrosovitz and Award (1972), Reese et al. (1974), and Prasad and Chari (1999). Each of the methods assumes a lateral earth pressure distribution, as shown in Figure2.18. Broms (1964) that the point of rotation is located at the pile tip while Petrosovitz and Award (1972) and Prasad and Chari (1999) assumption is that the pile will rotate at a point within the pile length.

Reese, Cox and Koop (1974) developed their model based on field tests considering two laterally loaded pile with a diameter of 24 inches and a wall thickness of 3/8 inch, pile instrumentation is shown in Figure 2.16. Using the field test results, Reese, Cox and Koop (1974) proposed a procedure for estimating the ultimate soil resistance. Two equations are proposed where the smaller value should be taken. The first equation assumes a wedge failure mode while the second equation assumes block failure mode.

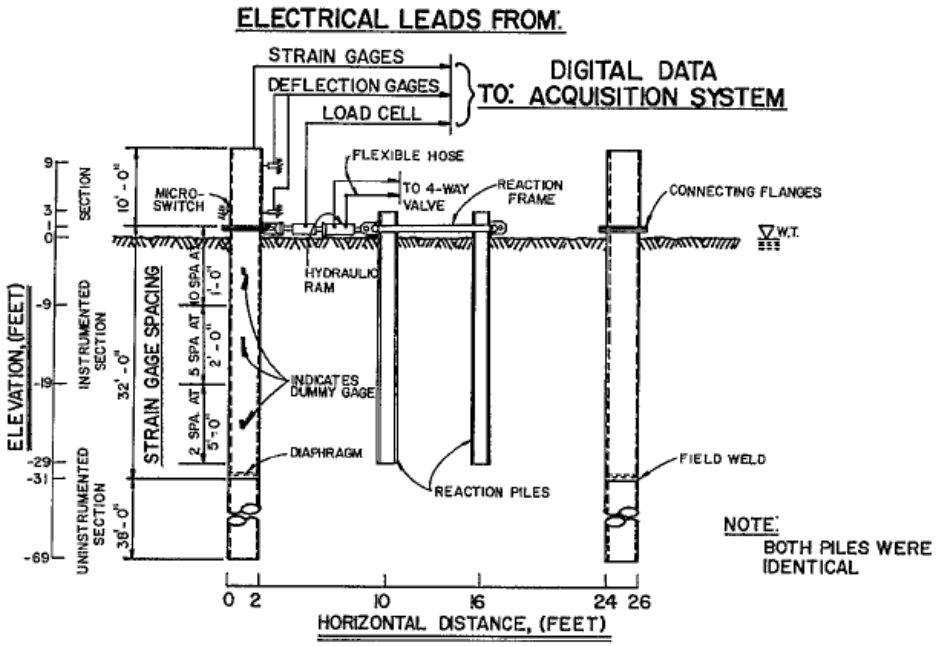

Figure 2.16: Pile instrumentation. Reprinted from [Reese, Cox and Koop ,1974]

The method takes the smaller quantity of p_u based on the following two equations:

$$\text{Pst} = \gamma' z \left[\frac{k_0 \tan\varphi' \sin\beta}{\tan(\varphi'-\beta)\cos\alpha} + \frac{\tan\beta}{\tan(\varphi'-\beta)}(b + z\tan\beta\tan\alpha) + k_0 z \tan\beta\,(\tan\varphi' \sin\beta - \tan\alpha) - k_a b \right] \quad (2.3)$$

$$\text{Psd} = k_a b\,\gamma' z\,(\tan\beta^8 - 1) + k_a b\,\gamma' z\,\tan\varphi'\tan\beta^4 \quad (2.4)$$

Reese, Cox, and Coop equations can be simplified and rewritten as shown in the next equation

$$\text{Pu} = (c_1 + c_2 \frac{z}{D})\,\gamma' z\, D < c_3\,\gamma' z\, D \quad (2.5)$$

Whiteside (1995) proposed simplified empirical fits for parameters c_1, c_2, and c_3 as follows

$$c1 = 0.124 \exp(0.091\varphi)$$

$$c2 = 0.58\exp(0.051\varphi)$$

$$c3 = 0.73\exp(0.123\varphi)$$

Since the main interest is the soil ultimate lateral resistance per unit length and earth pressure distribution associated with the different methods; Prasad and Chari (1999) the most recent out the chosen method will be considered to have an overview of these methods compare to each other and to measured soil pressure distribution. Prasad and Chari (1999) developed their equation based on experimental tests of steel model piles with diameter of 102 mm and length of 1135 mm.

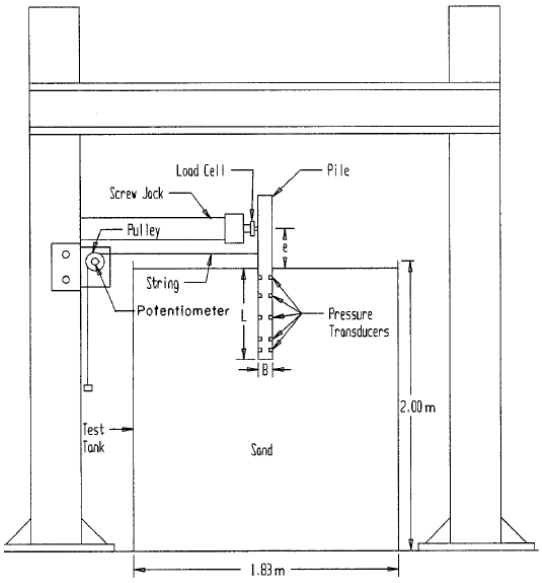

Figure 2.17: experimental set-up. Reprinted from [Prasad and Chari ,1999]

Prasad and Chari (1999) made use of measured data from Chari and Meyerhof (1983) to compare the different methods. Figure 2.18 shows prediction of soil pressure distribution.

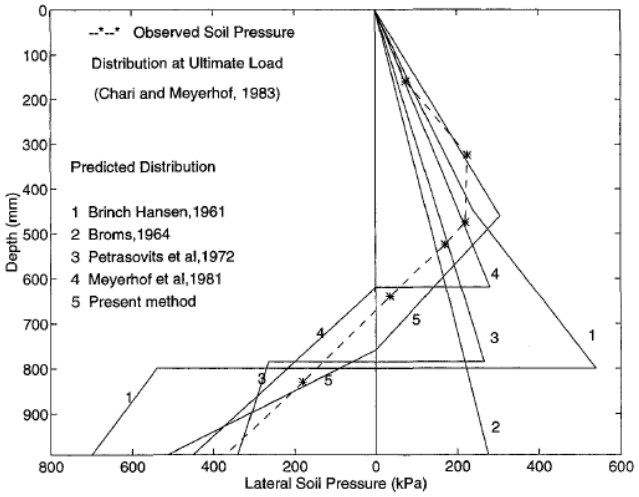

Figure 2.18: measured and estimated soil pressure distribution. Reprinted from [Prasad and Chari ,1999]

2.6 Multiline Ring Anchor

Multiline Ring Anchor (MRA) is a novel shared anchor concept comprises of a ring connected to multiple mooring lines which results in reduction in the total number of anchors. Since MRA is a new concept, there are currently no studies regarding the anchor capacity in sand, although a centrifuge test program investigating this topic is soon to be initiated.

Fontana et al (2018)

Fontana et al (2018) conducted a force dynamics study on multiline anchor to demonstrate the concept. Two multiline systems were considered 3-line and 6-line anchor system, Figure 2.19 shows the two systems.

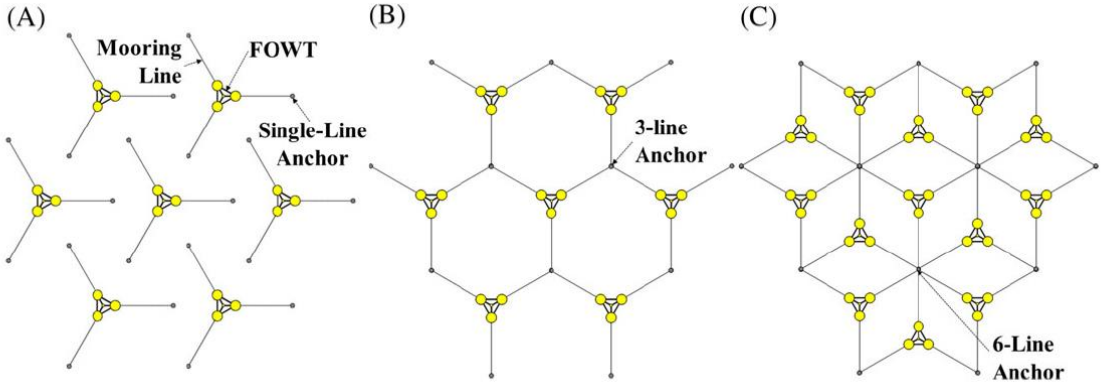

Figure 2.19: Layout of A, single-line; B, 3-line anchor; and C, 6-line anchor systems. Reprinted from [Fontana et al, 2018]

Total number of anchors for the single-line, 3-line, and 6-line geometries relative to farm size, and percent reduction in total number of anchors from single-line concept is shown in Figure x. Fontana et al (2018) found that multiline system anchor for floating offshore wind farm can results in about 60% and 79% reduction of the total number of anchors for the 3-line system and 6line system, respectively.

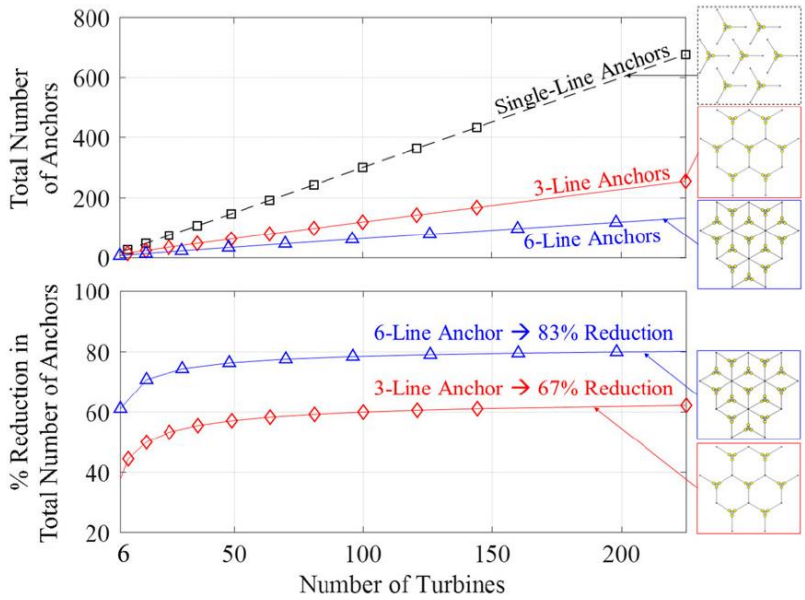

Figure 2.20: 3-line and 6-line systems compared to single line. Reprinted from [Fontana et al, 2018]

CHAPTER III

ULTIMATE CAPACITY OF CAISSON ANCHORS IN SAND UNDER GENERAL INL CINED MONOTONIC LOADING CONDITIONS

3.1. Introduction

This chapter focuses on caisson anchor behavior in sand and aims to evaluate the foundation as an anchoring solution for offshore floating wind turbines. The lateral and inclined ultimate capacities of the caisson anchor were estimated by means of numerical and plastic limit analyses. The caisson anchor behavior was investigated, and a research matrix is built to examine the effect of key parameters on the monotonic ultimate capacity of the caisson foundation.

For the lateral ultimate capacity of the caisson anchor, the effect of load attachment depth (padeye position) on the ultimate capacity was studied where different attachment depths were considered. The padeye location was optimized to find the optimum load attachment depth that corresponds to the maximum capacity which occurs when the rigid caisson anchor is under translational motion (no rotation). Other parameters including the soil strength parameters and load inclination angle were considered in the study and their effect on the ultimate lateral capacity was examined.

3.2 Numerical Model

A three-dimensional finite element model was developed in ABAQUS to estimate the capacity of short piles and caisson anchors in sand under general inclined monotonic loading conditions. In this section, details regarding the development of the finite element model and its validation are discussed.

3.2.1 Model Geometry and boundary conditions

In this section details related to the mesh, geometry, and boundary conditions of the finite element model developed to model the behavior of caisson anchor embedded in medium to dense sand soil is discussed. Figure 3.1 shows a sample of the mesh for the model. The mesh is generated by a MATLAB code to be able to modify and adopt different cases of loading conditions or material properties. The code is divided into four parts: mesh generator, material model, interaction model, and loading model. The mesh generator has added capabilities of refining certain regions of the model and controlling the element size and numbers for every part. Region refinement helps in building a refined mesh for a particular part in the domain that is of interest and a courser mesh for rest of the domain. The soil elements around the caisson both inside and outside are part of a refined mesh. Sensitivity analyses were completed to determine the refinement level and domain size, they are discussed later in this section.

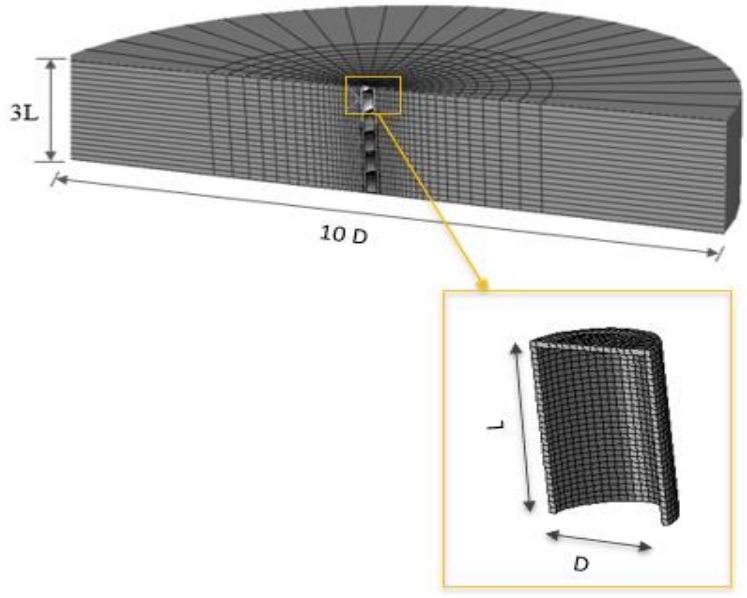

Figure 3.1: Finite- element mesh and domain dimensions.

Selecting the proper element type is important for obtaining correct and reliable solutions. The Solid continuum element C3D8 (8-node linear brick) was chosen to mesh the soil medium. C3D8 is a three dimension fully integrated element. Figure 3.2 shows the node and integration points numbering for C3D8 element.

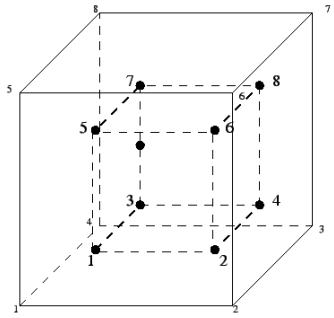

Figure 3.2: Nodes and integration points in C3D8 element.

Depending on the element analysis used elements are either Lagrangian or Eulerian. In Lagrangian formulation, both element and material deform together. However, in Eulerian formulation, nodes are constrained in space and material flows through elements that do not deform. Lagrangian formulation is more suitable for stress and displacements problems.

Boundary conditions

Two boundary conditions (BCs) are imposed on the model:

- Displacements are constrained on the far-field nodes for both of the horizontal directions (u_x, u_y).
- Displacements are constrained in all directions (u_x,u_y,u_z) for the bottom nodes of the model.

To simulate the far-field boundary conditions, the infinite element CIN3D8 is used for the far-field elements. Such elements are available in Abaqus element library to model problems in which the region of interest is small in size compared to the surrounding medium.

Sensitivity analyses

Sensitivity analyses were carried out to refine the mesh and extend the model domain size to mitigate the effect of boundary conditions and coarse mesh on the caisson anchor capacity. Different mesh refinements and domain configurations are attached later in Appendix A.

3.2.2 M-C in ABAQUS

The constitutive model Mohr-Coulomb is used to model the soil. Mohr-Coulomb is an elastic-perfectly plastic model used to represent shear failure in soils. The model has five parameters that are recognized and have a physical meaning. In the background chapter Mohr-Coulomb model was discussed and few features of the model were highlighted; however, this section will briefly go over Mohr-Coulomb model in ABAQUS and how it is being implemented.

In ABAQUS, Mohr-Coulomb constitutive model can be used to model granular materials under monotonic loading conditions. Linear isotropic elasticity is required to be used with Mohr-Coulomb; the model has a regime that represents the linear elastic response then after that some of the material deformations are considered plastic (irrecoverable). Mohr-Coulomb model has a smooth and non-associated plastic flow potential. The Mohr-Coulomb yield function is written as:

$$F = R_{mc}q - p\tan(\varphi) - c = 0 \qquad (3.1)$$

Where R_{mc} is a measure of the shape of the yield surface in the deviatoric plane

$$R_{mc} = \frac{1}{\sqrt{3}\cos\varphi}\sin\left(\theta + \frac{\pi}{3}\right) + \frac{1}{3}\cos\left(\theta + \frac{\pi}{3}\right)\tan\varphi \qquad (3.2)$$

Where φ is the friction angle of sand and it is the slope of the yield surface for M-C model

c is cohesion.

Θ is the deviatoric polar angle. Under shear, extension, and compression

Θ is $0°, -30°, 30°$ respectivly.

p is the equivalent pressure stress and q is the Mises equivalent stress

Using the stress tensor invariants to define the yield function is more suitable for geotechnical analyses. Abaqus invariants:

Pressure stress, $p = \frac{-1}{3}\text{trace}(\boldsymbol{\sigma})$

Mises equivalent stress, $q = \sqrt{\frac{3}{2}(\mathbf{S}:\mathbf{S})}$

Third invariant, r $= \left(\frac{9}{2}\,\mathbf{S}\,.\,\mathbf{S}:\mathbf{S}\right)^{\frac{1}{3}}$

Stress decomposition: $\boldsymbol{\sigma} = \mathbf{S} - \text{p}\,\mathbf{I}$

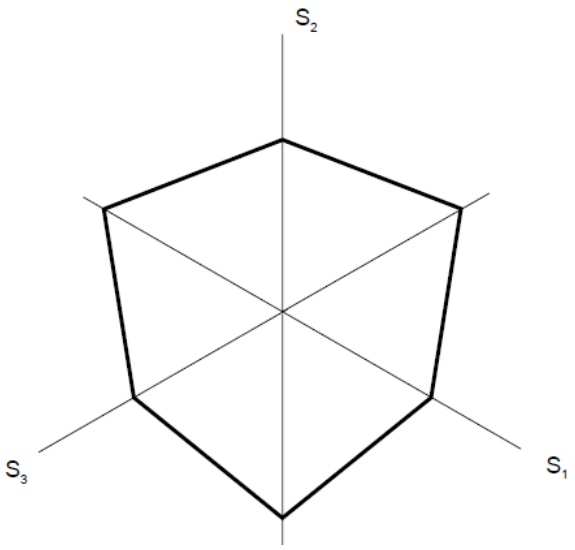

Figure 3.3: Mohr-Coulomb yield surface.

Plastic potential function (G)

In ABAQUS, for Mohr-Coulomb model the flow potential is chosen as a hyperbolic function in the meridional stress plane and the smooth elliptic function proposed by Menétrey and Willam (1995) in the deviatoric stress plane:

$$G = \sqrt{(\varepsilon c \tan\psi)^2 + (R_{mw} q)^2} - p \tan\psi \qquad (3.3)$$

Where c is initial cohesion

ψ is the soil dilation angle.

ε controls the shape of the flow potential function in the meridional plane

R_{mw} controls the shape of the flow potential function in the deviatoric plane

For the flow potential function (G) the internal friction angle (φ) is replaced by the soil dilation angle (ψ). In ABAQUS the flow rule is non-associated thus G≠F where $\psi < \varphi'$. Plastic

flow in the deviatoric plane is always non-associated; therefore, the unsymmetric solver should be used.

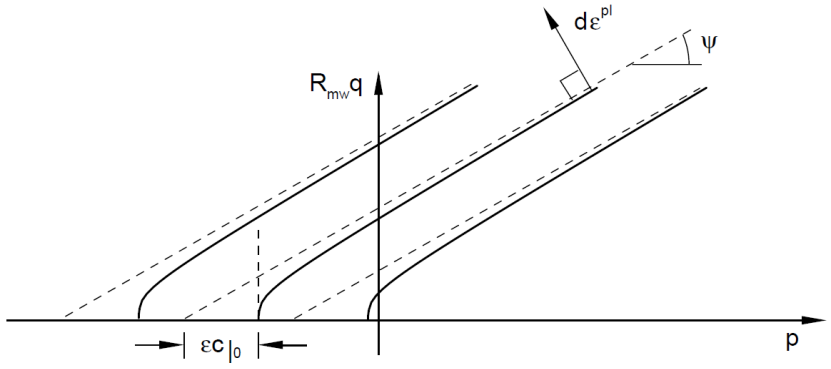

Figure 3.4: M-C flow potential in meridional plane.

Flow rule

A flow rule is needed in the constitutive model to determine the magnitude and the direction of plastic deformation.

$$\dot{\varepsilon}^{p} = \lambda \frac{\partial G}{\partial \boldsymbol{\sigma}} \qquad (3.4)$$

Where $\dot{\varepsilon}^{p}$ plastic strain rate

λ plastic multiplier

Since dense sand is of interest, the conventional Mohr-Coulomb idealization does not adequately capture the behavior of dense sand and the constant dilation assumption is one of the model limitations. Mohr-Coulomb model is used in this research but in an effort to better understand the effect of dilatancy, a USDFLD subroutine was written in Fortran and used in

conjunction with Mohr-Coulomb model that is available in ABAQUS library. The USDFLD subroutine is discussed later in Section 3.2.6.

3.2.3 Material properties and model parameters

As discussed earlier in this chapter, the soil was modeled as an isotropic elastic-perfectly plastic material using Mohr-Coulomb model available in ABAQUS library. The Mohr-Coulomb model is an elastic-perfectly plastic model that is used to represent shear failure in soils. In this section, the model parameters are discussed and the parameters selection to help correctly model the nonlinear soil response.

To model the sand in ABAQUS, the linear isotropic elasticity model was used with Mohr-Coulomb model to represent the elastic regime. For the elasticity model, two parameters are required modulus of elasticity (E) and Poisson's ratio (ν). For Mohr-Coulomb model, friction angle (φ), dilation angle (ψ), and cohesion (c) are the required parameters. The soil considered in this study is cohesionless but to ensure numerical convergence a low value of nominal cohesion is assigned.

Modulus of elasticity (E)

To correctly model the nonlinear soil response the stress dependency must be taken into account when estimating Young' modulus. There are several equations available in the literature to estimate the value of Young' modulus.

Equation suggested by Janbu (1964)

$$E_s = k\, pa \left(\frac{\sigma_m}{pa}\right)^n \qquad (3.5)$$

Stiffness ratio - Merifield and Sloan (2006)

$$E / \gamma D = 500 \quad (3.6)$$

Rigidity index by Vesic (1972)

$$I_r = \frac{E}{[2(1+\upsilon)(\sigma v * \tan\varphi)]} \quad (3.7)$$

In this study, the rigidity index approach by Vesic (1972) was employed. To estimate the the stress-dependent Young' modulus equation 3.8 is used

$$E = Ir * [2(1+\upsilon)(\sigma v * tan\varphi)] \quad (3.8)$$

where, E = Young' modulus
Ir = Rigidity index (from Figure 3.5)
υ = *Soil Poisson's ratio*
σ_v = *Vertical effective stress*
φ = *Angle of peak internal friction*

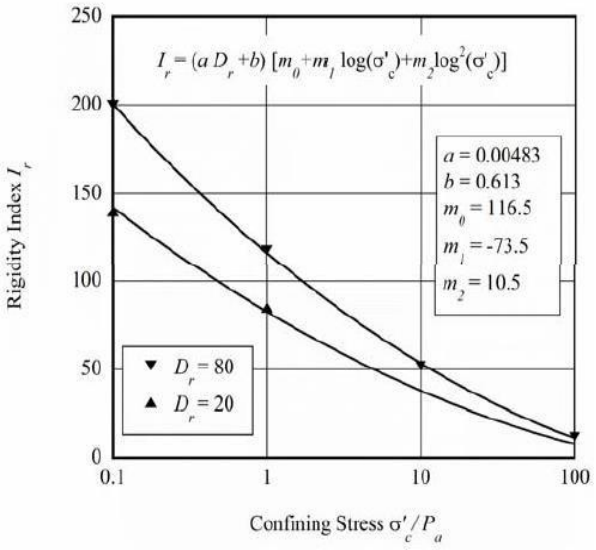

Figure 3.5: Rigidity index vs. confining stress. Reprinted from [Al Hakeem and Aubeny 2019]

Poisson's ratio (v)

In elastic material deformations, Poisson's ratio defines the ratio deformation perpendicular to the direction of a normal loading. to. Generally, for a homogeneous and isotropic

soil, the Poisson's ratio varies in the range $0 \leq \nu \leq 0.5$. For the medium to dense sand soil considered in this study a Poisson's ratio (ν) equals 0.3 is used.

Mohr-Coulomb model

The two input parameters for Mohr-Coulomb model are friction angle (φ) and dilation angle (ψ). It is common to treat these material parameters as constants where φ and ψ are assigned a single value, however, in reality both material parameters are a function of soil density and stress level.

Integrating the effect of soil density and stress level on φ and ψ requires the use of empirical relationships available in the literature. A soil profile was created where friction angle (φ) and dilation angle (ψ) are generated using Bolton equations. Bolton (1986) found that equation 3.9 can be used to estimate the peak friction angle for both plane-strain and triaxial compression conditions.

$$\varphi_{peak} = \varphi_{critical} + A\psi\, I_R \qquad (3.9)$$

Where $\varphi_{critical}$ is the critical state friction angle

$A\psi = 3$ for triaxial condition and 5 for plane strain condition.

I_R is a relative dilatancy index and equation (3.10) is used to estimate it.

$$I_R = D_r\,(10 - \ln p) - 1 \qquad (3.10)$$

After calculating the peak friction angle, the peak dilation angle can be estimated using the following equation:

$$\varphi_{peak} - \varphi_{critical} = 0.8\ \psi_{peak} \quad (3.11)$$

Soil-caisson interface friction angle (δ)

As mentioned earlier in the contact section, the caisson-soil interface was modeled using the Coulomb friction model. The friction factor (μ) is a model parameter that depends on the soil-caisson interface friction angle (δ)

$$\mu = \tan(\delta)$$

The soil-caisson interface friction angle (δ) depends on the caisson surface roughness, size and shape of soil particles and soil gradation. Han *et al.* (2018) carried out a series of direct interface shear tests to investigate the effect of these factors on the soil-caisson interface friction angle (δ). The tests consisted of 10 different soil samples and various rusting levels of steel surfaces. The test setup is shown in Figure 3.6 where the soil sample is sheared horizontally on top of the steel interface.

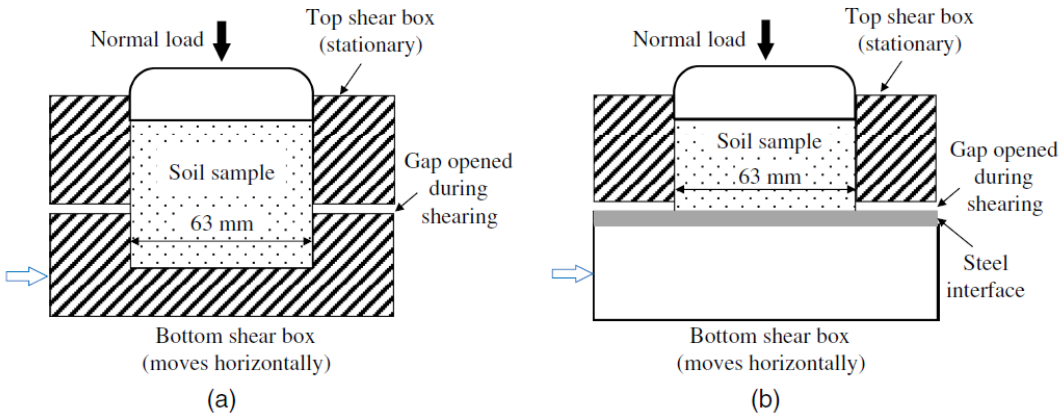

Figure 3.6: Test setup (a) direct shear test; and (b) direct interface shear test. Reprinted from [Han et al 2018]

Han concluded that angular soil particles increase the interface friction angle. Similarly, the surface roughness has the same effect on the interface friction angle. Higher rusting level on the steel surface result in a higher interface friction angle (rougher surface). The smooth steel surface has a δ/φ ratio of 0.5 while the heavily rusted steel surface has a ratio of 0.9.

To further assess the effect of surface roughness, the load inclination is considered. Huang *et al*. (2019) examined the effect of load inclination angle and surface roughness on the ultimate capacity of rigid piles in sand. Figure 3.7 shows that for load inclination angles greater than 45° the effect of surface roughness is pronounced. In this study, $\mu = \tan(0.6\,\varphi)$ was adopted to model the caisson-soil interface.

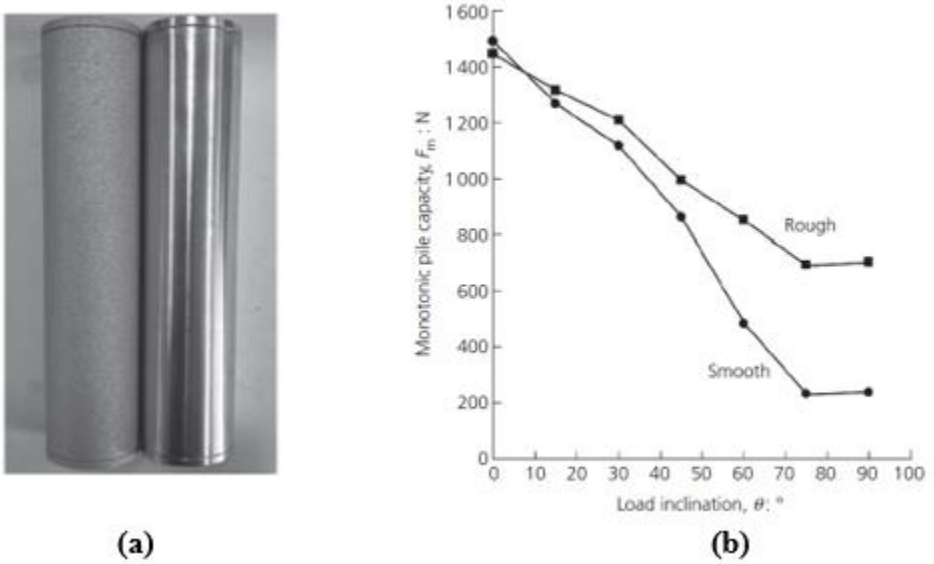

Figure 3.7: Surface roughness vs. inclination angle. Reprinted from [Huang *et al*.,2019]

3.2.4 Modeling contact interface

Modeling the contact and interaction between the caisson anchor and soil is challenging and needs to be modeled carefully to ensure that the solution obtained is correct and accurate. In general, contact mechanics theory is used to define normal and tangential stresses that occur during the analysis between the nodes or surfaces in contact.

ABAQUS has two contacts approaches that can be used to model contact problems. Although the two methods use similar algorithms, they differ in the user interface and the available options. The first contact type is General contact where the contact is imposed over several regions of the model or the entire domain. General contact is the simpler of the two methods since the entire domain is considered and the contact variables and surface characteristics are given independently. However, a contact pair, the other contact algorithm available in Abaqus can be more efficient compared to general contact. Obtaining a better analysis performance using contact pair requires a well-defined contact surfaces and properties.

Contact pair, as the name indicates requires two surfaces to be defined, a master surface and a slave surface, where the two surfaces interact with each other. All contact definitions in this study employed the contact pair approach.

Contact discretization

The contact discretization is the first step after selecting contact pair approach. There are two available options for contact discretization:

Node to surface: it is the traditional option in ABAQUS where a slave node interacts with a point of projection on a master surface. Slave nodes are restricted not to penetrate the master surface;

however, the master surface nodes can penetrate into the slave node-based surface. Figure 3.8 shows the node to surface option in ABAQUS.

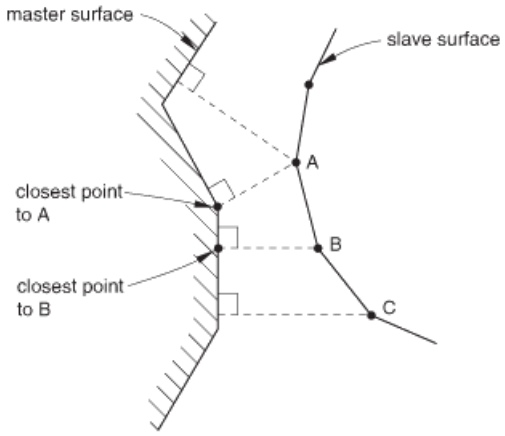

Figure 3.8: Node-to-surface contact discretization. Reprinted from [ABAQUS, 6.14]

Surface to surface: this option imposes contact conditions as an average over regions of adjacent slave nodes as opposed to a single slave node in node to surface option. Since it is an average, one slave node will eventually be considered but all neighboring slave nodes are included. Figure 3.9 illustrates the two discretization options.

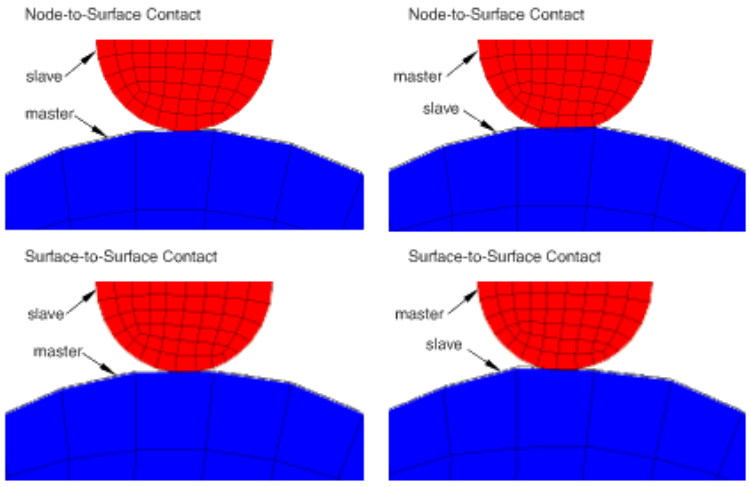

Figure 3.9: Comparison of contact enforcement for different master-slave assignments with node-to-surface and surface-to-surface contact discretization. Reprinted from [ABAQUS, 6.14]

Contact tracking approaches

During the analysis the pairing surfaces will interact with each other which will result in a relative motion that needs to be tracked. ABAQUS offers two methods to track the movement of the contact surfaces.

1- Finite sliding technique

This method is considered the general technique that Abaqus uses in tracking movements in contact problems. The finite sliding permits arbitrary separation, sliding, and rotation of the surfaces. The default settings for tracking motion in contact pair is finite sliding technique. However, invoking finite sliding forces Abaqus to constantly track which part of the master surface is in contact with each slave node. For the majority of contact problems this constantly tracking is unnecessary and costly in terms of computational efforts and requires very complex calculations.

Figure 3.10 shows a simple example of finite sliding in ABAUS. In this example slave node 101 may come into contact anywhere along the master surface BSURF. While in contact, it is constrained to slide along BSURF, irrespective of the orientation and deformation of this surface. This behavior is possible because Abaqus/Standard tracks the position of node 101 relative to the master surface BSURF as the bodies deform. (ABAQUS).

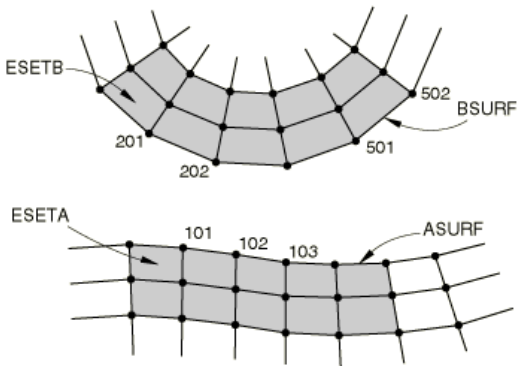

Figure 3.10: Contacting bodies finite sliding

2- Small sliding technique

This tracking approach differs from the finite sliding by defining a relationship between the slave nodes and master surface (node to master disc) and maintaining that relationship throughout the analysis. Abaqus in the small sliding formulation assumes that contact interaction occurs between a slave node and a tangent plane of the established segment of the master surface.

Figure 3.11 shows an example of small sliding in ABAQUS. The local tangent plane, which is a line in two dimensions, is defined by an anchor point, X_0, on the master surface and an orientation vector at the anchor point.

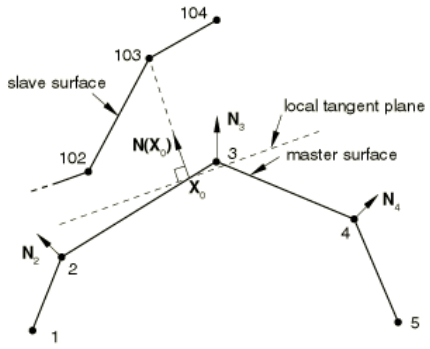

Figure 3.11: Definition of the anchor point, and local tangent plane used by the small-sliding. Reprinted from [ABAQUS, 6.14]

Surfaces definition

Different surfaces were defined for the soil-caisson interface. The caisson anchor surfaces, interior and exterior walls, were defined as master surfaces while the soil surfaces in contact were defined as node-based surfaces and modeled as the slave surface.

Friction model

The pairing surfaces in contact problems transfer loads through their interaction. These loads are normal and shear forces. The caisson-soil interface was modeled using the Coulomb friction model. The model uses a friction factor (μ) that relates the frictional shear stress to the normal pressure. The friction factor depends on the caisson surface roughness, but a common range is 0.5-0.7φ.

A critical shear stress value (Figure 3.12) is assumed for the model that depends on the normal contact pressure.

$$\tau_{critical} = \mu\, p$$

Where μ is a friction factor

p is the contact pressure between the two surfaces which represents the horizontal effective pressure σ_h.

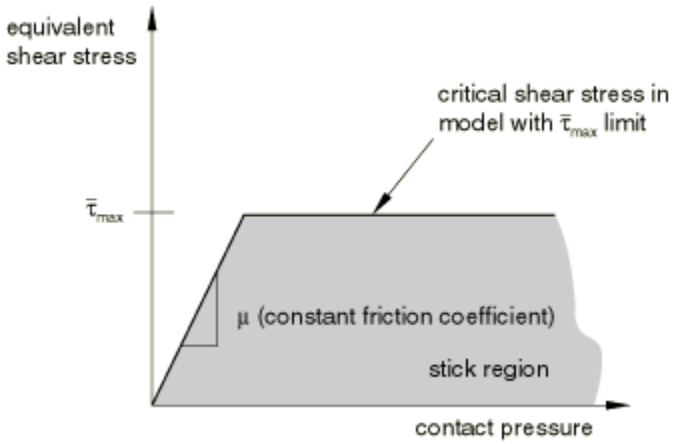

Figure 3.12: Frictional behavior.

3.2.5 Loading conditions

The main objective of this chapter is to evaluate caisson foundation in dense sand as an anchoring solution for offshore floating wind turbine. The three-dimensional finite element model was developed in ABAQUS to estimate the capacity of caisson anchors in sand under general inclined monotonic loading conditions. The loading conditions considered in this study are laterally loaded caisson anchor and caisson anchor under inclined tensile loads.

All loading conditions analyses were carried out under displacement control. The caisson anchor was modeled as a rigid body with displacements applied to a reference point which was taken as the pad-eye. Figure 3.13 shows the caisson anchor and the pad-eye location where the horizontal displacement is imposed.

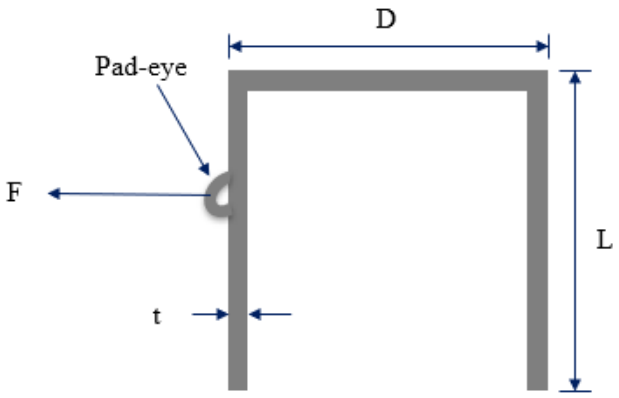

Figure 3.13: Caisson anchor under lateral loading condition.

To model the inclined load condition a local coordinate system was defined in ABAQUS where the keyword (*TRANSFORM) was used to introduce a transformed coordinate system. Figure 3.14 shows both local coordinate system (X`, Y`, Z`) and global coordinate system (X, Y,Z).

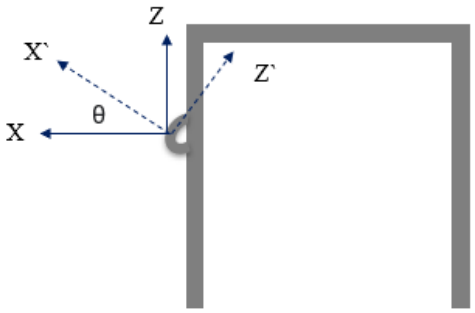

Figure 3.14: Local and global coordinate systems.

The local coordinate system is rotated by an angle (θ) which represents the load inclination angle.

Loading steps

The initial step is a geostatic step (*GEOSTATIC). This step is used to simulate the in-situ conditions where the initial geostatic stresses and gravity loads must be in equilibrium and generate no deformations.

Horizontal and vertical stress components must be defined in the initial conditions. To properly calculate stresses in the soil domain the following parameters are required:

- $\varphi_{critical:}$ critical state friction angle
- $K_{0:}$ The coefficient of lateral earth pressure at rest which is the ratio of effective horizontal stress to effective vertical stress. Equation 3.12 can be used to estimate the coefficient value.

$$K_0 = 1 - \sin \varphi_{critical} \quad (3.12)$$

The interaction model is then activated to establish contact between soil surfaces and the surfaces of the caisson anchor. The following loading step is to apply displacements at the pad-eye until the anchor fails. In this study a failure criterion of 10% of the anchor diameter was adopted.

3.2.6 USDFLD Subroutine

The constitutive model Mohr-Coulomb was used to model the soil. However, since dense sand is of interest, the conventional Mohr-Coulomb idealization does not adequately capture the behavior of dense sand and the constant dilation assumption is one of the model limitations. Shuttle and Jefferies (2005) discussed the use of other models and pointed out that these models are rarely more advanced than non-associated Mohr-Coulomb. They asked that any additional effort in the parameter determination for any advanced constitutive model must be justified. Thus, in an effort

to better understand the effect of dilatancy, a USDFLD subroutine was written in Fortran and used in conjunction with Mohr-Coulomb model that is available in ABAQUS library.

USDFLD

The user subroutine USDFLD is usually employed to model the behavior of a complex material without writing a complete UMAT subroutine. Most material properties (e.g., friction angle, φ) can be defined as functions of field variables. Since USDFLD has access to the solution data, the material properties can be a function of the solution data. Figure 3.15 shows a flow chart of ABAQUS standard and when USDFLD is being called.

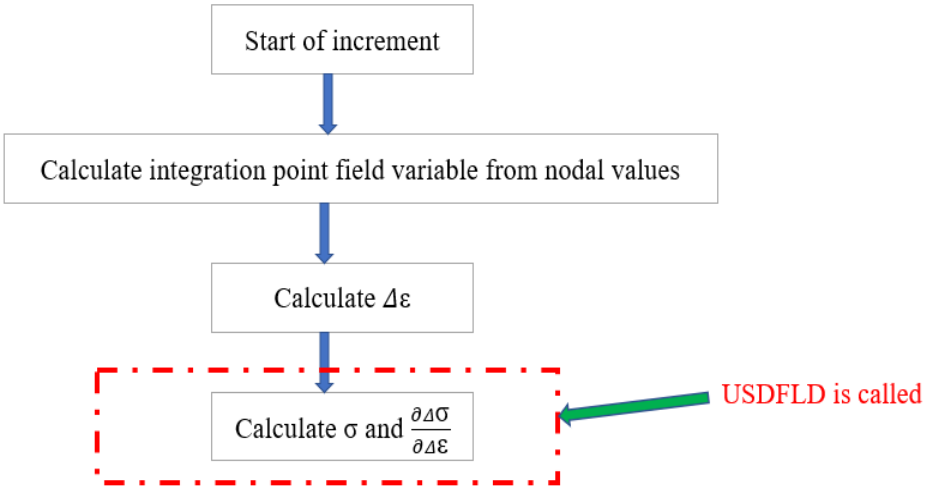

Figure 3.15: Detailed flow of ABAQUS Standard regarding USDFLD.

In this study, two field variables are created where the material properties soil internal friction angle (ϕ') and dilation angle (ψ) depend on. The two field variables are:

1- The first field variable (FV1) is the mean effective stress (p') and it is calculated using the stress components from the solution.

2- The second field variable (FV2) is the plastic shear strain increment γ^p and it is calculated using the strain increment components from the solution.

Accessing the solution data to calculate FV1 and FV2 requires the use of the utility routine GETVRM from which the stress and strain components are obtained. To compute the soil internal friction angle (ϕ') and dilation angle (ψ) based on the values of the field variables, Abaqus provides two approaches:

1- Tabular form if the material model is one of ABAQUS built-in models.

2- Other user subroutines.

Since Mohr-Coulomb is a built-in material model in ABAQUS, the tabular form is utilized. Figure 3.16 shows the use of DEPENDENCIES parameter to employ the tabular definition method. During the analysis, ABAQUS calls the subroutine and updates the values of ϕ' and ψ based on the field variables value.

```
*MOHR COULOMB, Dependencies=2
2.956741e+01,1,2.692229e+00,1.500000e-05
4.620000e+01,2.533333e+01,2.692229e+00,5.346899e-02
3.498254e+01,6.637559e+00,2.692229e+00,2.062345e-01
3.107163e+01,1,2.692229e+00,3.590000e-01
2.949463e+01,1,8.076688e+00,1.500000e-05
4.620000e+01,2.533333e+01,8.076688e+00,7.036914e-02
3.559971e+01,7.666184e+00,8.076688e+00,2.146846e-01
3.112747e+01,1,8.076688e+00,3.590000e-01
2.946405e+01,1,1.346115e+01,1.500000e-05
4.620000e+01,2.533333e+01,1.346115e+01,7.995478e-02
3.597323e+01,8.288710e+00,1.346115e+01,2.194774e-01
3.117419e+01,1,1.346115e+01,3.590000e-01
```

Figure 3.16: A snapshot of the input file.

Subroutine equations

Bolton equations are used to estimate the peak values for internal friction angle (ϕ') and dilation angle (ψ) following the process discussed in Section 3.2.3. However, with the help of USDFLD subroutine different values ranging from $\phi'_{critical}$ to ϕ'_{peak} can be assigned depending on the defined field variables. Similarly, the dilation angle (ψ) can have any value between 0 and ψ_{peak}. These relationships between the material properties ϕ' and ψ and the field variables mean effective stress (p') and the plastic shear strain increment γ^p are modeled using the following equations from Roy (2016).

<u>Pre-peak region:</u>

$$\phi' = \phi'_{in} + \sin^{-1}\left[\left(\frac{2\sqrt{\gamma^p \gamma^p_p}}{\gamma^p + \gamma^p_p}\right)\sin(\phi'_{peak} - \phi'_{in})\right] \qquad (3.13)$$

$$\psi = \sin^{-1}\left[\left(\frac{2\sqrt{\gamma^{p}\gamma_{p}^{p}}}{\gamma^{p}+\gamma_{p}^{p}}\right)\sin(\psi_{peak})\right] \tag{3.14}$$

Post -peak region:

$$\phi' = \phi'_{critical} + exp\left[-\left(\frac{\gamma^{p}-\gamma_{p}^{p}}{\gamma_{c}^{p}}\right)^{2}(\phi'_{peak} - \phi'_{critival})\right] \tag{3.15}$$

$$\psi = exp\left[-\left(\frac{\gamma^{p}-\gamma_{p}^{p}}{\gamma_{c}^{p}}\right)^{2}\psi_{peak}\right] \tag{3.16}$$

where γ_{c}^{p} is a strain softening parameter and C1= 0.22, C2= 0.11

γ_{p}^{p} is the plastic strain at ϕ'_{peak} and m=0.25

Figure 3.17 shows the variation of the internal friction angle (ϕ') as a function of the field variables for the different regions. Similarly, the variation of the dilation angle (ψ) is shown in Figure 3.18.

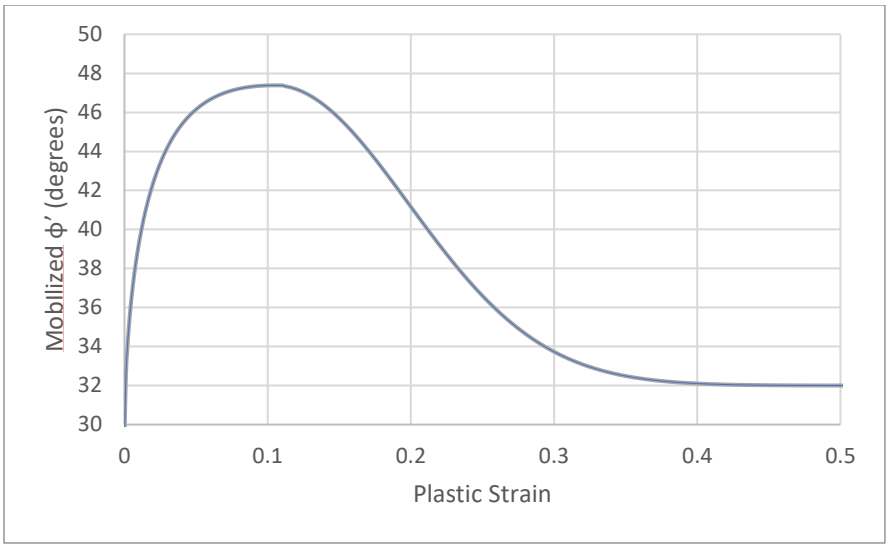

Figure 3.17: Friction angle (ϕ') variation as a function of field variables.

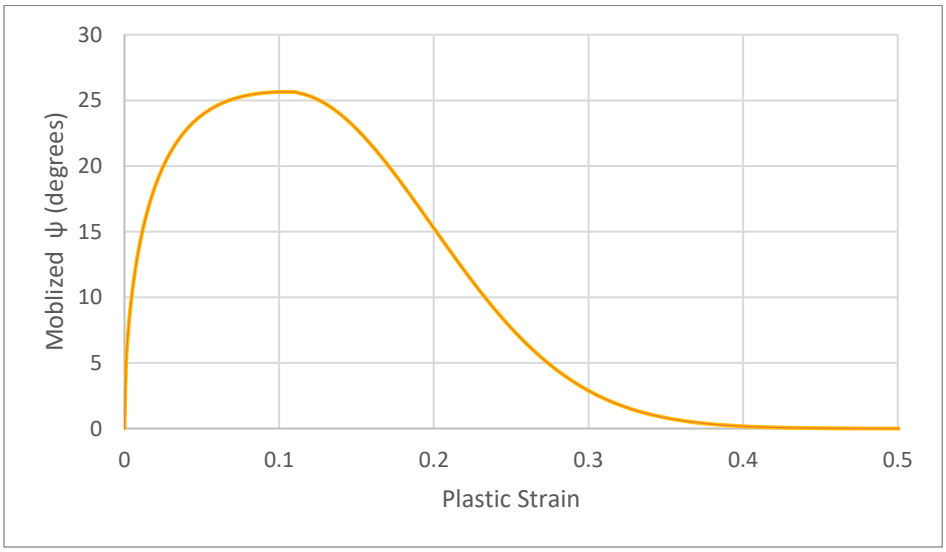

Figure 3.18.: Dilation angle (ψ) variation as a function of field variables.

3.2.7 Nonlinearity and convergence issues

In general, the response of the system is nonlinear however sometimes the response can be approximated as a linear response. Nonlinearity can be a result of geometric nonlinearity, material nonlinearity, and/or boundary constrains.

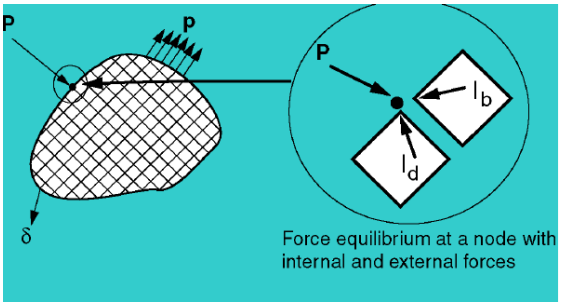

Figure 3.19: Force equilibrium at a node. Reprinted from [ABAQUS, 6.14]

The system of equations representing the static equilibrium is given by the following equation:

$$P - I = 0 \tag{3.17}$$

Where *P* is the applied load, and *I* is the internal forces

$$I=\int_V \beta^T \sigma \, dV \tag{3.18}$$

ABAQUS has several techniques to solve nonlinear systems of equations that give an approximate solution rather than an exact solution. These methods use the same concept of dividing the load into smaller load increments then solve the system of equations for each increment. The two common methods used in Abaqus are Newton-Raphson and Quasi-Newton. The main difference between the two methods is that Quasi-Newton does not recalculate the stiffness matrix in every iteration but instead it recalculates it once every eight iterations.

Quasi-Newton is more efficient in terms of computational effort however its main limitation is that it cannot be used with unsymmetric problems which is the case in this study.

Newton-Raphson method:

Newton-Raphson method is one of the most robust methods used in ABQUS. This technique uses iterations and incrementations to find a solution and it is unconditionally stable. In Newton-Raphson, equation 3.19 is rewritten as:

$$k_{tangent} c_u = P - I \tag{3.19}$$

Where c_u is the displacment correction which is used to update the incremental displacement

$$u_{i+1} = u_i + c_u \tag{3.20}$$

There are two checks used in ABAQUS to decide if a converged solution has been obtained or not.

1- The maximum residual which is sum of all forces acting on a node.

2- The displacement correction.

These two quantities must be within tolerance for the solution to be accepted by ABAQUS before it moves to the next increment. The two checks are local convergence criteria which compared to the global check are considered more conservative and likely to yield a correct solution.

Check 1

The maximum residual (Rmax), ABAQUS tolerance is 0.5% of the time average force.

$$\text{Rmax} <= 0.5\% \ \hat{q}$$

Where

$$\hat{q} = \frac{\text{Sum of all previous q for converged iterations}}{\text{number of increments in the step}}$$

Once the residual check is satisfied, ABAQUS checks if the displacement correction is within tolerance wish is 1% of the maximum incremental displacement. (c_{umax}< 1% Δu_{max}). If either of the convergence checks is not satisfied ABAQUS will start a new iteration and continue the iteration process until an acceptable converged solution is obtained for that load increment if not then ABAQUS will initiate a new attempt where it uses a smaller load increment. The flow chart in Figure 3.20 explains the solution procedure and shows how ABAQUS moves between loops.

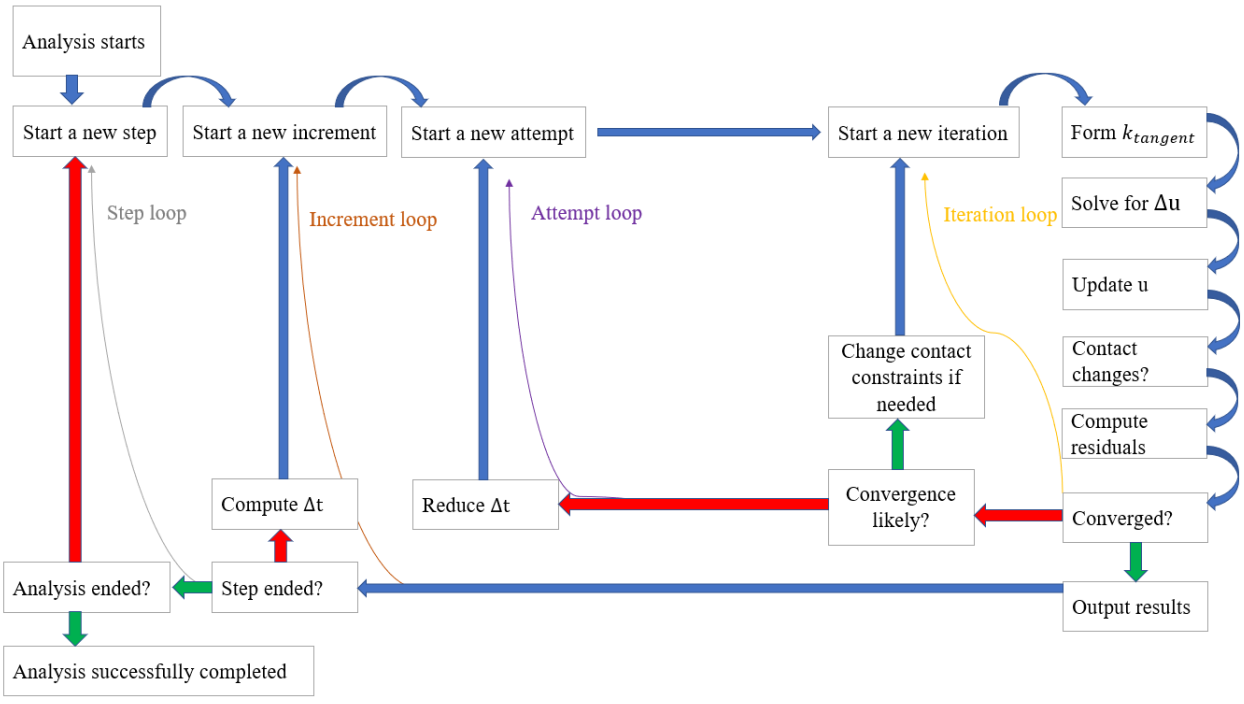

Figure 3.20: Abaqus solution procedure.

3.2.8 Numerical Model Validation

The finite element model was validated against a series of centrifuge tests on a model caisson anchor in sand conducted by the Daewoo Institute of Construction Technology, Bang *et al.* (2011).

Bang conducted centrifuge tests for a caisson anchor embedded in a dense sand soil. Different loading conditions were considered for the caisson anchor model in the centrifuge tests including lateral loading and inclined loading cases. Bang loading conditions are ideal to validate the finite element model results against all the different loading conditions. Figure 3.21 shows Bang centrifuge tests setup and the pull-out loading system. A model caisson anchor and the mooring line connection are shown in Figure 3.22(a) while Figure 3.22(b) shows the caisson anchor model after being loaded to failure.

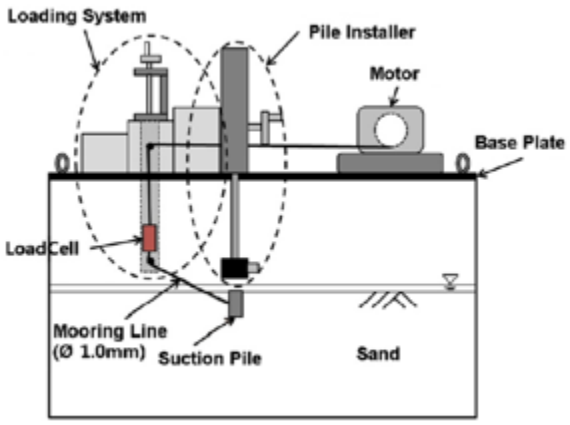

Figure 3.21: Pull-out loading system. Reprinted from [Bang et al. 2011]

Figure 3.22: (a) A model caisson anchor and the mooring line connection. (b) a failed caisson anchor model. Reprinted from [Bang et al. 2011]

All the model parameters and material properties that are reported by Bang et al. (2011) for the centrifuge tests conducted by the Daewoo Institute of Construction Technology are summarized in Table 3.1. For the numerical model parameters, a negligible nominal cohesion of 1 kN/m^2 was used in the model to ensure numerical convergence. Another material property that was assumed in the numerical model is a critical state friction angle of 31° for the sand sample. The critical state friction angle was used in the initial stress calculations for the geostatic step.

Table 3.1: A summary of the parameters used in the analysis

Part	Property	Centrifuge tests	Numerical model
Caisson	Outer diameter (D)	3 m	3 m
	Length (L)	6 m	6 m
	Load attachment (Li. Lf)	5, 25, 50, 75, 95 %	5, 25, 50, 75, 95 %
	Load inclination angle (θ)	0, 22.5,45, 90°	0, 22.5,45, 90°
Sand	Friction angle (ϕ')	39°	39°
	Dilation angle (Ψ)	9°	9°
	Relative density, Dr (%)	-	70
	Poisson's ratio	0.3	0.3
	Critical state Friction angle (ϕ')	-	31°
	Cohesion (c)	-	1 kN/m^2
	Buoyant unit weight	8.2 kN/m^3	8.2 kN/m^3

Lateral loading

A caisson anchor with a diameter of 3 m and a length of 6 m was used in the numerical analyses to validate the model against the centrifuge test results. The model dimensions and load attachment depths are shown in Figure 3.23.

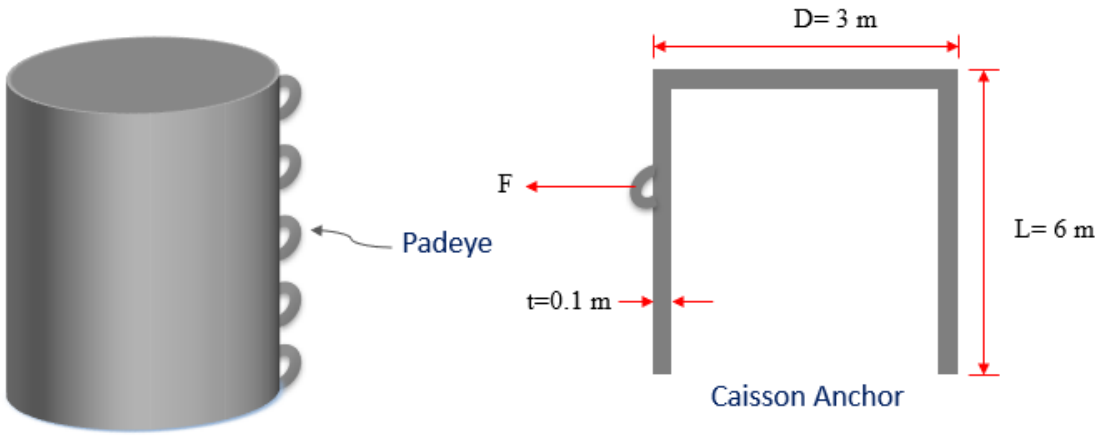

Figure 3.23: Caisson anchor dimensions and Padeye location.

Figure 3.24 shows the finite element model predictions using Mohr-Coulomb model with soil strength parameters estimated using Bolton equations. The numerical model estimations are compared to the centrifuge test results published by Bang *et al.* (2011). It can be noticed that the model is capable of estimating the ultimate horizontal capacity at different pad-eye locations and the results agree with the measured data from the centrifuge tests.

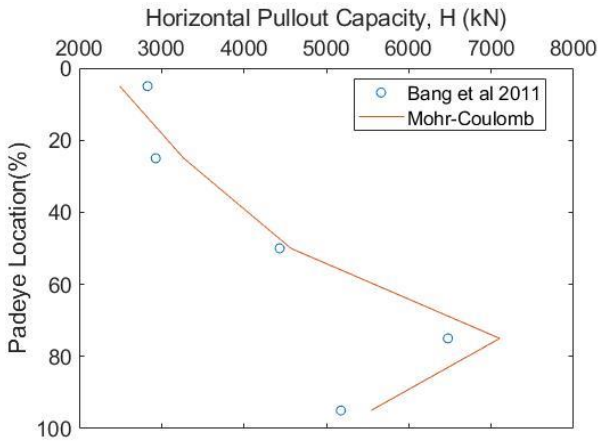

Figure 3.24: Ultimate lateral capacity of caisson anchor in sand.

For the same loading cases, the modified Mohr-Coulomb model using the USDFLD subroutine was used to predict the ultimate later load capacity of the caisson anchor in sand. The results from the modified Mohr-Coulomb model are compared to the centrifuge test results and the results obtained using Mohr-Coulomb model, Figure 3.25 It can be noticed that both models' estimates are close to the measured data reported by Bang *et al.* (2011). At the optimum attachment depth, the modified Mohr-Coulomb model yields a better prediction.

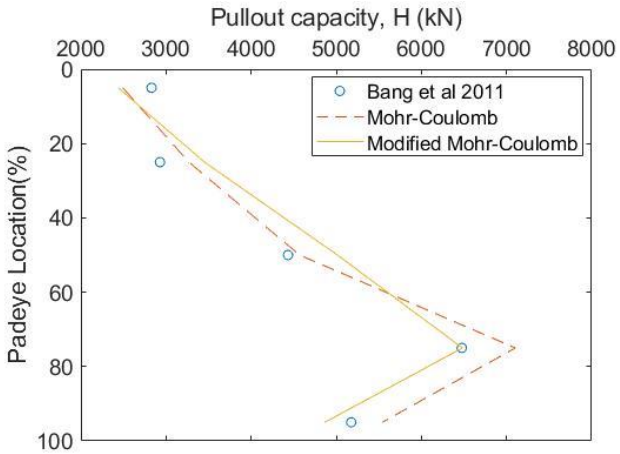

Figure 3.25: Ultimate lateral capacity of caisson anchor in sand using USDFLD and Mohr-Coulomb model.

Inclined loading

After the lateral load capacity, vertical and inclined load capacity predictions of the caisson anchor were compared to the centrifuge data results. Figure 3.26 shows the numerical model predictions and measured centrifuge data at load inclination angle (θ) = 0°, 22°.5,45°, and 90°.

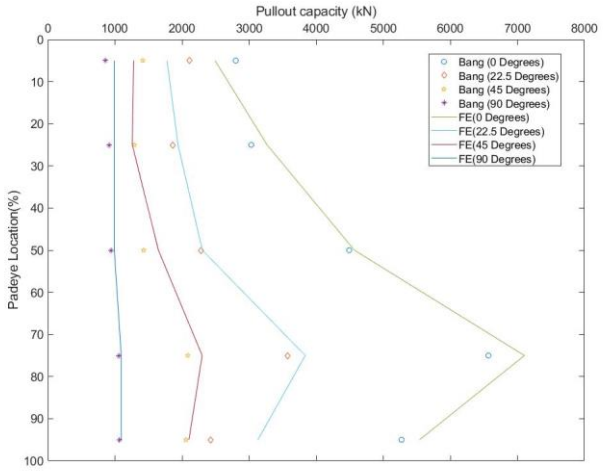

Figure 3.26: Ultimate capacity of suction anchor in sand under monotonic inclined loading.

3.3 Plastic limit Analysis

In this section a simplified method using an upper bound formulation of plasticity limit analysis is proposed to estimate the lateral load capacity of caisson anchor in sand. The plastic limit analysis model offers a quick estimate of lateral load capacity for the caisson anchor, and it provides an uncomplicated way to assess the effect of key parameters on the lateral capacity of caisson anchor.

The upper bound theorem uses a virtual velocity field to calculate an upper bound collapse load. The upper bound method requires postulating a kinematically admissible collapse mechanism. Figure 3.27 shows the virtual velocity field and failure mechanism. The rate of internal energy dissipation associated with the failure mechanism and the external work done by the anchor line are calculated then the collapse load is computed by optimizing the failure mechanism that

corresponds to the least upper bound estimate of the collapse load.

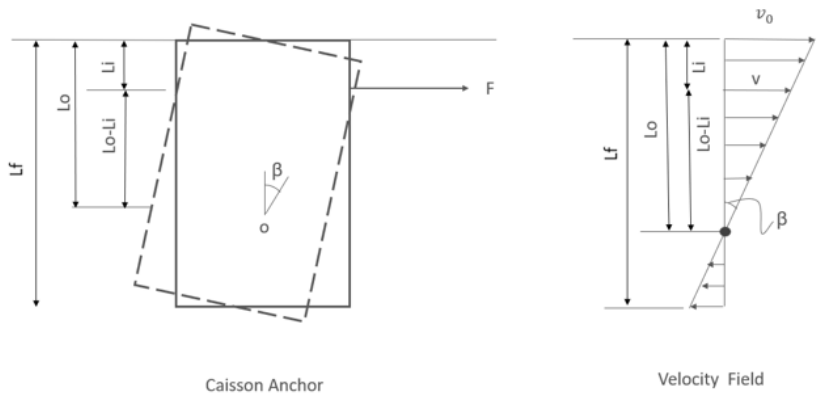

Figure 3.27: Velocity field.

The ultimate lateral resistance per unit length that soils can exert against the pile is a key quantity in the calculation of ultimate lateral capacity, Chen (1975). Different profiles for the unit lateral soil resistance in sands are adopted in this method where integration of pu along the caisson anchor side is used to generate an expression to compute the internal energy dissipation.

3.3.1. Unit lateral soil resistance in sands

As discussed earlier, the unit lateral soil resistance (P_u) is the primary component in estimating the lateral capacity of caisson anchor. Several approaches are available in the literature to calculate unit lateral soil resistance. The different approaches are primarily developed based on experimental test results. In this study, few selected methods are adopted in the simplified model. The equations developed by Broms (1964), Petrosovitz and Award (1972), Reese et al. (1974), and Prasad and Chari (1999) are presented next while details regarding the development of the

different methods were discussed earlier in Chapter 2.

Broms (1964)

Broms method is a widely used approach in practice. The method assumes the pile will rotate around its base and it employs the passive lateral stress ratio from Rankine theory to estimate the unit lateral soil resistance (Pu). Figure 3.3.1.1 shows the lateral soil pressure distributions at ultimate state. The unit lateral soil resistance (Pu) in Broms' method is given as follows:

$$Pu = 3\ Kp\ \gamma' z\ D \tag{3.21}$$

Where: Kp is the coefficient of passive earth pressure (equation 3.22)

γ' is soil buoyant unit weight

D is the caisson anchor diameter

$$Kp = \tan^2\left(45 + \frac{\varphi'}{2}\right) \tag{3.22}$$

Petrasovtiz and Award (1972)

In their method, Petrasovtiz and Award consider the active earth pressure and its influence on the lateral soil pressure. As shown in Figure 3.3.1.1, Petrasovtiz and Award assume a point of rotation within the pile at which the active and passive stress reversal happen. Estimating the unit lateral soil resistance (Pu) in Petrasovtiz and Award's method is given as follows:

$$Pu = 3.7(Kp - Ka)\ \gamma' z\ D \tag{3.23}$$

Where: Kp is the coefficient of passive earth pressure (equation 3.22)

Ka is the coefficient of active earth pressure (equation 3.24)

γ' is soil buoyant unit weight

D is the caisson anchor diameter

$$\text{Ka} = \tan^2(45 - \frac{\varphi'}{2}) \quad (3.24)$$

Prasad & Chari (1999)

Prasad & Chari method is the most recent approach out of the four methods considered in this study. Their method is similar to Petrasovtiz and Award's method in the way that it assumes a point of rotation within the pile at which the active and passive stress reversal happen. Estimating the unit lateral soil resistance (P_u) in Prasad & Chari's method is given as follows:

$$P_u = 10^{(1.3\tan\varphi + 0.3)}\gamma' z\, D \quad (3.25)$$

Reese, Cox, and Coop (1974)

The method developed by R-C-C is based on a series of tests in the field for two piles loaded horizontally in sand. The method takes the smaller quantity of p_u based on the following two equations:

$$P_{st} = \gamma' z \left[\frac{k_0 \tan\varphi' \sin\beta}{\tan(\varphi'-\beta)\cos\alpha} + \frac{\tan\beta}{\tan(\varphi'-\beta)}(b + z\tan\beta\tan\alpha) + k_0 z \tan\beta\,(\tan\varphi' \sin\beta - \tan\alpha) - k_a b \right] \quad (3.26)$$

$$P_{sd} = k_a b\,\gamma' z\,(\tan\beta^8 - 1) + k_a b\,\gamma' z\,\tan\varphi'\tan\beta^4 \quad (3.27)$$

Reese, Cox, and Coop equations can be simplified and rewritten as shown in the next equation

$$P_u = (c_1 + c_2 \frac{z}{D})\,\gamma' z\, D < c_3\,\gamma' z\, D \quad (3.28)$$

Whiteside (1995) proposed simplified empirical fits for parameters c_1, c_2, and c_3 as follows

$$c1 = 0.124 \exp(0.091\varphi)$$

$$c2 = 0.58\exp(0.051\varphi)$$

$$c3 = 0.73\exp(0.123\varphi)$$

The equations for the different methods are summarized in Table 3.2 and the soil pressure distributions are shown in Figure 3.28.

Table 3.2: The unit lateral soil resistance equations in sand.

Broms (1964)	$P_u = 3\ Kp\ \gamma' z\ D$
Petrasovtiz and Award (1972)	$P_u = 3.7(Kp\text{-}Ka)\ \gamma' z\ D$
Prasad & Chari (1999)	$P_u = 10^{(1.3tan\varphi\ +0.3)}\gamma' z\ D$
Reese, Cox, and Coop (1974)	$P_u = (C1+C2\ \frac{z}{D})\ \gamma' z\ D < C3\ \gamma' z\ D$

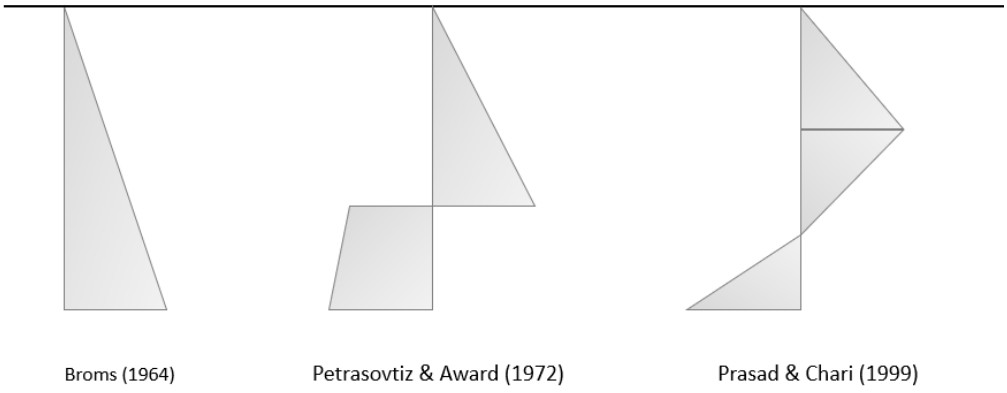

Figure 3.28: Soil Pressure distribution under lateral load.

3.3.2. Internal Energy dissipation for side resistance

The rate of energy dissipation for side resistance of the caisson anchor per unit length is the lateral soil resistance (section 3.3.1) times the virtual velocity times the projected side area. The rate of internal energy dissipation along the side of the caisson is given by equation 3.29

$$\dot{dE} = puvDdz \tag{3.29}$$

The total rate of energy dissipation is then computed by integrating equation 3.30 over the length of the caisson anchor

$$\dot{D_s} = \int_0^L v\ pu\ D\ dz = v_0 D \int_0^L \left[\gamma'\ z_i\ (3.7K_p - K_a) \left|\left(1 - \frac{z}{Lo}\right)\right|\right] dz \tag{3.30}$$

Where: v is velocity

P_u is lateral soil resistance; Petrasovtiz and Award (1972) definition of Pu is used as an example.

D is caisson anchor diameter

3.3.3. Internal Energy dissipation for tip resistance

For the soil resistance at the caisson tip, Aubeny and Murff (2003) proposed a failure mechanism that adopts a rigid rotating spherical soil mass at the bottom of the caisson failing on a compatible slip surface, is shown in Figure 3.29. To generate an expression for the rate of internal energy dissipation for the tip resistance; equation 3.31 is used.

$$S_d = (\chi W_{net}/A_{tip} + \gamma' L_f) \tan \phi' \quad (3.31)$$

Where: χ is a parameter that consider the caisson weight transmitted to the soil.

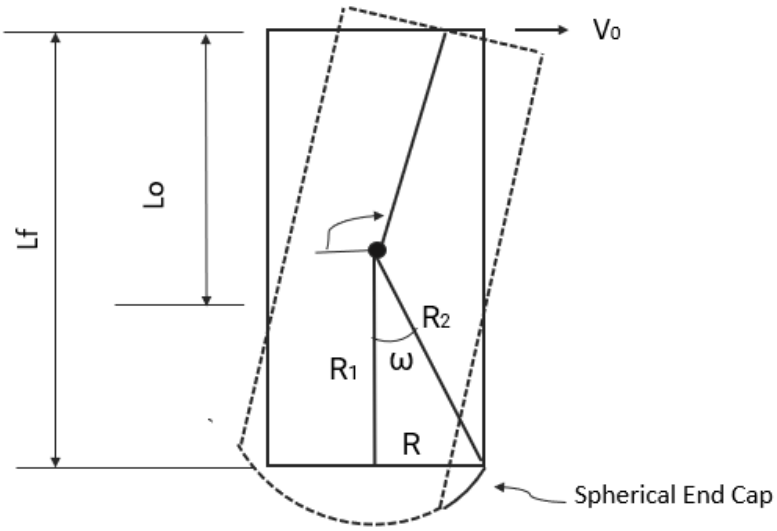

Figure 3.29: Failure mechanism at the caisson tip.

Aubeny and Murff (2003) presented a dimensionless expression for Murff and Hamilton (1993) solution:

$$\frac{M_{b0}}{0.5\pi^2 R^3 S_d} = 2\left(\frac{R1}{\pi R}\right) + \left(\frac{-I4\ R1}{R}\right) \quad (3.32)$$

where, $Rl = Lf - L0$
$R = D/2$
$I4 = 1.118$
$S_d = (\chi W_{net}/A_{tip} + \gamma' L_f) \tan \phi'$

3.3.4 External work and lateral load capacity

Equating the external work from load (*F*) to internal dissipation energies and canceling virtual velocities, we get:

$$F = \frac{D_s + D_e}{\left|1 - {}^{L_i}/_{L_0}\right|} \tag{3.33}$$

3.3.5 PLA Model calibration

The same set of measured data from the series of centrifuge tests conducted by the Daewoo Institute of Construction Technology were used to validate the Plastic limit analysis (PLA) predictions. PLA estimates for the lateral capacity of the caisson anchor in sand are shown in Figure 3.30.

The predictions of the four different methods in PLA are compared to finite element analysis results and measured data. It can be noticed from the plot that Reese, Cox, and Coop (1974) predictions underestimate the capacity which can be attributed to the fact that the equation was built through calibration to long piles which is different than the short rigid piles investigated in this study.

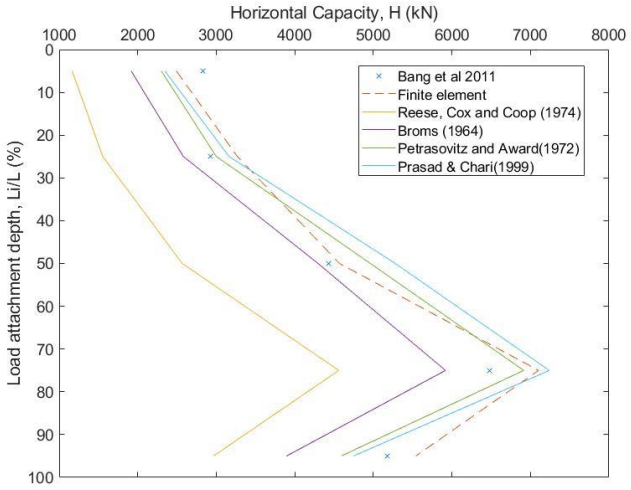

Figure 3.30: PLA and FE predictions for ultimate lateral capacity of caisson anchor in sand.

PLA predictions were also validated against another set of measured data for a series of model tests was conducted in sand Gao *et al.* (2013). Figure 3.31 shows a schematic of the model test and different load attachment depths that were considered. All the model parameters and material properties that are reported by Gao et al. (2013) for the physical tests are summarized in Table 3.3.

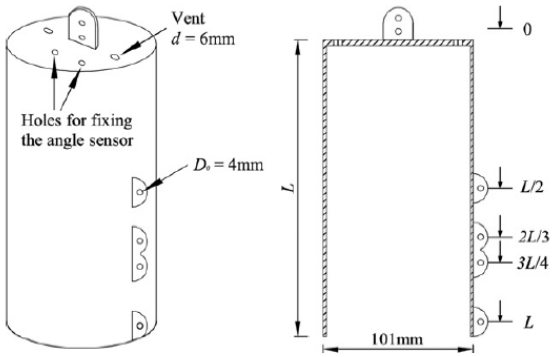

Figure 3.31: Anchor model and different load attachment depths. Reprinted from [Gao et al., 2013]

Table 3.3: A summary of the parameters used in the analysis

Part	Property	Model test	PLA model
Caisson	Aspect ratio	2	2
	Load attachment (Li/Lf)	0,1/2,2/3,3/4,1	0,1/2,2/3,3/4,1
Sand	Friction angle (ϕ')	36.7°	36.7°
	Poisson's ratio	0.3	0.3
	Buoyant unit weight	10 kN/m^3	10 kN/m^3

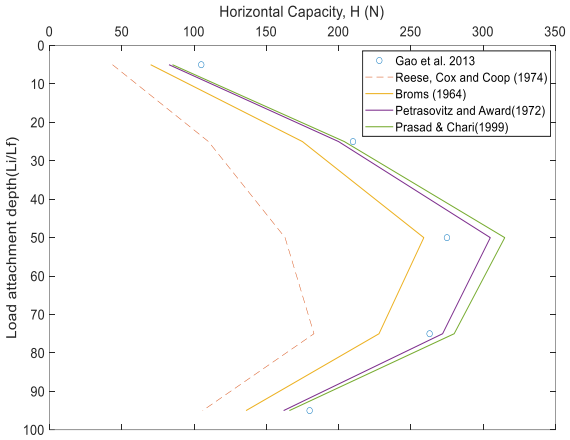

Figure 3.32: PLA predictions for ultimate lateral capacity of caisson anchor in sand.

3.4 Parametric study

After the models were validated by comparing their results to measured data, the models then are utilized in the scope of a parametric study to investigate the effect of key parameters on the monotonic ultimate capacity of a caisson anchor embedded in sand. The research matrix was built to evaluate the effect of load attachment depth (L_i), Load inclination angle (θ), and soil strength parameters internal friction angle (ϕ) and dilation angle(ψ).

The results are presented by normalizing the ultimate load capacity for ease of comparison and to follow the trends and relationships of the anchor behavior under the different load cases and model parameters. The ultimate load capacity of the caisson anchor is divided by the vertical

effective stress (σ_v) and the area that acts on which is represented by the caisson anchor diameter (D) and the anchor length (L).

$$N_h = \frac{H}{\sigma_v D\, L} \tag{3.34}$$

Where N_h is the normlized lateral capacity of the caisson anchor.

H is the lateral load.

σ_v is the verical effective stress.

D is the caisson anchor diameter.

L is the caisson anchor length.

3.4.1 The effect of load attachment depth on ultimate capacity

The load attachment depth or the pad-eye location has a major effect on the ultimate capacity of the caisson anchor as it was reported by multiple studies (Bang et al, 2011, Gao *et al.* ,2013, and Zhao *et al.*, 2019). In this study, the effect of the load attachment depth will be investigated as an independent parameter and as part of the other parameters in the research matrix.

The load attachment depth is defined as a ratio where the load attachment depth (L_i) is divided by the total anchor length (L_f). Figure 3.33 shows the expected trend of the lateral load capacity at different load attachment depths. The later load capacity increases when the padeye location moves from the top of the caisson anchor towards the bottom of the anchor until it reaches its maximum capacity at a certain point after that the lateral capacity starts to decrease. The maximum lateral ultimate capacity occurs at the optimum load attachment depth. One characteristic of the optimum padeye location is that there is no rotation and loading is purely translational. The optimum load attachment depth for caisson anchor is located between Li/Lf= 0.6 and 0.7.

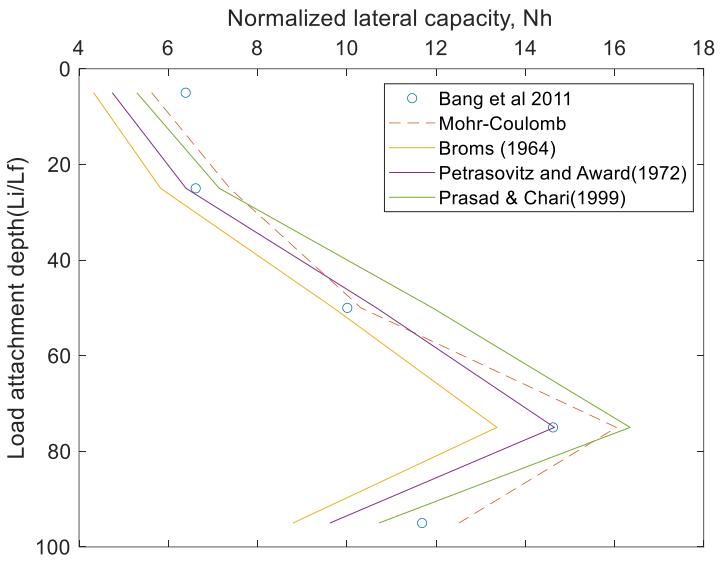

Figure 3.33: Ultimate lateral capacity at different load attachment depths.

A caisson anchor with diameter of 3 m and a length of 9 m was used to further investigate the load attachment depth effect on the ultimate lateral load capacity and to define the optimum padeye location. A schematic of the model dimensions and load attachment depths are shown in Figure 3.34. Model parameters and material properties that were used in the analysis are summarized in Table 3.4.

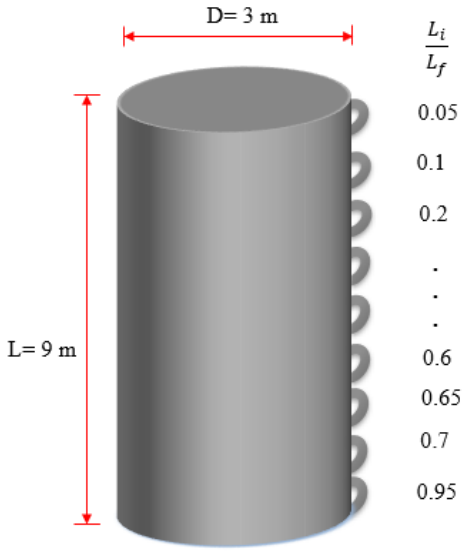

Figure 3.34: Model dimensions and load attachment depths.

Table 3.4: A summary of the parameters used in the analysis

Part	Property	
Caisson	Outer diameter (D)	3 m
	Length (L)	9 m
	Load attachment (Li/Lf)	5, 10, 20,30,40,50,60,64,65,66,68,70, 75, 95 %
Sand	Friction angle (ϕ')	39°
	Dilation angle (Ψ)	9°
	Relative density, Dr (%)	70
	Poisson's ratio	0.3
	Critical state Friction angle	31°
	Cohesion (c)	1 kN/m^2
	Buoyant unit weight	8.2 kN/m^3

The reults are shown in Figure 3.35. The maximum ultimate lateral load capcity corresponds to Li/Lf of 0.68 which represents the optimum load attahcment depth (L_{opt}). The effect of the padeye location will be further assessed during the analyses perfumed to invistages the effect of the aspect ration and the soil strenth paramters friction angle (ϕ) and dilation angle(ψ).

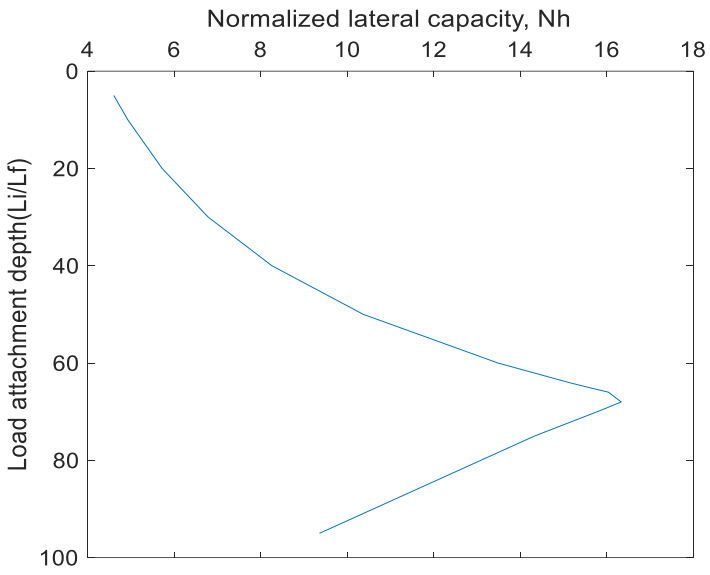

Figure 3.35: Ultimate lateral capacity at different load attachment depths.

3.4.2 Soil strength parameters: internal friction angle (ϕ) and dilation angle(ψ)

For cohesionless soils as the one considered in this study, the internal friction angle (ϕ) and dilation angle(ψ) define the strength behavior of the soil and as a result they have a significant impact on the ultimate load capacity of the caisson anchor. The dense sand behavior is the prime interest in this study, however, to better understand the effect of the soil strength parameters on the ultimate capacity and failure behavior, three different soil relative densities were considered. The different soil densities represent the different states of medium, medium dense, and dense sand. Bolton equations were used to generate a soil profile for the soil strength parameters. The soil strength parameters used in the analyses are presented in Table 3.5.

Table 3.5: A summary of the parameters used in the analysis.

	Friction angle (ϕ')	Dilation angle (Ψ)
Medium dense	36°	5°
Dense	41°	11°
Very dense	45°	15°

The results for the three soils using the numerical and plastic limit analysis models are presented in Figure 3.36 to Figure 3.38. Regardless of the soil strength parameters, the trend for load attachment depth holds true throughout the different analyses.

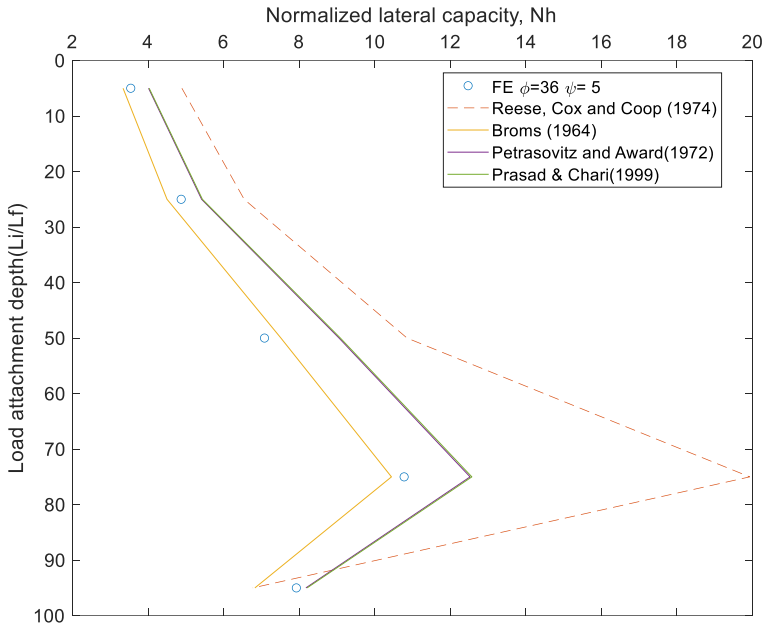

Figure 3.36: The ultimate lateral capacity of the caisson anchor (ϕ'= 36° and Ψ = 5°).

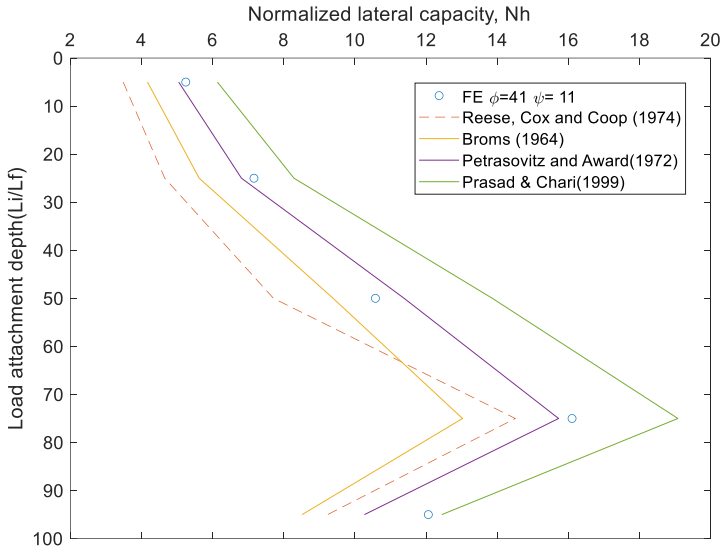

Figure 3.37: The ultimate lateral capacity of the caisson anchor (ϕ'= 41° and Ψ = 11°).

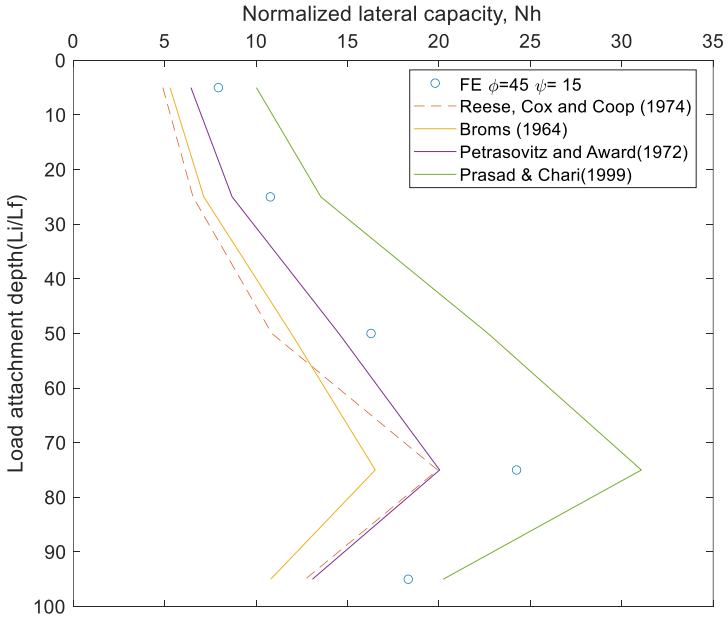

Figure 3.38: The ultimate lateral capacity of the caisson anchor (ϕ'= 45° and Ψ = 15°).

3.4.3 Aspect Ratio

The effect of the aspect ratio on the ultimate capacity of the caisson anchor was evaluated. Three aspect ratios were considered L/D=2,4, and 6. A summary of the parameters used in the analysis is shown in Table 3.6.

Table 3.6: A summary of the parameters used in the analysis

Part	Property	Model test	PLA model
Caisson	Aspect ratio	2,4,6	2,4,6
	Load attachment (Li/Lf)	0,1/2,2/3,3/4,1	0,1/2,2/3,3/4,1
Sand	Friction angle (ϕ')	36.7°	36.7°
	Poisson's ratio	0.3	0.3
	Buoyant unit weight	10 kN/m^3	10 kN/m^3

Figures 3.39 to 3.41 show the results compared to lab tests data reported by Gao *et al.* (2013). PLA model predictions follow the trend and Petrasovitz and Award tend to yield a better estimate compared to the other methods. Near the optimum attachment depth (Li/Lf =2/3), Petrasovitz and Award's estimates are in a good agreement with the measured data.

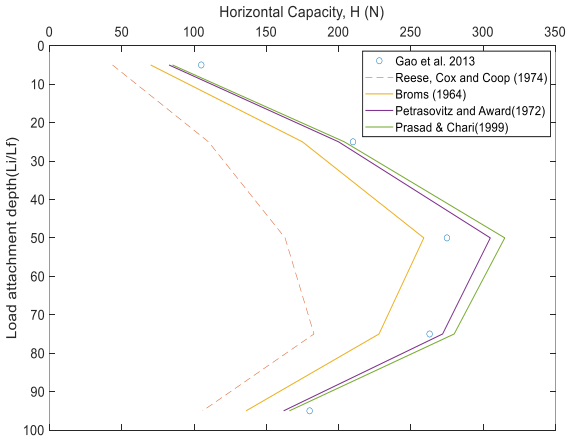

Figure 3.39: Caisson anchor ultimate capacity for L/D=2.

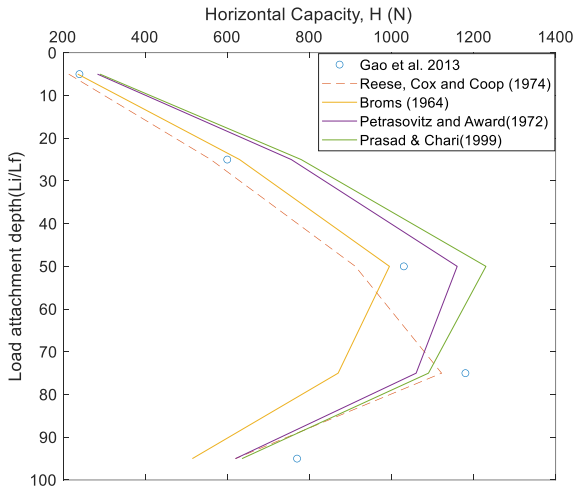

Figure 3.40: Caisson anchor ultimate capacity for L/D=4.

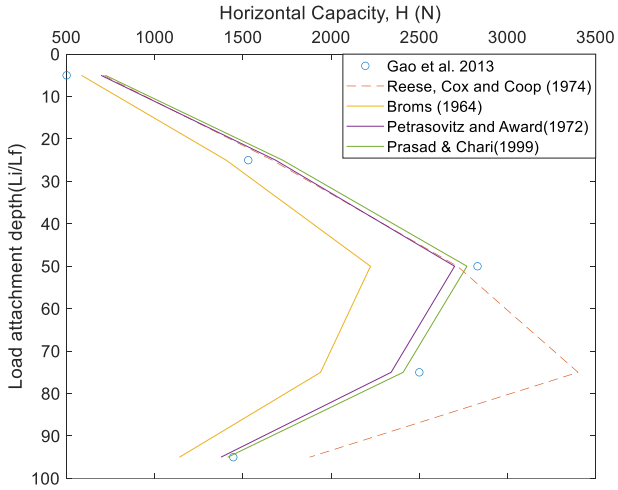

Figure 3.41: Caisson anchor ultimate capacity for L/D=6.

3.4.4 Load inclination angle

The load inclination angle has a major effect on the ultimate capacity of the caisson anchor as it was reported by (Bang et al, 2011and Zhao *et al.*, 2019). In this study, the effect of load inclination angle was investigated where the capacity of the caisson anchor was estimated at different inclined angles ranging between pure lateral (θ =0°) and pure axial (θ =90°). A summary of the parameters used in the analyses are presented in Table 3.7.

Two aspect ratios were considered (L/D=2 and L/D=3). Figure 3.42 shows the results for the ultimate capacity of the caisson anchor for θ=0°,10°,30°,45°,60°,80°, and 90°. The trend observed in the results is that the ultimate capacity deceases as the inclination angle increases. However, the interaction diagram shown in Figure 3.42 indicates that the ultimate capacity start declining even at lower inclination angle values. Zhao *et al.* (2019) findings conform the trend observed in Figure 3.42.

Table 3.7: A summary of the parameters used in the analysis.

Part	Property	
Caisson	Outer diameter (D)	3 m
	Length (L)	6 m
	Load inclination angle(θ)	0°,10°,30°,45°,60°,80°,90°
Sand	Friction angle (ϕ')	39°
	Dilation angle (Ψ)	9°
	Relative density, Dr (%)	70
	Poisson's ratio	0.3
	Critical state Friction angle	31°
	Cohesion (c)	1 kN/m^2
	Buoyant unit weight	8.2 kN/m^3

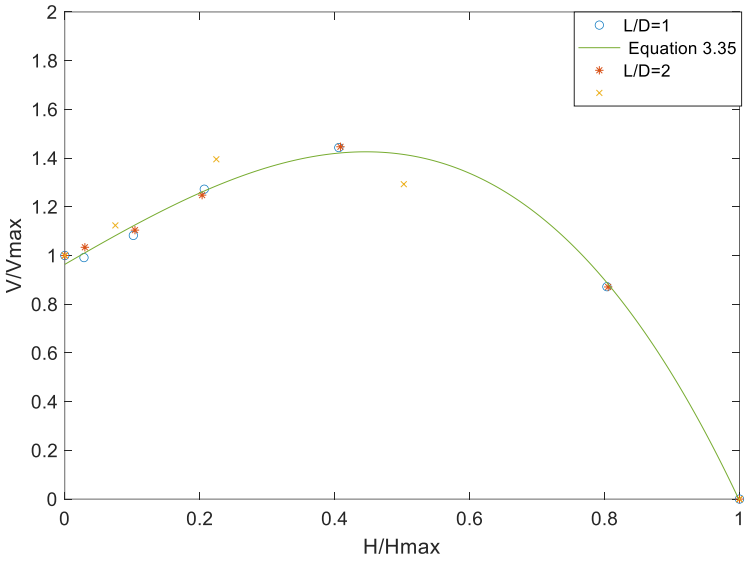

Figure 3.42: Inclined load capacity of the caisson anchor.

From the finite element results, an expression to estimate the ultimate inclined capacity of the caisson was obtained. Equation 3.35 is shown in Figure 3.42.

$$\left(\frac{V}{Vmax}\right) = a\left(\frac{H}{Hmax}\right) - b\left(\frac{H}{Hmax}\right)^2 - c\left(\frac{H}{Hmax}\right)^3 + 1 \qquad (3.35)$$

Where a= 1.604

b=0.2248

c=2.35

3.5. Conclusion

The caisson anchor behavior in sand was investigated and the lateral and inclined ultimate capacities of the caisson anchor were estimated by utilizing a three-dimensional finite element model and a plastic limit analysis model. The models were validated by comparing their predictions to centrifuge and lab tests. The numerical model was utilized in the scope of a parametric study to investigate the effect of load attachment depth (Li), Load inclination angle (θ), aspect ratio and soil strength parameters.

For the lateral ultimate capacity of the caisson anchor, the effect of load attachment depth (padeye position) on the ultimate capacity was studied where different attachment depths were considered. The padeye location was optimized to find the optimum load attachment depth that corresponded to the maximum capacity which occurs when the rigid caisson anchor is under translational motion (no rotation). The maximum ultimate lateral load capcity was found to be at Li/Lf of 0.68 which represents the optimum load attahcment depth (L_{opt}).

The effect of the caisson anchor aspect ratio and load inclination angle were also examined. The analysis results showed that load inclination angle (θ) has a major effect on the ultimate load capacity of the caisson anchor even at low load inclination angle values from the horizontal.

The simplified PLA model presented in this study showed a good agreement when compared to measured data from centrifuge and lab tests. Despite the simplifications in the model components, it is capable of providing a quick estimate of lateral load capacity for the caisson anchor at different load attachment depths and aspect ratios to a sufficient accuracy.

CHAPTER IV

ULTIMATE CAPACITY OF MULTILINE RING ANCHOR IN SAND UNDER LATERAL LOADING CONDITIONS

4.1. Introduction

The untapped offshore wind resources in deep waters make the floating offshore wind (FOWT) technology a primary choice for renewable energy. However, the high levelized cost of energy (LCOE) for the technology needs to undergo significant reduction to be commercially competitive. Some new innovative anchoring solutions have been proposed in the literature including the Multiline Ring Anchor (MRA) concept. MRA is a novel shared anchor concept comprises of a ring connected to multiple mooring lines which results in reduction in the total number of anchors, MRA concept is shown in Figure4.1. MRA has the applicability to be installed in wide range of soil type (Fontana *et al.*, 2018).

This chapter focuses on Multiline Ring Anchor (MRA) behavior in sand and aims to evaluate the foundation as an anchoring solution for offshore floating wind turbines. The three-dimensional finite element model developed in chapter 3 was modified to model to the new anchor type and the numerical model was used to estimate the lateral ultimate capacity of the MRA. In addition to the numerical model, a simplified plastic limit analysis (PLA) model is proposed to estimate the lateral load capacity of MRA in sand.

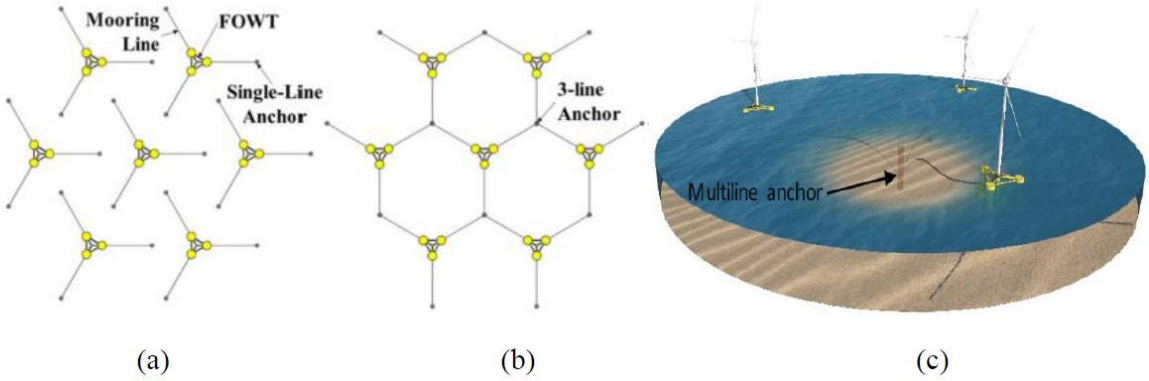

Figure 4.1: Layout of (a) single-line; (b) 3-line anchor; (c) multiline anchor concept. Reprinted from [Fontana et al., 2018]

MRA capacity in sand can theoretically be increased by increasing the anchor diameter or installing the MRA deeper. Therefore, the anchor diameter and embedment depth are two key parameters in the research matrix that was built to evaluate MRA behavior in sand.

4.2 Numerical Model

The three-dimensional finite element model developed in chapter 3 was modified to model the new anchor type. The model adjustments include new ring structure for the MRA, new contact definitions, a built-in embedment depth parameter for the MRA, and other changes regarding the material model parameters. In this section, details regarding the development of the finite element model in ABAQUS and all modifications made are discussed.

4.2.1 Model Geometry and boundary conditions

The numerical model mesh, geometry, and boundary conditions are described in this section. Figure 4.2 shows the mesh of the finite element model used to model the MRA before refinement was applied to the MRA vicinity. The mesh is generated by a MATLAB code to be able to utilize the numerical model in a matrix of parametric studies. The code consists of four

parts: mesh generator, material model, interaction model, and loading model. One of the modifications to the mesh generator used in Chapter 3 is introducing an embedment depth parameter (z/D) which controls how deep the MRA needs to be. The embedment depth parameter (z/D) corresponds to the bottom tip of the MRA. As mentioned in section 3.2.1, the mesh generator has added capabilities of refining certain sections of the model and controlling the element size and numbers for every part. To employ the zone refinement as has been done in Chapter 3; the embedment depth parameter (z/D) was used to track the zone of interest (i.e., soil elements around the MRA). Region refinement helps in building a refined mesh for a particular part in the domain that is of interest and a courser mesh for rest of the domain. The soil elements around the MRA both inside and outside are part of a refined mesh. Also, soil elements at both ends of the MRA are part of the refined mesh. Sensitivity analyses were completed to determine the refinement level and domain size, they are discussed later in this section.

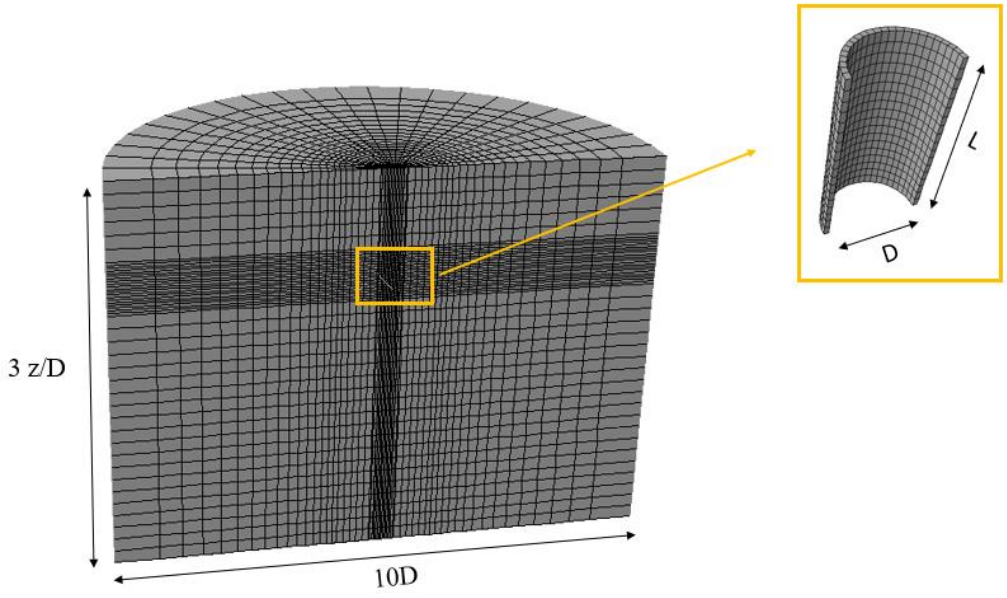

Figure 4.2: Finite- element mesh and domain dimensions.

Using the proper element type is crucial for obtaining correct and reliable solutions at an acceptable computational cost. The Solid continuum element C3D8 (8-node linear brick) was selected to mesh the soil medium. C3D8 is a three dimension fully integrated element. Figure 4.3 shows the node and integration points numbering for C3D8 element. ABAQUS provides some guidelines on element selections and recommends not to use C3D8 elements if the structure is under bending because results show that C3D8 can be stiff. Therefore, the MRA was meshed using an improved version of C3D8 which is C3D8I element. The incompatible mode eight-node brick element removes shear locking and reduce volumetric locking. ABAQUS enhances the shape functions used in C3D8 by using bubble functions that have a zero value at all nodes and non-zero values in between.

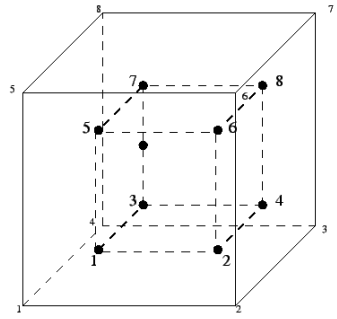

Figure 4.3: Nodes and integration points in C3D8 element.

Boundary conditions imposed on the model consists of two main boundary conditions (BCs). First, displacements are constrained on the far-field nodes for both of the horizontal directions (u_x, u_y). To impose the far-field boundary conditions, the infinite element CIN3D8 is used for the far-field elements. Such elements are available in ABAQUS element library to model problems in which the region of interest is small in size compared to the surrounding medium.

Second, displacements are restricted in all directions (u_x,u_y,u_z) for the bottom nodes of the model. Degrees of freedom 1,2, and 3 are restricted for all nodes at the bottom of the domain.

4.2.2 Material Modeling

The constitutive model Mohr-Coulomb was used to model the soil domain. Mohr-Coulomb is an elastic-perfectly plastic model used to represent shear failure in soils. The model is one of built-in models that are available in ABAQUS library. In the background chapter Mohr-Coulomb model was discussed and few features of the model were highlighted. Details on Mohr-Coulomb model implementation in ABAQUS were covered in Section 3.2.2.

4.2.3 Material properties and model parameters

As mentioned above, the soil was modeled as an isotropic elastic-perfectly plastic material using Mohr-Coulomb model available in ABAQUS library. In this section, the model parameters are discussed and the parameters selection to help correctly model the nonlinear soil response. To model the sand in ABAQUS, the linear isotropic elasticity model was used with Mohr-Coulomb model to represent the elastic regime. For the elasticity model, two parameters are required modulus of elasticity (E) and Poisson's ratio (ν). For Mohr-Coulomb model, friction angle (φ), dilation angle (ψ), and cohesion (c) are the required parameters. The soil considered in this study is cohesionless but to ensure numerical convergence low nominal cohesion value is assigned.

Modulus of elasticity (E)

As mentioned in section 3.2.3, A stress-dependent modulus of elasticity (E) must be considered to realistically model the nonlinearity in the soil response. Section 3.2.3 discussed few methods available in the literature to estimate the value of Young' modulus based on stress level.

The rigidity index approach proposed by Vesic (1972) was used in this chapter, defined by the following expression:

$$\mathrm{I_r} = \frac{\mathrm{E}}{[2(1+\upsilon)(\sigma \mathrm{v} * \tan\varphi)]} \qquad (4.1)$$

Where from equation (4.1), E can be computed as follows:

$$E = Ir * [2(1+\upsilon)(\sigma v * tan\varphi)] \qquad (4.2)$$

where, E = Young' modulus
Ir = Rigidity index (from Figure 4.4)
υ = Soil Poisson's ratio
σ_v = Vertical effective stress
φ = Angle of peak internal friction

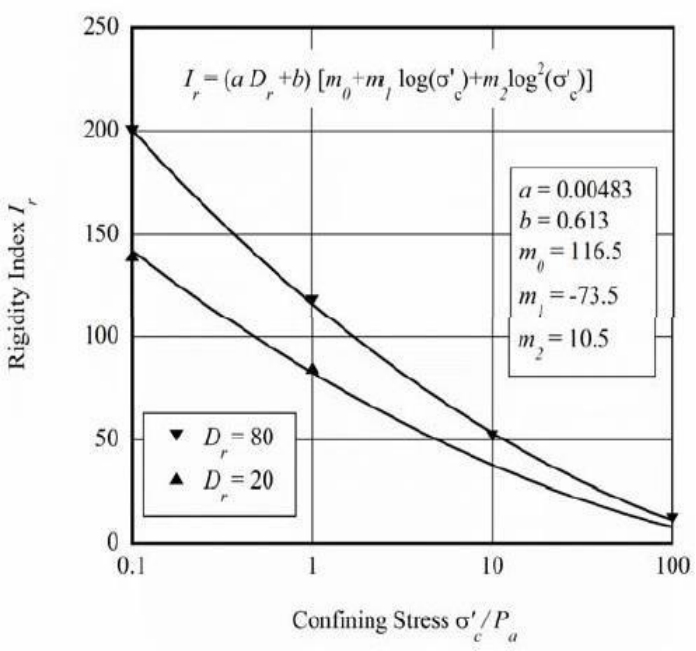

Figure 4.4: Rigidity index vs. confining stress. Reprinted from [Al Hakeem and Aubeny 2019]

Poisson's ratio (ν)

In elastic material deformations, Poisson's ratio defines the ratio deformation perpendicular to the direction of a normal loading. to. Generally, for a homogeneous and isotropic soil, the Poisson's ratio varies in the range $0 \leq \nu \leq 0.5$. For the medium to dense sand soil considered in this study a Poisson's ratio (ν) equals 0.3 is used.

Mohr-Coulomb Plastic Parameters

Mohr-Coulomb model has three plastic parameters which are friction angle (φ), dilation angle (ψ), and nominal cohesion (c). Sand is cohesionless (c=0); however, for the numerical model to avoid convergence issues a low value of nominal cohesion is required. In this study a small cohesion of 1 kPa was used.

The friction angle (φ) and dilation angle (ψ) are both a function of soil density and stress level. Thus, a soil profile was created where friction angle (φ) and dilation angle (ψ) are generated using Bolton equations to incorporate the effect of soil density and stress level. Bolton equations were discussed in detail in Chapter 2 and section 3.2.3 but for clarity the main points are reiterated here.

Bolton (1986) found that equation 4.3 can be used to estimate the peak friction angle for both plane-strain and triaxial compression conditions.

$$\varphi_{peak} = \varphi_{critical} + A\psi\, I_R \qquad (4.3)$$

Where $\varphi_{critical}$ is the critical state friction angle

$A\psi = 3$ for triaxial condition and 5 for plane strain condition.

I_R is a relative dilatancy index estimated from equation (4.4).

$$I_R = D_r (10 - \ln p) - 1 \quad (4.4)$$

After calculating the peak friction angle, the peak dilation angle can be estimated using the following equation:

$$\varphi_{peak} - \varphi_{critical} = 0.8\ \psi_{peak} \quad (4.5)$$

Soil-MRA interface friction angle (δ)

The Coulomb friction model was used to model the MRA-soil interface. The contact model itself is discussed in the next section. The main parameter for the contact model is the friction factor (μ) which depends on the soil-MRA interface friction angle (δ). There are few factors that effect the value of the interface friction angle such as MRA surface roughness, size and shape of soil particles and soil gradation. In section 3.2.3, the interface friction angle was reviewed and a couple of studies that investigated the effect of the different factors were presented (Han *et al.* ,2018 and Huang *et al*., 2019).

Huang *et al*. (2019) examined the effect of load inclination angle and surface roughness on the ultimate capacity of rigid piles in sand. Figure 4.5 shows that for load inclination angles greater than 45° the effect of surface roughness is pronounced. However, it can be noticed that surface roughness has a minimal effect on the capacity for the lateral load case. Since the prime interest of this study is the lateral load capacity of the MRA a soil-MRA interface friction angle (δ) of 0.6 φ was used in the analysis.

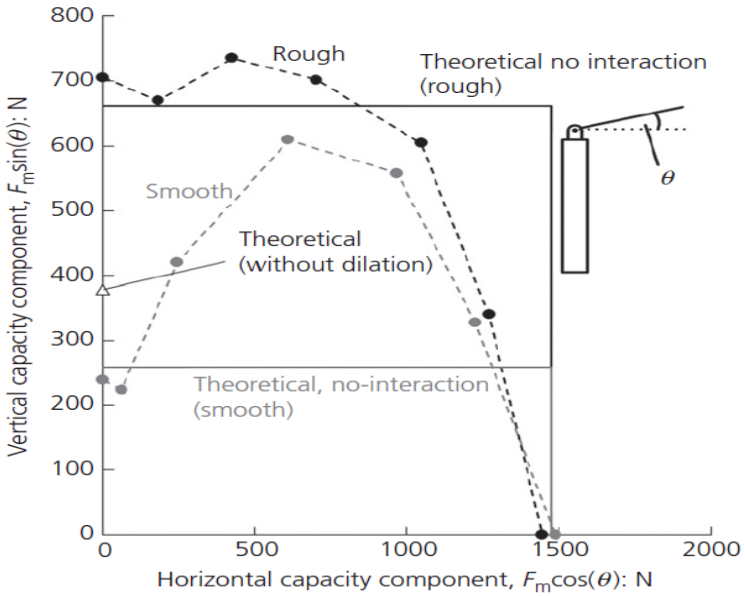

Figure 4.5: Surface roughness vs. inclination angle. Reprinted from [Huang et al., 2019]

4.2.4 Modeling contact interface

As experienced in Chapter 3 modeling the contact and interaction between the caisson anchor and soil was challenging and needed to be modeled carefully to guarantee that the solution achieved is correct and accurate. The MRA presents an extra challenge due to the fact that a top tip surface needs to be incorporated into the contact model.

The contact approaches available in ABAQUS were discussed in depth in section 3.2.4. Namely, the two main methods are General contact and Contact pair. Although the two methods use similar algorithms, they differ in the user interface and the available options. For efficiency the contact pair approach was used in the analysis where well-defined contact surfaces and properties were utilized.

Contact discretization and tracking approaches

The contact discretization is the first step after selecting contact pair approach. There are two available options for contact discretization: node to surface and surface to surface.

During the analysis the paired surfaces will interact with each other which results in a relative motion that needs to be tracked. Details about the two approaches were discussed in section 3.4.2 but a brief summary of tracking approaches is presented here. ABAQUS offers two methods to track the movement of the contact surfaces which are finite sliding technique and small sliding technique. The main difference between the two methods is that the small sliding technique defines a relationship between the slave nodes and master surface (node to master discretization) and maintain that relationship throughout the analysis whereas the finite sliding technique demands that ABAQUS constantly track which part of the master surface is in contact with each slave node. As mentioned in section 3.4.2 for the majority of contact problems this constantly tracking is unnecessary and costly in terms of computational efforts and requires very complex calculations.

Surfaces definition

To utilize the contact pair approach well-defined contact surfaces are required. In this section, the different surface definitions for the soil-MRA interface are described. The node to surface discretization was employed where MRA surfaces were defined as master surfaces while the soil surfaces in contact were defined as node-based surfaces and modeled as the slave surfaces. The diagram in Figure 4.6 shows the different surfaces where they are color coded.

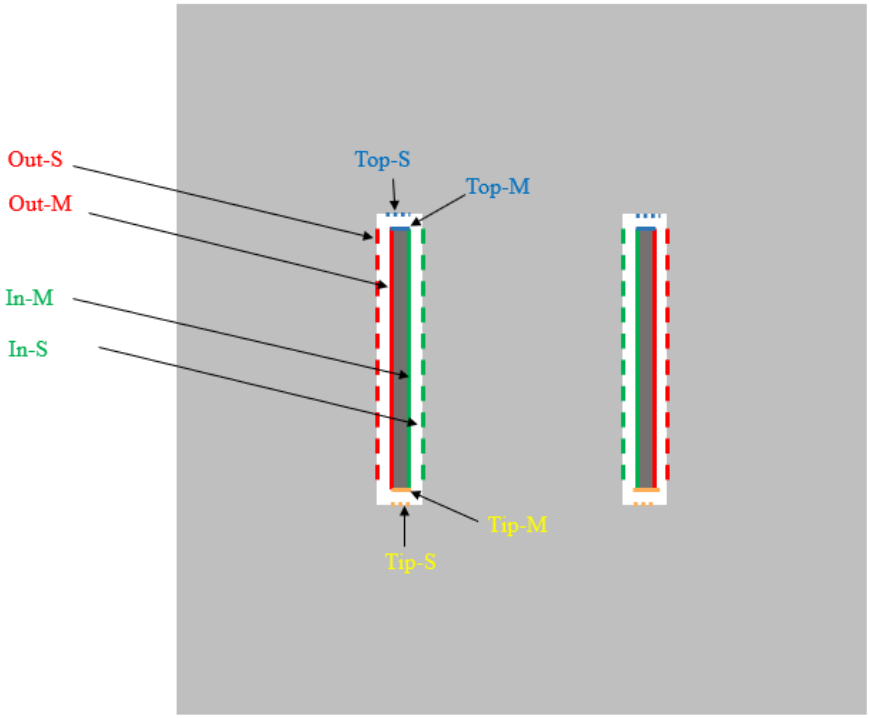

Figure 4.6: Contact surface definitions for the MRA.

Friction model

The paired surfaces in contact problems transfer loads through their interaction. These loads are normal and shear forces. As mentioned earlier the soil-MRA interface was modeled using the Coulomb friction model. The model has a main parameter called friction factor (μ) that relates the frictional shear stress to the normal pressure. ABAQUS provides an option to introduce a critical shear stress which depends on the normal contact pressure (p).

$$\tau_{critical} = \mu\, p$$

Where μ is a friction factor

p is the contact pressure between the two surfaces which represents the horizontal effective pressure σ_h.

4.2.5 Loading conditions

The primary goal of this chapter is to evaluate Multiline Ring Anchor (MRA) behavior in dense sand as an anchoring solution for offshore floating wind turbine. A three-dimensional finite element model was developed in ABAQUS to estimate the lateral capacity of MRA anchors. All loading conditions analyses were carried out under displacement control. The MRA was modeled as a rigid body with displacements applied to a reference point which was taken as the pad-eye. Figure 4.7 shows the MRA and the pad-eye location where the horizontal displacement is imposed.

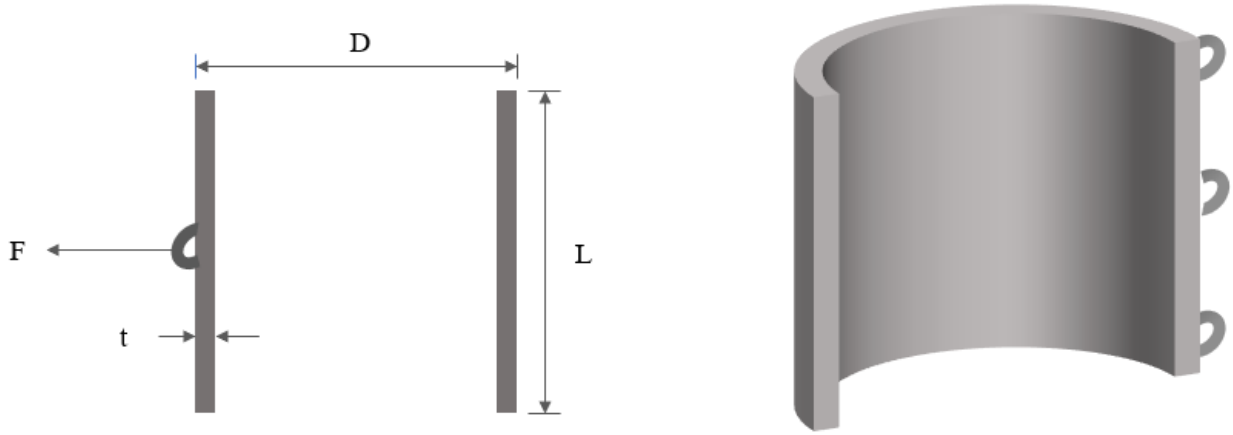

Figure 4.7: MRA under lateral loading condition.

Loading steps

The initial step is a geostatic step (*GEOSTATIC). This step is used to simulate the in-situ conditions where the initial geostatic stresses and gravity loads must be in equilibrium and generate no deformations. Horizontal and vertical stress components must be defined in the initial conditions. To properly calculate stresses in the soil domain the following parameters are required:

- $\varphi_{critical:}$ critical state friction angle

- $K_{0:}$ The coefficient of lateral earth pressure at rest which is the ratio of effective horizontal stress to effective vertical stress. Equation 4.6 can be used to estimate the coefficient value.

$$K_0 = 1 - \sin \varphi_{critical} \quad (4.6)$$

The interaction model was then activated to establish contact between soil surfaces and the surfaces of the MRA. The following loading step is to apply displacements at the pad-eye until the anchor fails. In this study a failure criterion of 10% of the anchor diameter was adopted.

4.3 Plastic limit Analysis

In this section some modifications were made to the simplified method using an upper bound formulation of plasticity limit analysis that was presented in Chapter 3 to formulate a PLA model that can estimate the lateral load capacity of MRA in sand. The plastic limit analysis model offers a quick estimate of lateral load capacity for the MRA, and it provides a way to validate the numerical model results. Additionally, the PLA model offers an alternative to assess the effect of key parameters on the lateral capacity of the MRA.

As discussed in section 3.3 the upper bound theorem uses a virtual velocity field to calculate an upper bound collapse load. The upper bound method requires postulating a kinematically admissible collapse mechanism. Figure 4.8 shows the virtual velocity field and failure mechanism. The rate of internal energy dissipation associated with the failure mechanism and the external work done by the anchor line are calculated then the collapse load is computed by optimizing the failure mechanism that corresponds to the least upper bound estimate of the collapse load. Similar to the framework that was followed in section 3.3, the ultimate lateral resistance per unit length that soils can exert against the MRA was utilized to generate an expression to compute the internal energy dissipation for MRA side resistance.

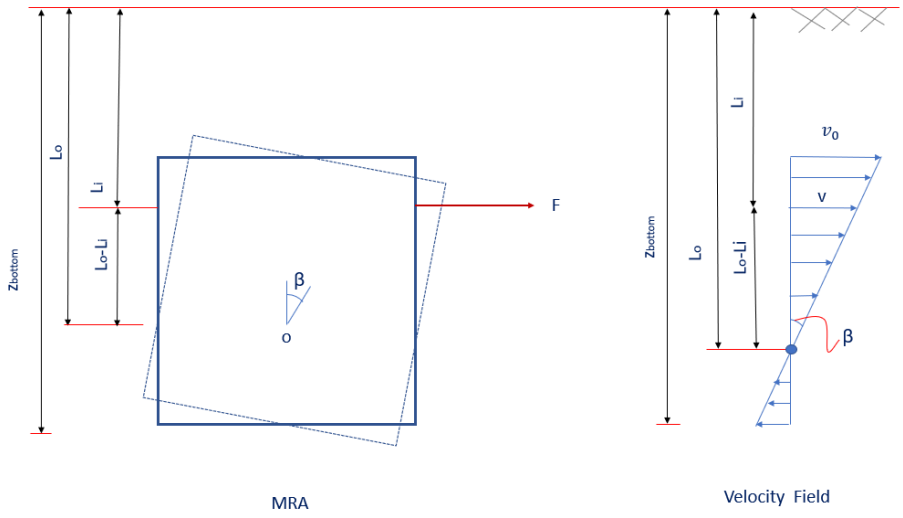

Figure 4.8: Velocity field.

4.3.1. Unit lateral soil resistance in sands

The significance of the unit lateral soil resistance (P_u) in estimating the lateral capacity of anchors in cohesionless soil was discussed in depth in sections 3.3 and 3.3.1. However, a brief summary listing the equations of the different methods that were considered in estimating the unit lateral soil resistance will be presented next.

Broms (1964)

Broms method assumes the pile will rotate around its base and it employs the passive lateral stress ratio from Rankine theory to estimate the unit lateral soil resistance (P_u).

$$P_u = 3\, K_p\, \gamma' z\, D \qquad (4.7)$$

Where: K_p is the coefficient of passive earth pressure (equation 3.8)

γ' is soil buoyant unit weight

D is MRA diameter

$$K_p = \tan^2(45 + \frac{\varphi'}{2}) \quad (4.8)$$

Petrasovtiz and Award (1972)

Petrasovtiz and Award assume a point of rotation within the pile at which the active and passive stress reversal happen. Estimating the unit lateral soil resistance (P_u) in Petrasovtiz and Award's method is given as follows:

$$P_u = 3.7(K_p - K_a)\,\gamma' z\, D \quad (4.9)$$

Where: K_p is the coefficient of passive earth pressure (equation 4.8)

K_a is the coefficient of active earth pressure (equation 4.10)

γ' is soil buoyant unit weight

D is MRA diameter

$$Ka = \tan^2(45 - \frac{\varphi'}{2}) \quad (4.10)$$

Prasad & Chari (1999)

Prasad & Chari method is the most recent approach out of the four methods considered in this study. Estimating the unit lateral soil resistance (Pu) in Prasad & Chari's method is given as follows:

$$P_u = 10^{(1.3tan\varphi + 0.3)}\gamma' z\, D \quad (4.11)$$

Reese, Cox, and Coop (1974)

The method developed by R-C-C is based on a series of tests in the field for two piles loaded horizontally in sand. Equation 4.12 is a simplified equation of Reese, Cox, and Coop method where parameters c_1, c_2, and c_3 are listed in Table 4.1 (Whiteside, 1995).

$$P_u = (c_1 + c_2 \frac{z}{D}) \gamma' z D < c_3 \gamma' z D \quad (4.12)$$

Table 4.1: Whiteside (1995) empirical fits for parameters c1, c2, and c3.

C_1	0.124 exp (0.091φ)
C_2	0.58exp (0.051φ)
C_3	0.73exp (0.123φ)

4.3.2. Internal Energy dissipation for side resistance

The rate of energy dissipation for side resistance of the MRA per unit length is the lateral soil resistance (section 4.3.1) times the virtual velocity times the projected side area. The rate of internal energy dissipation along the side of the MRA is given by equation 4.13

$$\dot{dE} = puvDdz \quad (4.13)$$

The total rate of energy dissipation is then computed by integrating equation 4.14 over the length of the MRA

$$\dot{D}_s = \int_0^L v\ pu\ D\ dz = v_0 D \int_0^L \left[\gamma'\ z_i\ (3.7K_p - K_a)\left|\left(1 - \frac{z}{Lo}\right)\right|\right]\mathrm{dz} \qquad (4.14)$$

Where: v is velocity

P_u is lateral soil resistance; Petrasovtiz and Award (1972) definition of P_u is used as an example.

D is MRA diameter

4.3.3. Internal Energy dissipation for tip resistance

MRA has two ends and they both contribute to the ultimate capacity of the anchor in sand. A kinematically admissible collapse mechanism needs to be postulated for each end. However, first an expression for the rate of internal energy dissipation for the tip resistance must be adopted.

Lower end of the MRA

To generate an expression for the rate of internal energy dissipation for the tip resistance; equation 4.15 is used.

$$\mathrm{S_d} = (\chi\, \mathrm{W_{net}}/\mathrm{A_{tip}} + \gamma' z_{\mathrm{bottom}}) \tan \phi' \qquad (4.15)$$

Where: χ is a parameter that consider the MRA weight transmitted to the soil.

z_{bottom} is the depth of the MRA measured at the MRA tip.

Upper end of the MRA

For the top of the MRA, the MRA weight does not play a role in generating the expression for the rate of internal energy dissipation. Therefore, equation 4.16 is reduced to the following expression:

$$S_d = (\gamma' z_{top}) \tan \phi' \qquad (4.16)$$

Where: z_{top} is the depth of the MRA measured at the top of the MRA.

Collapse mechanism for the tip

As mentioned earlier a kinematically admissible collapse mechanism needs to be postulated for each end. In this study, a failure mechanism that consist of a rigid rotating spherical soil mass at the bottom of the MRA failing on a compatible slip surface was adopted after Aubeny and Murff (2003). The failure mechanism is shown in Figure 4.9. From the figure, R is the MRA radius while R_1 and R_2 are variables that depend on the optimization parameter L_0.

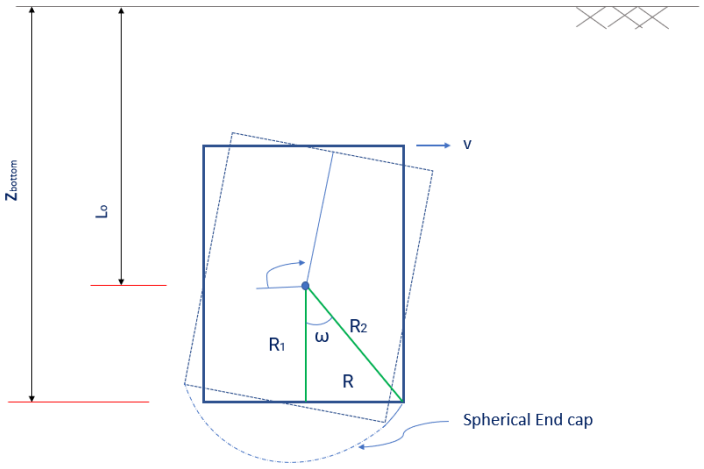

Figure 4.9: Failure mechanism at the MRA tip.

Aubeny and Murff (2003) presented a dimensionless expression for Murff and Hamilton (1993) solution:

$$\frac{M_{b0}}{0.5\pi^2 R^3 S_d} = 2\left(\frac{R1}{\pi R}\right) + \left(\frac{-I4\ R1}{R}\right) \qquad (4.17)$$

Where $R_1 = z_{bootom} - L_0$

R= D/2

I_4=1.118

Sd= $(\chi\, W_{net}/A_{tip} + \gamma' zbottom)\, tan\, \phi'$

Figure 4.10 shows the failure mechanism at the other end of the MRA (i.e., at the top of the MRA).

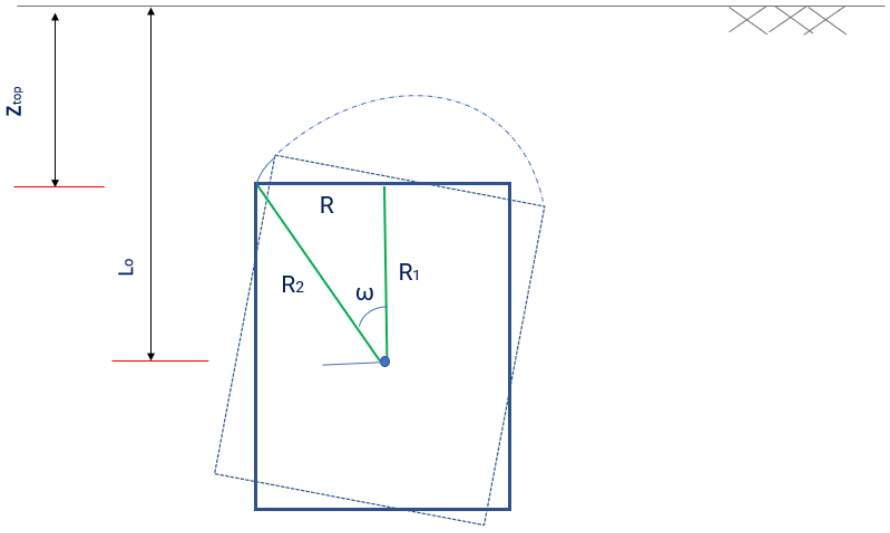

Figure 4.10: Failure mechanism at the top of the MRA.

Equation (4.18) was modified for the top of the MRA as follows:

$$\frac{M_{b0}}{0.5\pi^2 R^3 S_d} = 2\left(\frac{R1}{\pi R}\right) + \left(\frac{-I4\ R1}{R}\right) \quad (4.18)$$

Where $R_1 = L_{0-}\ z_{top}$

R= D/2

I_4=1.118

Sd= $(\gamma' ztop)\ tan\phi'$

4.3.4 External work and lateral load capacity

Equating the external work from load (*F*) to internal dissipation energies and canceling virtual velocities, we get:

$$F = \frac{D_s + D_{tip} + D_{top}}{\left|1 - {}^{L_i}/_{L_0}\right|} \quad (4.19)$$

4.3.5 PLA Model validation

The numerical model was used to validate the Plastic limit analysis (PLA) predictions. Two different embedment depths were used to compare PLA estimates for the lateral capacity of the MRA in sand to those obtained by the finite element model. All the model parameters and material properties are summarized in Table 4.2.

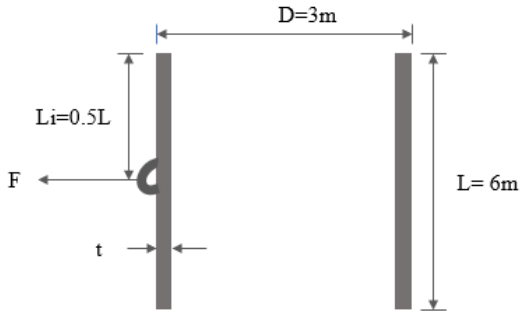

Figure 4.11: MRA model dimensions and padeye location.

Table 4.2: A summary of the parameters used in the analysis.

Part	Property	FE model	PLA model
MRA	MRA diameter (D)	3 m	3 m
	Aspect ratio	1.5	1.5
	Embedment depth (z/D)	3,5	3,5
	MRA wall thickness (t)	0.1 m	0.1 m
	Load attachment (Li/Lf)	0.5	0.5
Sand	Friction angle (ϕ')	39°	39°
	Poisson's ratio	0.3	0.3
	Buoyant unit weight	9 kN/m^3	9 kN/m^3

4.4 Comparative study between MRA and caisson anchor

The MRA presents an anchoring solution alternative and one of the main concerns is how the MRA ultimate lateral load capacity compare to other anchor capacities. In this study, the conventional caisson anchor is chosen to compare the MRA since it was the research topic of Chapter 3.

The lateral capacities of a conventional caisson anchor and a multiline ring anchor (MRA) with the same diameter were compared. The two anchors with dimensions and parameters used in the comparative study are shown in Figure 4.12. MRA and caisson anchor dimensions are summarized in Table 4.3 with soil properties that used in the analysis.

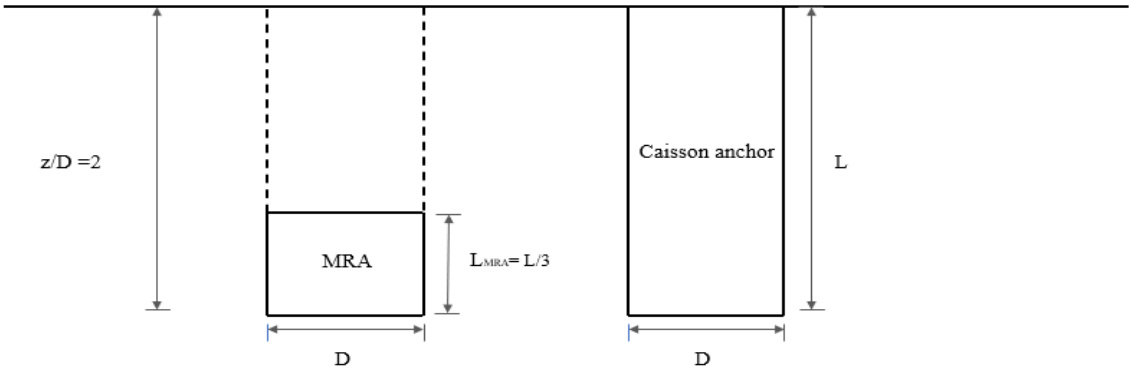

Figure 4.12: Caisson anchor and MRA.

Table 4.3: A summary of the parameters used in the analysis.

Part	Property	MRA	Caisson anchor
Anchor	Outer diameter (D)	3 m	3 m
	Length (L)	2 m	6 m
	Load attachment (L_i/L_f)	5, 25, 50, 75, 95 %	5, 25, 50, 75, 95 %
	Embedment depth (z/D)	2	-
Sand	Friction angle (ϕ')	39°	39°
	Dilation angle (Ψ)	9°	9°
	Poisson's ratio	0.3	0.3
	Buoyant unit weight	8.2 kN/m^3	8.2 kN/m^3

Figure 4.13 shows the lateral capacity of the two anchors. Load application depth close to the optimal attachment depth gives the maximum lateral capacity. For caisson anchor, from Chapter 3 the optimal attachment depth is approximately at 0.67L, shown in Figure 4.13. MRA optimal attachment depth is somewhere around middle of the anchor (0.5L). In the parametric study section, the effect of load attachment depth on ultimate capacity was investigated more.

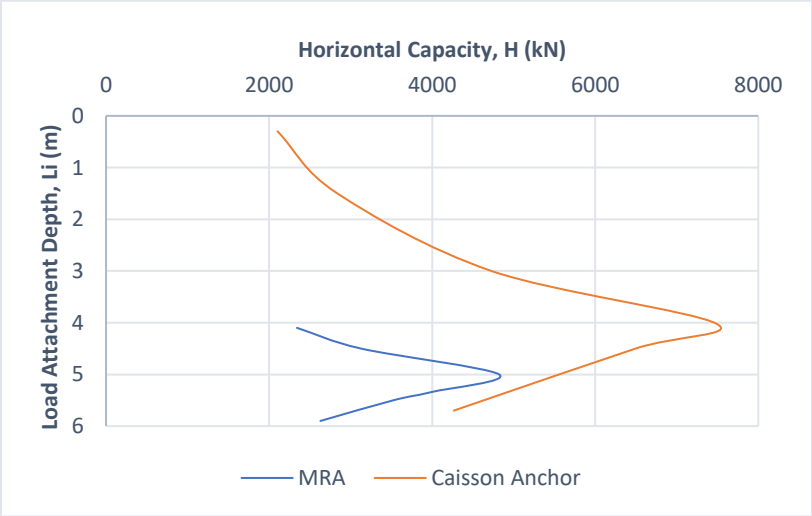

Figure 4.13: Lateral capacity for Caisson anchor and MRA.

4.5 Parametric study

After the models were validated, the models then were utilized in the scope of a parametric study to investigate the effect of key parameters on the monotonic ultimate lateral capacity of a MRA embedded in sand. The research matrix was built to evaluate the effect of load attachment depth (Li), Embedment depth (z/D), and MRA diameter (D).

The results are presented by normalizing the ultimate load capacity for ease of comparison and to follow the trends and relationships of the anchor behavior under the different load cases and model parameters. The ultimate load capacity of the MRA is divided by the vertical effective stress (σ_v) and the area that acts on which is represented by the MRA diameter (D) and the anchor length (L).

$$N_h = \frac{H}{\sigma_v D\, L} \tag{4.20}$$

Where N_h is the normlized lateral capacity of the caisson anchor.

H is the lateral load.

σ_v is the verical effective stress.

D is the MRA diameter.

L is the MRA length.

4.5.1 The effect of load attachment depth on ultimate capacity

The load attachment depth or the pad-eye location has a major effect on the ultimate capacity of the caisson anchor as it was discussed in Chapter 3. In this section, the effect of load attachment depth on MRA ultimate lateral capacity is investigated.

The load attachment depth is defined as a ratio where the load attachment depth (L_i) is divided by the total anchor length (L_f). As shown above in Figure 4.13 the expected trend of the

lateral load capacity at different load attachment depths. The lateral load capacity increases when the padeye location moves from the top of the MRA towards the bottom of the anchor until it reaches its maximum capacity at a certain point after that the lateral capacity starts to decrease. The maximum lateral ultimate capacity occurs at the optimum load attachment depth. One characteristic of the optimum padeye location is that there is no rotation and loading is purely translational. The optimum load attachment depth for MRA is located around Li/Lf= 0.5. To further investigate the effect of load attachment depth, MRA diameter of 3 m and a length of 2D was used and to define the optimum padeye location. A schematic of the model dimensions and load attachment depths are shown in Figure 4.14 Model parameters and material properties that were used in the analysis are summarized in Table 4.4.

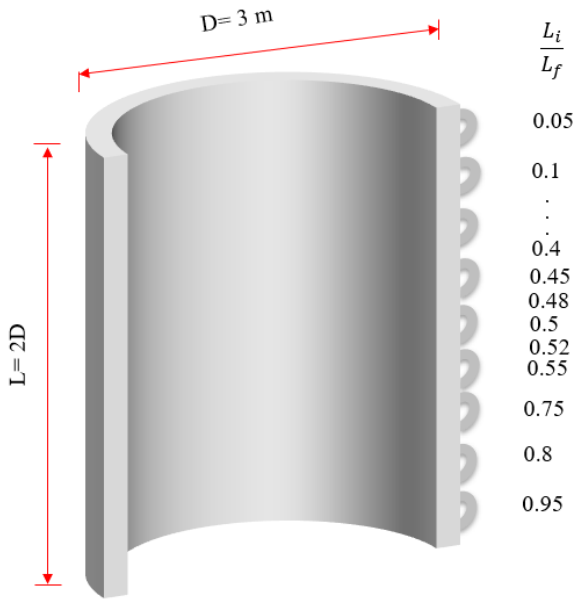

Figure 4.14: Model dimensions and load attachment depths.

Table 4.4.: A summary of the parameters used in the analysis.

Part	Property	
MRA	Outer diameter (D)	3 m
	Length (L)	2D
	Load attachment (Li/Lf)	5, 10, 20,30,40,45,48,50,52,55,60, 75, 80, 95 %
	Embedment depth (z/D)	5
Sand	Friction angle (ϕ')	39°
	Dilation angle (Ψ)	9°
	Relative density, Dr (%)	70
	Poisson's ratio	0.3
	Critical state Friction angle	31°
	Cohesion (c)	1 kN/m^2
	Buoyant unit weight	8.2 kN/m^3

The reults are shown in Figure 4.15. The maximum ultimate lateral load capcity corresponds to Li/Lf of 0.55 which represents the optimum load attahcment depth (L_{opt}). The effect of the padeye location will be further assessed in the next sections.

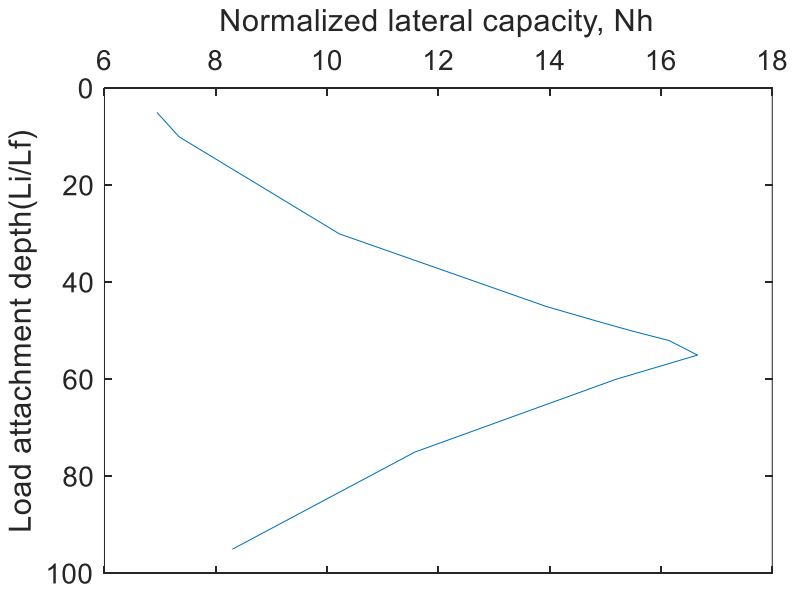

Figure 4.15: Ultimate lateral capacity at different load attachment depths.

4.5.2 The effect of embedment depth on ultimate capacity

One of the main advantages of the Multiline Ring Anchor (MRA) is that it can be installed deeper to increase the ultimate capacity. In this section, the effect of the embedment depth on the ultimate lateral capacity of the MRA was examined. The embedment depth (z/D) is a parameter that is used to describe how deep the MRA is in the ground where z represents depth and D is the MRA diameter.

To investigate the effect of the embedment depth on the ultimate lateral capacity of the MRA, an MRA with a diameter of 4 m and length of 6 meter was used. Three different levels of embedment depths were considered 3,5, and 7. 1 Model parameters and material properties that were used in the analysis are summarized in Table 4.5.

Table 4.5.: A summary of the parameters used in the analysis.

Part	Property	
MRA	Outer diameter (D)	4 m
	Length (L)	1.5D
	Load attachment (Li/Lf)	50 %
	Embedment depth (z/D)	3,5,7
Sand	Friction angle (ϕ')	39°
	Dilation angle (Ψ)	9°
	Relative density, Dr (%)	70
	Poisson's ratio	0.3
	Critical state Friction angle	31°
	Cohesion (c)	1 kN/m^2
	Buoyant unit weight	8.2 kN/m^3

Figure 4.16 shows the results for the MRA ultimate capacity at the different embedment depths. It can be noticed from the figure for all the different methods, the MRA capacity increases as the embedment depth increase. Figure 4.16 shows the finite element model prediction for the case of z/D=5 is less than the PLA predictions using Petrasovitz and Award or Prasad and Chari. Broms (1964) yields the most conservative estimates compared to other methods.

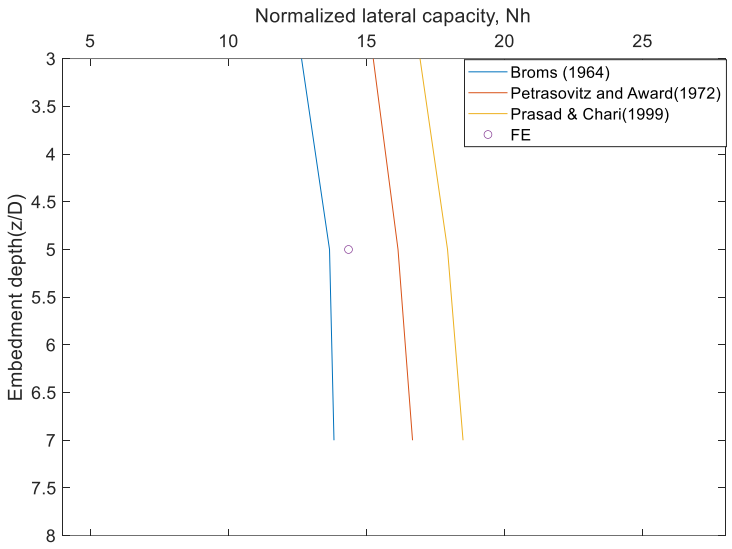

Figure 4.16: MRA ultimate lateral capacity vs. embedment depth.

4.5.3 The effect of MRA diameter on ultimate capacity

Increasing the anchor diameter is another method of improving the MRA ultimate capacity in sand. To investigate the effect of the anchor diameter on the ultimate lateral capacity of the MRA, three different MRA diameters were considered 2.8m ,4m, and 5m. Model parameters and material properties that were used in the analysis are summarized in Table 4.6.

Table 4.6: A summary of the parameters used in the analysis.

Part	Property	
MRA	Outer diameter (D)	2.8,4,5 m
	Length (L)	4 m
	Load attachment (Li/Lf)	50 %
	Embedment depth (z/D)	5
Sand	Friction angle (ϕ')	39°
	Dilation angle (Ψ)	9°
	Relative density, Dr (%)	70
	Poisson's ratio	0.3
	Critical state Friction angle	31°
	Cohesion (c)	1 kN/m^2
	Buoyant unit weight	8.2 kN/m^3

Figure 4.17 shows the results for the MRA ultimate capacity with different anchor diameters. It can be noticed from the figure for all the different methods, the MRA capacity increases as the anchor diameter increase. Figure 4.17 shows that Prasad and Chari method overestimates the ultimate capacity of the MRA while Petrasovitz and Award gives a prediction that is in the middle between it and the conservative prediction from Broms (1964) method.

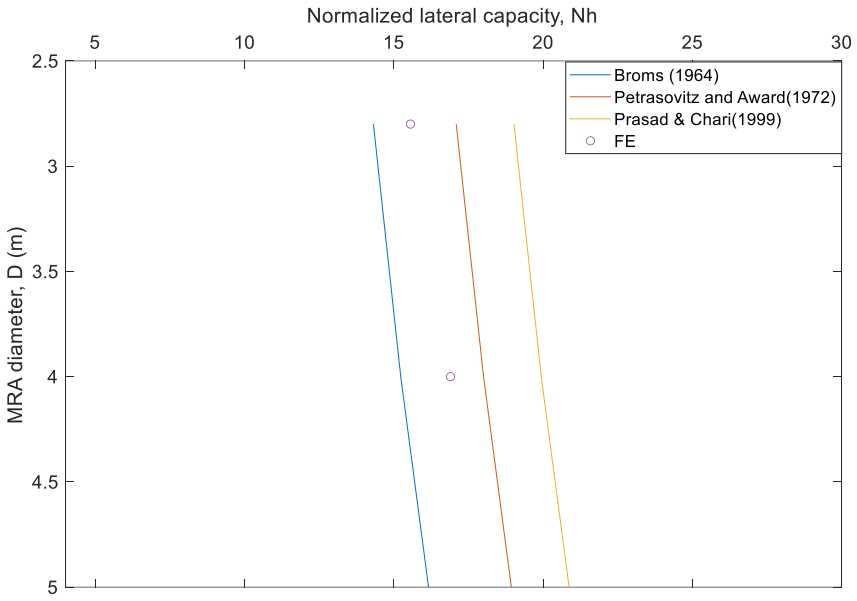

Figure 4.17: MRA ultimate lateral capacity vs. anchor diameter.

CHAPTER V

BUCKET FOUNDATION FOR FIXED FOUNDATION OFFSHORE WIND TOWERS

5.1 Introduction

The caisson anchor and Multiline Ring Anchor (MRA) were studied in Chapter 3 and Chapter 4 to investigate the two anchors behavior in sand and evaluate them as anchoring solutions for offshore floating wind turbines. This chapter investigates a fixed-bottom foundation system where the wind turbine is supported by a massive bucket foundation, Figure 5.1. The majority of the existing offshore wind turbine projects utilize a fixed-bottom system where they are built in water depths less than 60 meters. The fixed-bottom technology is more mature than the floating offshore wind technology as discussed in Chapter 2. In 2018, the typical turbine size was 6.8 Megawatt while in 2021 GE introduced the 12-Megawatt Haliade-X offshore wind turbine to market (Gaertner *et al.*, 2020). Offshore wind turbine size will continue to increase because larger turbines yield more energy at a lower rate. The main objective of this chapter is to size a bucket foundation that is under high moment demands for a fixed 15-Megawatt wind turbine.

Figure 5.1: An offshore wind turbine with a monopod bucket foundation. Reprinted from [Achmus et al. ,2013]

5.2 Problem Statement

The primary goal of this chapter is to size a bucket foundation for a fixed-bottom wind turbine structure that supports the International Energy Agency (IEA) 15-megawatt offshore wind turbine. The IEA 15-megawatt offshore wind turbine is shown in Figure 5.2. The turbine has a rotor with a diameter of 240 m and a hub height of 150 m as shown in the Figure. The overall parameters for the IEA 15-megawatt offshore wind turbine including blade, rotor, tower, and nacelle properties are summarized in Table 5.1.

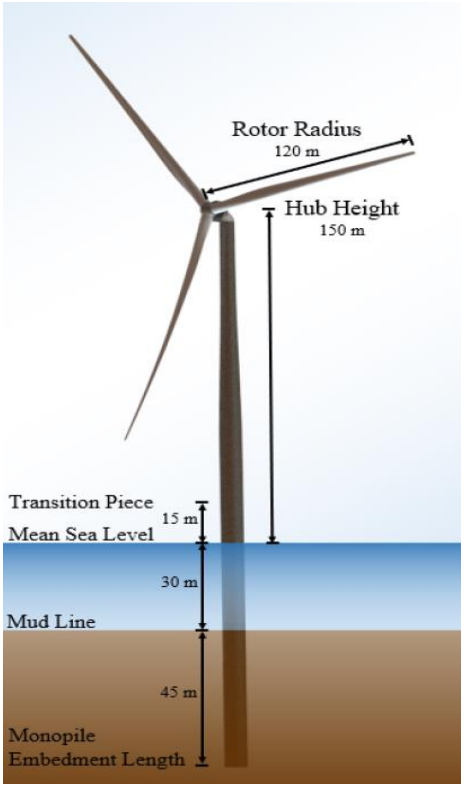

Figure 5.2: The IEA wind 15 MW reference wind turbine. Reprinted from [Gaertner et al., 2020]

Table 5.1: Key parameters for the IEA 15MW turbine. Reprinted from [Gaertner et al., 2020]

Parameter	Value	Units
Power rating	15	MW
Turbine class	IEC Class 1B	-
Specific rating	332	W/m^2
Number of blades	3	-
Minimum rotor speed	5	rpm
Maximum rotor speed	7.56	rpm
Rotor diameter	240	m
Hub height	150	m
Hub diameter	7.94	m
Hub overhang	11.35	m
Blade prebend	4	m
Blade mass	65	t
RNA mass	1017	t
Transition piece height	15	m

With a hub height of 150 m, the bucket foundation will be under a high moment demand. The loading conditions will be discussed more in a later section. Gaertner *et al*. (2020) assumed a generic U.S. east coast site with a wind speed described by a Weibull distribution with a mean velocity of around 8.65 m/s where the corresponding wave height is about 1.4 m. To define the worst-case ultimate loading on the system parts, Gaertner *et al*. (2020) performed a design load case analysis using OpenFAST. Table 5.2 shows the different design load cases considered in the analysis.

Table 5.2: Summary of design load case settings. Reprinted from [Gaertner et al., 2020]

DLC	Wind Condition	Wind speeds	No. of Simulations
1.1	NTM	3:2:25 m/s	72
1.3	ETM	3:2:25 m/s	72
1.4	ECD	Vr m/s	6
1.5	EWS	3:2:25 m/s	48
6.1	EWM	V50	12
6.3	EWM	V1	12
NTM	normal turbulence model		
ETM	extreme turbulence model		
ECD	extreme coherent gust with direction change		
EWS	extreme wind shear		
EWM	extreme wind speed model		
Vr=10.8 m/s	rated wind speed		
V50=50m/s	10-m average extreme speed with a 50-year return period		
V1=40m/s	10-m average extreme speed with a 1-year return period		

Figure 5.3 shows the maximum bending moment for the different cases. From the figure, the maximum bending moment at the tower base is around 410 MN-m for the extreme wind speed cases.

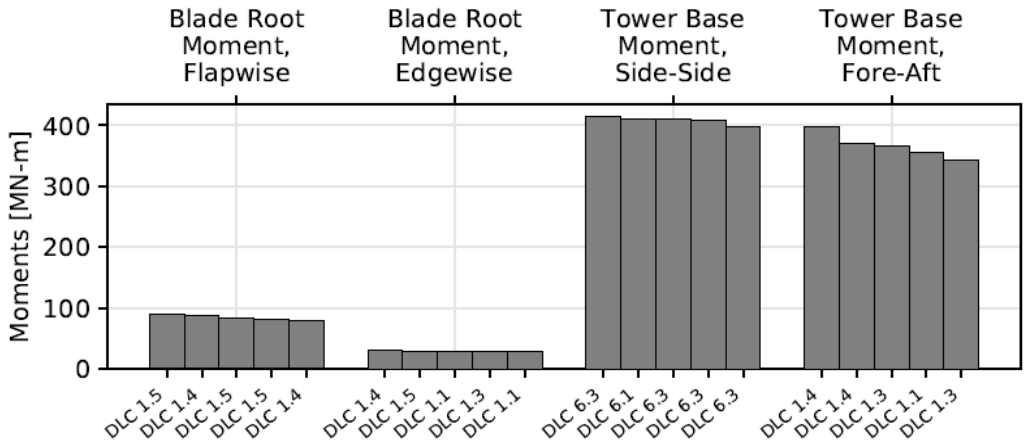

Figure 5.3: DLC ranking of maximum blade root and tower base bending moments. Reprinted from [Gaertner et al., 2020]

5.3 Numerical Model

A three-dimensional finite element model was developed in ABAQUS to estimate the capacity of the bucket foundation in sand under high moment demand. In this section, details regarding the development of the finite element model and its validation are discussed.

5.3.1 Model Geometry and boundary conditions

The numerical model mesh, geometry, and boundary conditions are described in this section. Figure 5.4 shows the mesh of the finite element model used to model the bucket foundation. The mesh is generated by a MATLAB code to be able to modify and adopt different cases of loading conditions or material properties. The code is divided into four parts: mesh generator, material model, interaction model, and loading model. The mesh generator has added capabilities of refining certain regions of the model and controlling the element size and numbers for every part. Region refinement helps in building a refined mesh for a particular part in the domain that is of interest and a coarser mesh for rest of the domain. The soil elements around the bucket both inside and outside are part of a refined meth. Sensitivity analyses were completed to determine the refinement level and domain size, they are discussed later in this section.

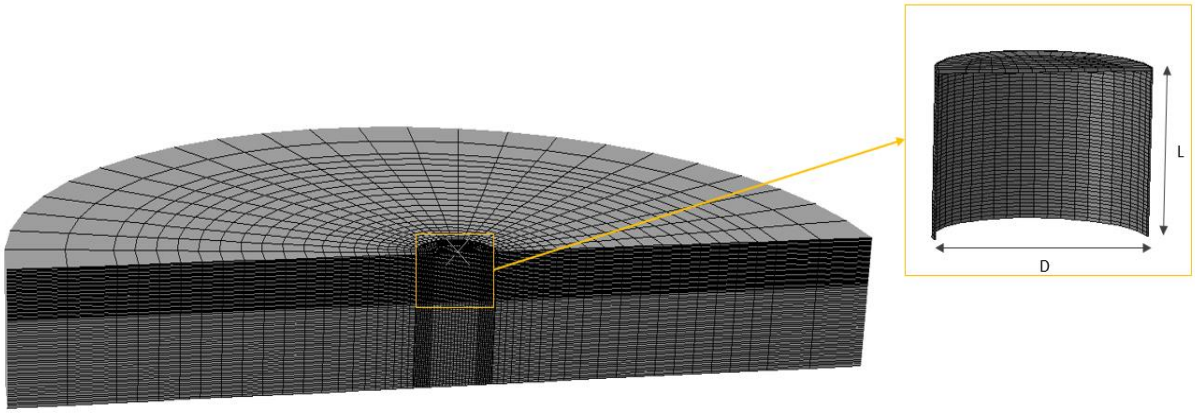

Figure 5.4: Finite- element mesh.

The soil domain was meshed using the solid continuum element C3D8 (8-node linear brick) which is a three dimensional fully integrated element i.e., it has eight integration points. ABAQUS manual offers some guidance on element selection and for a structure under bending it advises not to use C3D8 elements because results show that C3D8 can be stiff. Thus, the bucket foundation was meshed using an improved version of C3D8 which is C3D8I element. The incompatible mode eight-node brick element removes shear locking and reduces volumetric locking. ABAQUS enhances the shape functions used in C3D8 by using bubble functions that have a zero value at all nodes and non-zero values between the nodes (Simo and Armero, 1992).

Boundary conditions imposed on the model consists of two main boundary conditions (BCs). First, displacements are constrained on the far-field nodes for both of the horizontal directions (u_x, u_y). To impose the far-field boundary conditions, the infinite element CIN3D8 is used for the far-field elements. Such elements are available in ABAQUS element library to model problems in which the region of interest is small in size compared to the surrounding medium.

Second, displacements are restricted in all directions (u_x,u_y,u_z) for the bottom nodes of the model. Degrees of freedom 1,2, and 3 are restricted for all nodes at the bottom of the domain.

5.3.2 Material Modeling

The constitutive model Mohr-Coulomb was used to model the soil domain. Mohr-Coulomb is an elastic-perfectly plastic model used to represent shear failure in soils. The model is one of built-in models that are available in ABAQUS library. In the background chapter Mohr-Coulomb model was discussed and few features of the model were highlighted. Details on Mohr-Coulomb model implementation in ABAQUS were covered in Section 3.2.2.

5.3.3 Material properties and model parameters

As mentioned above, the soil was modeled as an isotropic elastic-perfectly plastic material using Mohr-Coulomb model available in ABAQUS library. In this section, the model parameters are discussed and the parameters selection to help correctly model the nonlinear soil response. To model the sand in ABAQUS, the linear isotropic elasticity model was used with Mohr-Coulomb model to represent the elastic regime. For the elasticity model, two parameters are required modulus of elasticity (E) and Poisson's ratio (ν). For Mohr-Coulomb model, friction angle (φ), dilation angle (ψ), and cohesion (c) are the required parameters. The soil considered in this study is cohesionless but to ensure numerical convergence a low nominal cohesion value is assigned.

Modulus of elasticity (E)

As mentioned in section 3.2.3, A stress-dependent modulus of elasticity (E) must be considered to realistically model the nonlinearity in the soil response. Section 3.2.3 discussed few methods available in the literature to estimate the value of Young' modulus based on stress level. The stress dependent oedometric modulus of elasticity approach proposed by Janbu (1964) was used in this chapter.

Equation suggested by Janbu (1964)

$$E_s = k\ pa\ \left(\frac{\sigma_m}{pa}\right)^n \qquad (5.1)$$

Where k is a parameter that defines the soil stiffness at the reference stress state.

pa is the reference stress and it equals 100 kN/m^2.

σ_m is the mean principal stress.

n is a parameter that governs the stress dependency of the soil stiffness.

Poisson's ratio (ν)

In elastic material deformations, Poisson's ratio defines the ratio deformation perpendicular to the direction of normal loading. Generally, for a homogeneous and isotropic soil, the Poisson's ratio varies in the range $0 \leq \nu \leq 0.5$. For the medium to dense sand soil considered in this study a Poisson's ratio (ν) equals 0.25 is used.

Mohr-Coulomb Plastic Parameters

Mohr-Coulomb model has three plastic parameters which are friction angle (φ), dilation angle (ψ), and nominal cohesion (c). Sand is cohesionless soil (c=0); however, for the numerical model to avoid convergence issues a low nominal cohesion value is required. In this study a small cohesion of 1 kPa was used.

The friction angle (φ) and dilation angle (ψ) are both a function of soil density and stress level. Thus, a soil profile was created where friction angle (φ) and dilation angle (ψ) are generated using Bolton equations to incorporate the effect of soil density and stress level. Bolton equations were discussed in detail in Chapter 2 and section 3.2.3 but for clarity the main points are reiterated here.

Bolton (1986) found that equation 5.2 can be used to estimate the peak friction angle for both plane-strain and triaxial compression conditions.

$$\varphi_{peak} = \varphi_{critical} + A\psi\, I_R \qquad (5.2)$$

Where $\varphi_{critical}$ is the critical state friction angle

$A\psi = 3$ for triaxial condition and 5 for plane strain condition.

I_R is a relative dilatancy index estimated from equation (5.3)

$$I_R = D_r\,(10 - \ln p) - 1 \qquad (5.3)$$

After calculating the peak friction angle, the peak dilation angle can be estimated using the following equation:

$$\varphi_{peak} - \varphi_{critical} = 0.8\ \psi_{peak} \qquad (5.4)$$

Soil-foundation interface friction angle (δ)

The Coulomb friction model was used to model the bucket-soil interface. The contact model itself is discussed in the next section. As mentioned in section 3.2.3, the contact model utilizes a friction factor (μ) parameter which value depends on the soil- bucket foundation interface friction angle (δ). Studies conducted by Han *et al*. (2018) and Huang *et al*. (2019) show the effect of different factors such as surface roughness, size and shape of soil particles, soil gradation, and load inclination angle on the ultimate capacity of the foundation. In Figure 5.5, the surface roughness effect, i.e., the soil- bucket foundation interface friction angle (δ), is evident for load

inclination angles greater than 45° (Huang *et al*., 2019). In this chapter, since the bucket foundation is mainly under moment demand, the effect of surface roughness will be assessed.

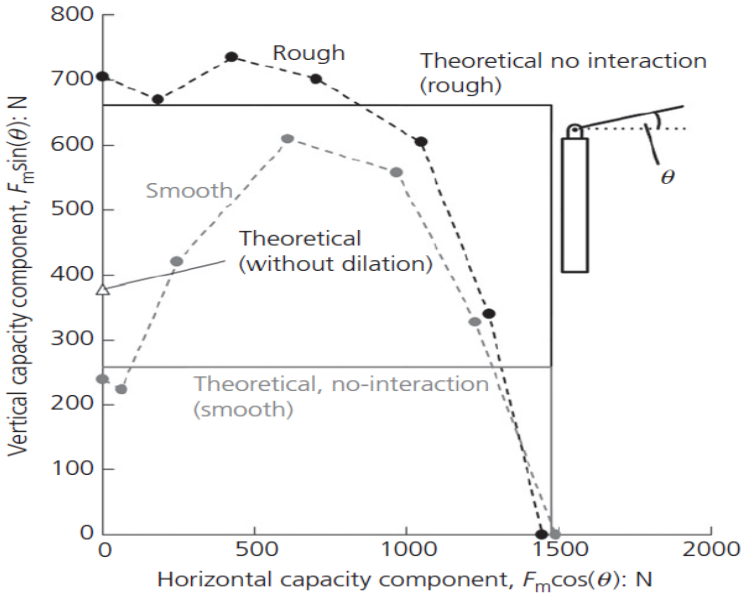

Figure 5.5: Surface roughness vs. inclination angle. Reprinted from [Huang et al., 2019]

The paired surfaces in contact problems transfer loads through their interaction. These loads are normal and shear forces. As mentioned earlier the soil-bucket interface was modeled using the Coulomb friction model. The model has a main parameter called friction factor (μ) that relates the frictional shear stress to the normal pressure. ABAQUS provides an option to introduce a critical shear stress which depends on the normal contact pressure (p).

$$\tau_{critical} = \mu\, p$$

Where μ is a friction factor.

5.3.4 Modeling contact interface

As experienced in Chapter 3 modeling the contact and interaction between the caisson anchor and soil was challenging and needed to be modeled carefully to guarantee that the solution achieved is correct and accurate.

The contact approaches available in ABAQUS were discussed in depth in section 3.2.4. Namely, the two main methods are General contact and Contact pair. Although the two methods use similar algorithms, they differ in the user interface and the available options. For efficiency the contact pair approach was used in the analysis where well-defined contact surfaces and properties were utilized.

Contact discretization and tracking approaches

The contact discretization is the first step after selecting contact pair approach. There are two available options for contact discretization: node to surface and surface to surface.

During the analysis the paired surfaces will interact with each other which results in a relative motion that needs to be tracked. Details about the two approaches were discussed in section 3.4.2 but a brief summary of tracking approaches is presented here. ABAQUS offers two methods to track the movement of the contact surfaces which are finite sliding technique and small sliding technique. The main difference between the two methods is that the small sliding technique defines a relationship between the slave nodes and master surface (node to master discretization) and maintain that relationship throughout the analysis whereas the finite sliding technique demands that ABAQUS constantly track which part of the master surface is in contact with each slave node. As mentioned in section 3.4.2 for the majority of contact problems this constantly tracking is unnecessary and costly in terms of computational efforts and requires very complex calculations.

Surfaces definition

To utilize the contact pair approach well-defined contact surfaces are required. In this section, the different surface definitions for the soil-foundation interface are described. The node to surface discretization was employed where bucket surfaces were defined as master surfaces while the soil surfaces in contact were defined as node-based surfaces and modeled as the slave surfaces.

5.3.5 Loading conditions

The primary goal of this chapter is to size a bucket foundation that is under high moment demand for a fixed 15-Megawatt wind turbine. A three-dimensional finite element model was developed in ABAQUS to estimate the ultimate capacity of the bucket foundation. All loading conditions analyses were carried out under displacement control. The bucket was modeled as a rigid body with displacements applied to a reference point. The reference point at which the lateral displacement applied is a 180 m above the bucket foundation which represents the hub height of 150 m and a water depth of 30 m, as shown in Figure 5.6.

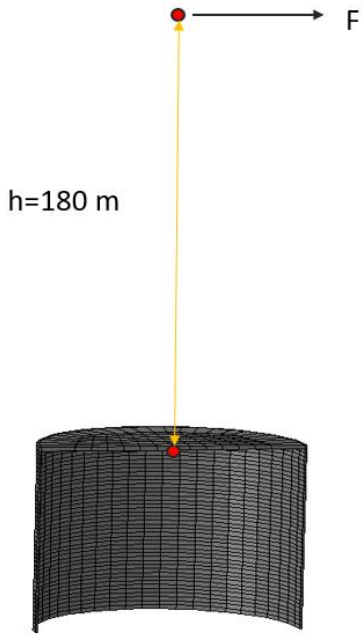

Figure 5.6: Reference point where lateral load is applied.

Loading steps

The initial step is a geostatic step (*GEOSTATIC). This step is used to simulate the in-situ conditions where the initial geostatic stresses and gravity loads must be in equilibrium and generate no deformations. Horizontal and vertical stress components must be defined in the initial conditions. To properly calculate stresses in the soil domain the following parameters are required:

- $\varphi_{critical:}$ critical state friction angle
- $K_{0:}$ The coefficient of lateral earth pressure at rest which is the ratio of effective horizontal stress to effective vertical stress. Equation 5.5 can be used to estimate the coefficient value.

$$K_0 = 1 - \sin \varphi_{critical} \qquad (5.5)$$

The interaction model was then activated to establish contact between soil surfaces and the surfaces of the bucket. To simulate the superstructure weight on the bucket foundation, a vertical

load on the bucket foundation cap in the second loading step. Estimating the superstructure weight for the IEA 15 MW wind turbine is discussed in a later section. The final step in the analysis is to apply lateral displacements at the reference point until the bucket fails.

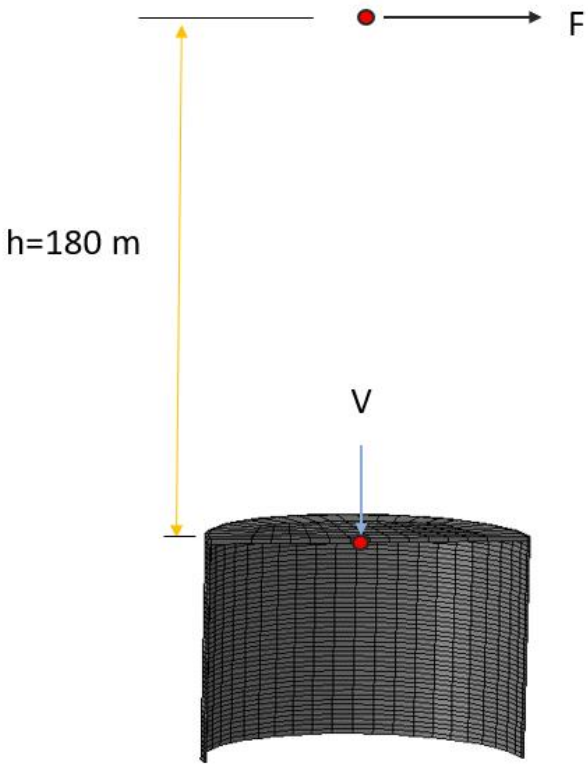

Figure 5.7: Superstructure weight and the reference point for lateral displacements.

5.3.6 Failure criterion

In Chapter 3 and 4, the caisson anchor and MRA failures were governed by the ultimate limit state where a failure criterion of 10% of the anchor diameter was adopted. However, for the bucket foundation a different criterion is implemented to meet an allowable limit load. A rotation of 0.5° at the bucket level was adopted as a failure criterion.

5.3.7 Numerical Model Validation

The finite element model was validated using field test data and other numerical model studies before the model was used to size the bucket foundation for a fixed 15-Megawatt wind turbine.

Houlsby *et al.* (2005) showed the datils and analyses of large-scale tests that took place in Frederikshavn. A bucket foundation with a diameter of 2 m and aspect ratio of 1 was installed in a very dense sand soil at a shallow water depth of 4 m. The bucket foundation was supporting a 3 MW wind turbine, as shown in Figure 5.8. The bucket used for the large-scale test in Frederikshavn is shown in Figure 5.9.

Figure 5.8: Vestas V90 3MW turbine. Reprinted from [Houlsby et al., 2005]

Figure 5.9: The 2 m diameter bucket used for large-scale test in Frederikshavn. Reprinted from [Houlsby et al., 2005]

All the parameters and material properties that are reported by Houlsby *et al.* (2005) for the large-scale tests in Frederikshavn are summarized in Table 5.3 For the numerical model parameters, a negligible nominal cohesion of 1 kN/m^2 was used in the model to ensure numerical convergence. Another material property that was assumed in the numerical model is a critical state friction angle of 31° for the sand sample. The critical state friction angle was used in the initial stress calculations for the geostatic step.

Table 5.3: A summary of the parameters used in the analysis.

Part	Property	Centrifuge tests	Numerical model
Bucket	Outer diameter (D)	2 m	2 m
	Length (L)	2 m	2 m
	Loading eccentricity (h)	17.4 m	17.4 m
	Vertical load (V)	37.3 kN	37.3 kN
Sand	Friction angle (ϕ')	-	37°
	Dilation angle (Ψ)		7°
	Relative density, Dr (%)	90	90
	Poisson's ratio	0.25	0.25
	Critical state Friction angle (ϕ')	-	31°
	Cohesion (c)	-	1 kN/m^2
	Buoyant unit weight	9 kN/m^3	9 kN/m^3
	Elastic stiffness parameter *k*		500
	Elastic stiffness exponent *n*		0.58

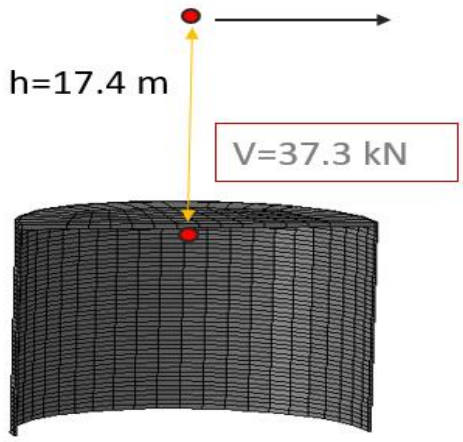

Figure 5.10: Loading eccentricity and vertical load used in the numerical analysis.

Figure 5.11 shows the finite element model predictions compared to the large-scale test data in Frederikshavn from Houlsby *et al.* (2005). Although, the numerical model prediction slightly underestimates the ultimate capacity of the bucket foundation compared to the measured data, the model estimates are still in a good agreement with the data from Frederikshavn. The difference in the ultimate capacity between the model perdition and the measured data can be attributed to the material property estimation for the dense sand.

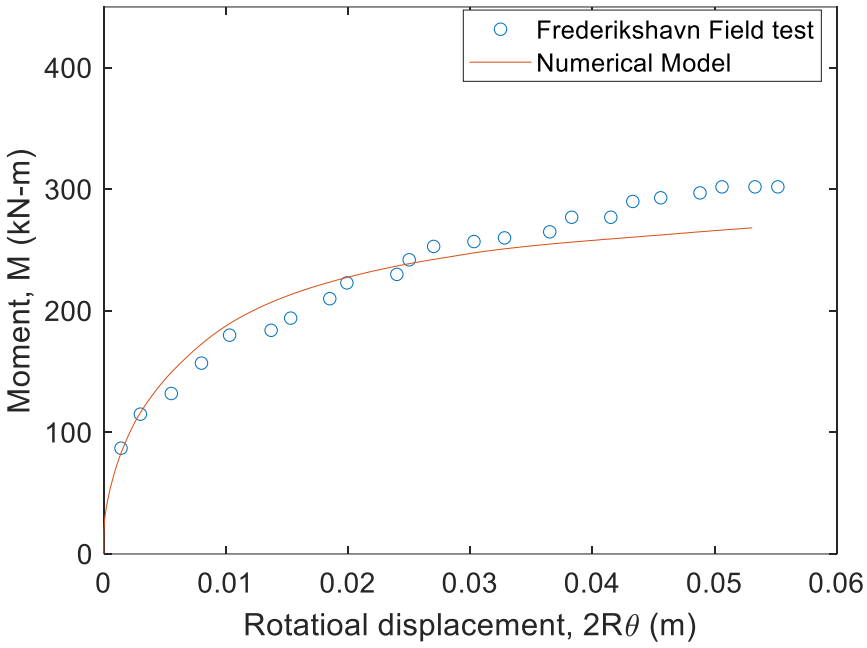

Figure 5.11: Finite element and field test results.

5.4 Bucket foundation for IEA 15 MW wind turbine

The technical report "Definition of the IEA 15-Megawatt Offshore Reference Wind" published by National Renewable Energy Laboratory (NREL) was used obtain technical information about the IEA 15-Megawatt turbine including the hub height, tower mass, rotor nacelle assembly mass (RNA), and design load case analyses. In section 5.2, Figure 5.3 shows the maximum bending moment for the different cases. From the figure, the maximum bending moment at the tower base is around 410 MN-m for the extreme wind speed case. Table 5.4 summaries the IEA 15-Megawatt turbine parameters used in the analysis.

Table 5.4: IEA 15-Megawatt turbine parameters.

Parameter	Value	Units
Rotor diameter	240	meters
Hub height	150	meters
Water depth	30	meters
RNA mass	1017	metric tons
Tower mass	860	metric tons

From the hub height and water depth, the load eccentricity (h) can be calculated as follows:

$$\text{load eccentricity (h)} = \text{Hub height} + \text{Water depth} = 180 \text{ m}$$

The maximum horizontal load that the bucket needs to withstand is 2.3 MN acting at a load eccentricity of 180 m above the bucket foundation cap.

5.4.1 Superstructure weight

To estimate the superstructure weight of the IEA 15-Megawatt turbine, tower mass and RNA mass from Table 5.4.1 were used. The superstructure mass is 2072 metric tons which corresponds to a weight of 20 MN. Thus, a vertical load of 20 MN was applied at the bucket foundation cap. The soil properties of the dense sand soil that was used in the numerical model analysis are summarized in Table 5.5.

Table 5.5: A summary of the parameters used in the analysis.

Part	Property	Numerical model
Sand	Friction angle (ϕ')	40°
	Dilation angle (Ψ)	10°
	Relative density, Dr (%)	90
	Poisson's ratio	0.25
	Critical state Friction angle (ϕ')	30°
	Cohesion (c)	1 kN/m^2
	Buoyant unit weight	11 kN/m^3
	Elastic stiffness parameter *k*	600
	Elastic stiffness exponent *n*	0.65

5.4.2 Deb and Singh (2018) – 3 Parameters

Deb and Singh (2018) proposed two equations to estimate the ultimate and allowable load capacities of bucket foundation developed by curve fitting where their analysis was based on Achmus et al. (2013). One set of equations has three fitting parameters a, b, and c while the other set has only two parameters.

The ultimate load capacity can be estimated using the following equation:

$$H_{ultimate} = \frac{\gamma' L D^2}{a+b\left(\frac{h}{L}\right)+c\left(\frac{h}{L}\right)^2} \quad (5.6)$$

Where: ɣ ′is Buoyant unit weight

L is the bucket length

D is the bucket diameter

h is load eccentricity

a,b, and c are fitting parameters (see Table 5.6)

The allowable load capacity which is defined at a bucket rotation of θ=0.5°
can be estimated using the following equation:

$$H_{Allowable} = a'(\gamma' L D^2) + b'(H_{ultimate}) + c' \frac{(H_{ultimate})^2}{\gamma' L D^2} \quad (5.7)$$

Table 5.6: Fitting parameters for the three parameter equations

a	0.4019	a'	0.0232
b	0.3733	b'	0.3509
c	3.71E-05	c'	0.085

5.4.3 Deb and Singh (2018) – 2 Parameters

The ultimate load capacity can be estimated using the following equation:

$$H_{ultimate} = \frac{\gamma' D L^2}{a+b\left(\frac{h}{L}\right)+c\left(\frac{h}{L}\right)^2} \quad (5.8)$$

Where: ɣ ′is Buoyant unit weight

L is the bucket length

D is the bucket diameter

h is load eccentricity

a,b, and c are fitting parameters (see Table 5.7)

The allowable load capacity which is defined at a bucket rotation of θ=0.5° can be estimated using the following equation:

$$H_{Allowable} = a'(H_{ultimate}) + b' \frac{(H_{ultimate})^2}{\gamma' D L^2} \quad (5.9)$$

Table 5.7: Fitting parameters for the two parameter equations

a	0.288	a'	0.191
b	0.367	b'	0.083
c	-0.007	c'	-

5.4.4 Bucket Foundation Results

Deb and Singh equations were used as a starting point to obtain an initial bucket size to initiate the finite element model study. It was found that using the soil properties from Table 5.4.2, a bucket foundation with a diameter of 16 m and aspect ratio of 1 has an allowable load capacity of 2.74 MN in the 2-parameter method and 4.7 MN using the 3-parameter equation. A finite element analysis was performed using the same dimensions as shown in Figure 5.12. The finite element estimate of the allowable load capacity of the bucket foundation is 3.1 MN.

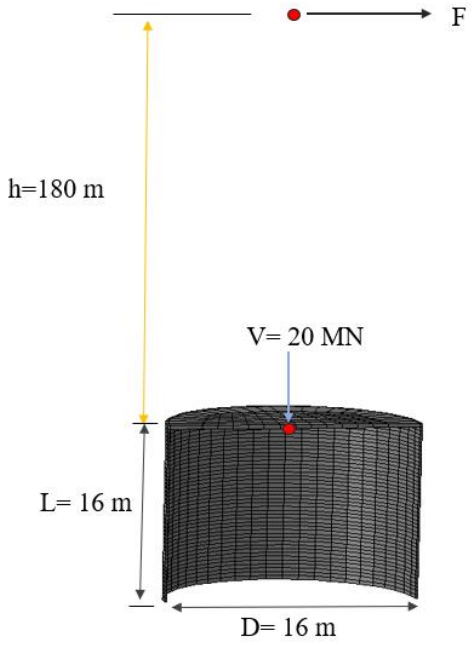

Figure 5.12: Loading parameters and bucket dimensions used in the numerical model.

Other aspect ratios were considered in sizing the bucket foundation including L/D of 0.8 to allow for suction installation. Table 5.8 has the different aspect ratios and diameter and length combinations.

Table 5.8: Bucket sizes considered in the analysis.

L/D=1	D	16
	L	16
L/D=0.8	D	18
	L	14
L/D=1.2	D	15
	L	18
L/D=1.22	D	14
	L	17
L/D=1.5	D	12
	L	18

A series of finite element analyses were carried out to obtain the allowable load capacity of the five bucket foundations in dense sand soil. The dense sand has a friction angle (ϕ') of 40°, a dilation angle (Ψ) of 10°, and a Buoyant unit weight of 11 kN/m^3. The numerical model estimates are shown in Table 5.9 with the estimates from Deb and Singh equations.

Table 5.9: Bucket foundation allowable load capacity at θ=0.5°.

			Very dense sand		
			H (MN)		
			Deb-Singh 2 Parameters	Deb-Singh 3 Parameters	This study FE
L/D=1	D	16	2.74	4.7	3.1
	L	16			
L/D=0.8	D	18	2.14	4.5	3
	L	14			
L/D=1.2	D	15	3.5	5.2	3.6
	L	18			
L/D=1.22	D	14	2.8	4.1	3
	L	17			
L/D=1.5	D	12	2.8	3.5	2.7
	L	18			

As mentioned in section 5.4, the maximum horizontal load that the bucket needs to withstand is 2.3 MN acting at a load eccentricity of 180 m above the bucket foundation cap (Gaertner *et al*., 2020). DNVGL-ST-0437 recommends using a factor of 1.35, thus the factored load becomes 3.2 MN. As expected, the bucket length has a direct impact on resisting the overturning moment which can be noticed in the case of D=15 m and L=18 m the bucket can withstand the 3.2MN in all estimates. However, for the case of D=18 m and L=14 m, the bucket foundation capacity is less than 3.2 MN. From Table 5.9, the bucket size that can resist high moment demand for the IEA 15-Megawatt turbine in dense sand soil is a bucket with a diameter of 17 m and length of 17 m.

Another set of numerical analyses were carried out to size a bucket foundation in a medium dense sand soil. The soil properties for the medium dense sand are a friction angle (ϕ') of 35°, a dilation angle (Ψ) of 5°, and a buoyant unit weight of 9 kN/m^3, medium dense sand parameters are summarized in Table 5.10. The final bucket size in the very dense sand has a diameter of 17m and length of 17m; thus, for the medium dense sand and since the soil is weaker a bucket with a diameter of 20m was chosen initially. Three different aspect ratios were considered in the numerical analyses 0.8,1, and 1.2, as shown in Table 5.11.

Table 5.10: A summary of medium dense sand parameters used in the analysis.

Part	Property	Numerical model
Sand	Friction angle (ϕ')	35°
	Dilation angle (Ψ)	5°
	Poisson's ratio	0.25
	Critical state Friction angle (ϕ')	30°
	Cohesion (c)	1 kN/m^2
	Buoyant unit weight	9 kN/m^3
	Elastic stiffness parameter *k*	400
	Elastic stiffness exponent *n*	0.58

Table 5.11: Bucket sizes considered in the analysis.

L/D=1	D	20
	L	20
L/D=0.8	D	22
	L	18
L/D=1.2	D	18
	L	22

The finite element model estimates are shown in Table 5.12. All three aspect ratios have sufficient capacity to resist the moment demand for the IEA 15-Megawatt turbine. For the bucket with a diameter of 20m and 20m of length, the allowable capacity is 3.7 MN which is more than the maximum horizontal load of 3.2 MN that the bucket needs to withstand. Another observation about the finite element model estimates for the medium dense sand is that both the bucket diameter and length have a similar effect on the bucket capacity while in very dense sand the bucket length has a higher impact on the bucket capacity compared to its diameter.

Table 5.12: Bucket foundation allowable load capacity at θ=0.5°.

Medium dense sand			
			H (MN)
		(m)	
L/D=1	D	20	3.7
	L	20	
L/D=0.8	D	22	3.5
	L	18	
L/D=1.2	D	18	3.75
	L	22	

CHAPTER VI

CONCLUSION

6.1 Caisson Anchors in Sand

The caisson anchor behavior in sand was investigated and the lateral and inclined ultimate capacities of the caisson anchor were estimated by utilizing a three-dimensional finite element model and a plastic limit analysis model. The models were validated by comparing their predictions to centrifuge and lab tests. The numerical model was utilized in the scope of a parametric study to investigate the effect of load attachment depth (Li), Load inclination angle (θ), aspect ratio and soil strength parameters.

For the lateral ultimate capacity of the caisson anchor, the effect of load attachment depth (padeye position) on the ultimate capacity was studied where different attachment depths were considered. The padeye location was optimized to find the optimum load attachment depth that corresponded to the maximum capacity which occurs when the rigid caisson anchor is under translational motion (no rotation). The maximum ultimate lateral load capcity was found to be at Li/Lf of 0.68 which represents the optimum load attahcment depth (L_{opt}).

The effect of the caisson anchor aspect ratio and load inclination angle were also examined. The analysis results showed that load inclination angle (θ) has a major effect on the ultimate load capacity of the caisson anchor even at low load inclination angle values from the horizontal.

The simplified PLA model presented in this study showed a good agreement when compared to measured data from centrifuge and lab tests. In despite of the simplifications in the model components, it is capable of providing a quick estimate of lateral load capacity for the caisson anchor at different load attachment depths and aspect ratios to a sufficient accuracy.

6.2 Multiline Ring Anchor (MRA) in sand

By utilizing a three-dimensional finite element model and a plastic limit analysis model the ultimate lateral capacity of the MRA was estimated and the anchor behavior was examined. The models were validated before being utilized in the scope of a parametric study to investigate the effect of load attachment depth (Li), embedment depth (z/D), and MRA diameter (D).

The effect of load attachment depth on the ultimate capacity was examined where different attachment depths were considered. The maximum ultimate lateral load capcity was found to be at Li/Lf of 0.55 which represents the optimum load attahcment depth (L_{opt}).

The effect of embedment depth (z/D), and MRA diameter (D) were also examined. The analysis results showed that embedment depth is an effective way to improve the lateral ultimate load capacity of the MRA where at deeper embedment depths the higher stress result in a higher anchor capacity.

6.3 Bucket Foundation Design for Fixed Offshore Wind Tower

A bucket foundation was designed in medium and very dense sand that can withstand the overturning moment for the IEA 15-Megawatt turbine. The bucket foundation capacity was estimated by utilizing a three-dimensional finite element model which was validated against measured data from a large-scale field test. After the numerical model was validated, it was used to size the bucket foundation for the IEA 15-Megawatt turbine in medium dense and very dense sand soil.

The technical report “Definition of the IEA 15-Megawatt Offshore Reference Wind” published by National Renewable Energy Laboratory (NREL) was used obtain technical information about the IEA 15-Megawatt turbine. The maximum factored horizontal load that the

bucket needs to withstand is 3.2 MN acting at a load eccentricity of 180 m above the bucket foundation cap (Gaertner *et al*., 2020). In addition to the large-scale field test validation, equations developed by Deb and Singh (2018) to estimate the ultimate and allowable load capacities of bucket foundation were used. For the dense sand, the bucket size that can resist the high moment demand for the IEA 15-Megawatt turbine in is a bucket with a diameter of 17 m and length of 17 m.

For the medium dense sand which has a friction angle (ϕ') of 35°, a dilation angle (Ψ) of 5°, and a buoyant unit weight of 9 kN/m^3, the bucket size needed to be increased to have a sufficient capacity to resist the moment demand for the IEA 15-Megawatt turbine. The numerical model predictions for medium dense sand showed that a bucket foundation with a diameter of 20 m and length of 20m has an adequate allowable capacity to resist the moment demand for the IEA 15-MW.

REFERENCES

ABAQUS. (2014). Abaqus Analysis User Manual, Version 6.14. Dassault Systems Simulia Corp; ABAQUS Inc.

Achmus, M., Akdag, C. T., & Thieken, K. (2013). Load-bearing behavior of suction bucket foundations in sand. Applied Ocean Research, 43. https://doi.org/10.1016/j.apor.2013.09.001

Ahlinhan, M. F., Houehanou, E. C., Koube, B. M., & Sungura, N. (2020). 3D Finite element analyses of suction caisson foundations for offshore wind turbines in drained sand. International Journal of Geotechnical Engineering, 14(1). https://doi.org/10.1080/19386362.2019.1617500

Ahmed, S. S., & Hawlader, B. C. (2015). Numerical Analysis of Inclined Uplift Capacity of Suction Caisson in Sand. International Journal of Offshore and Polar Engineering, 25(2). https://doi.org/10.17736/ijope.2015.cg11

Al-adhadh, A. R. (2013). Interface Friction Angle Between Cohesionless Soil and Different Structural Materials. Dissertations & Theses - Gradworks, October.

Bagheri, P., Yoon, J. C., Park, D., & Kim, J. M. (2019). Numerical analysis of suction bucket foundations used for offshore wind turbines. In Lecture Notes in Civil Engineering (Vol. 18). https://doi.org/10.1007/978-981-13-2306-5_46

Bagheri, P., Son, S. W., & Kim, J. M. (2017). Investigation of the load-bearing capacity of suction caissons used for offshore wind turbines. Applied Ocean Research, 67. https://doi.org/10.1016/j.apor.2017.07.002

Bariker, P., & Raju, K. V. S. B. (2020). Strength and Dilatancy of Sands Mixed with Jute Fibre. Lecture Notes in Civil Engineering, 85. https://doi.org/10.1007/978-981-15-6086-6_6

Bolton, M. D. (1986). The strength and dilatancy of sands. Geotechnique, 36(1). https://doi.org/10.1680/geot.1986.36.1.65

Cecconi, M., Pane, V., Vecchietti, A., & Bellavita, D. (2019). Horizontal capacity of single piles: an extension of Broms' theory for c-ϕ soils. Soils and Foundations, 59(4). https://doi.org/10.1016/j.sandf.2019.01.007

Chari, T. R., & Meyerhof, G. G. (1983). ULTIMATE CAPACITY OF RIGID SINGLE PILES UNDER INCLINED LOADS IN SAND. Canadian Geotechnical Journal, 20(4). https://doi.org/10.1139/t83-091

Choo, Y. W., Kim, D., Park, J. H., Kwak, K., Kim, J. H., & Kim, D. S. (2014). Lateral response of large-diameter monopiles for offshore wind turbines from centrifuge model tests. Geotechnical Testing Journal, 37(1). https://doi.org/10.1520/GTJ20130081

Deb, T. K., & Singh, B. (2018). Response and capacity of monopod caisson foundation under eccentric lateral loads. Marine Georesources and Geotechnology, 36(4), 452–464. https://doi.org/10.1080/1064119X.2017.1330374

DNV/Riso. (2002). Guidelines for Design of Wind Turbines. In Wind Engineering (Vol. 29, Issue 2).

Gaertner, E., Rinker, J., Sethuraman, L., Zahle, F., Anderson, B., Barter, G., Abbas, N., Meng, F., Bortolotti, P., Skrzypinski, W., Scott, G., Feil, R., Bredmose, H., Dykes, K., Shields, M., Allen, C., & Viselli, A. (2020). Definition of the IEA Wind 15-Megawatt Offshore Reference Wind Turbine Technical Report. www.nrel.gov/publications.

Gao, Y., Qiu, Y., Li, B., Li, D., Sha, C., & Zheng, X. (2013). Experimental studies on the anti-uplift behavior of the suction caissons in sand. Applied Ocean Research, 43. https://doi.org/10.1016/j.apor.2013.08.001

Han, F., Ganju, E., Salgado, R., & Prezzi, M. (2018). Effects of Interface Roughness, Particle Geometry, and Gradation on the Sand–Steel Interface Friction Angle. Journal of Geotechnical and Geoenvironmental Engineering, 144(12), 04018096. https://doi.org/10.1061/(asce)gt.1943-5606.0001990

Harte, M., Basu, B., & Nielsen, S. R. K. (2012). Dynamic analysis of wind turbines including soil-structure interaction. Engineering Structures, 45, 509–518. https://doi.org/10.1016/j.engstruct.2012.06.041

Hazzar, L., Karray, M., Bouassida, M., & Hussien, M. N. (2013). Ultimate Lateral Resistance of Piles in Cohesive Soil. DFI Journal - The Journal of the Deep Foundations Institute, 7(1). https://doi.org/10.1179/dfi.2013.005

Hopstad, A. L. H., Argyriadis, K., Manjock, A., Goldsmith, J., & Ronold, K. O. (2018). DNV GL standard for floating wind turbines. ASME 2018 1st International Offshore Wind Technical Conference, IOWTC 2018. https://doi.org/10.1115/IOWTC2018-1035

Houlsby, G. T., Ibsen, L. B., & Byrne, B. W. (2005). Suction caissons for wind turbines. Frontiers in Offshore Geotechnics, ISFOG 2005 - Proceedings of the 1st International Symposium on Frontiers in Offshore Geotechnics. https://doi.org/10.1201/noe0415390637.ch4

Hu, Q., Han, F., Prezzi, M., Salgado, R., & Zhao, M. (2021). Lateral load response of large-diameter monopiles in sand. Geotechnique. https://doi.org/10.1680/jgeot.20.00002

Huang, T., O loughlin, C., Gaudin, C., Tian, Y., & Lu, T. (2020). Drained response of rigid piles in sand under an inclined tensile load. Geotechnique Letters, 10(1). https://doi.org/10.1680/jgele.19.00028

Jang, Y. S., & Kim, Y. S. (2013). Centrifugal model behavior of laterally loaded suction pile in sand. KSCE Journal of Civil Engineering, 17(5). https://doi.org/10.1007/s12205-013-0011-z

Kelly, R. B., Houlsby, G. T., & Byrne, B. W. (2006). Transient vertical loading of model suction caissons in a pressure chamber. Geotechnique, 56(10). https://doi.org/10.1680/geot.2006.56.10.665

Kelly, R. B., Byrne, B. W., Houlsby, G. T., & Martin, C. M. (2004). Tensile loading of model caisson foundations for structures on sand. Proceedings of the International Offshore and Polar Engineering Conference.

Kim, B. T., & Kim, Y. S. (1999). Back analysis for prediction of the behavior of laterally loaded single piles in sand. Electronic Journal of Geotechnical Engineering, 4. https://doi.org/10.1007/bf02823813

Kulhawy, F. H., & Mayne, P. W. (1990). Manual on Estimating Soil Properties for Foundation Design. In Ostigov.

Lee, J., & Aubeny, C. P. (2021). Lateral Undrained Capacity of a Multiline Ring Anchor in Clay. International Journal of Geomechanics, 21(5). https://doi.org/10.1061/(asce)gm.1943-5622.0001995

Li, D. Y., Feng, L. Y., Zhang, Y. K., & Guo, Y. X. (2013). Model tests on lateral bearing capacity and deformation of skirted suction caissons in saturated fine sand under horizontal monotonic loading. Yantu Gongcheng Xuebao/Chinese Journal of Geotechnical Engineering, 35(11).

Li, B., Gao, Y., Sha, C., & Tong, X. (2012). Calculation method for maximum bearing capacity of suction caisson foundation in sand. Dongnan Daxue Xuebao (Ziran Kexue Ban)/Journal of Southeast University (Natural Science Edition), 42(6). https://doi.org/10.3969/j.issn.1001-0505.2012.06.032

Liu, M., Yang, M., & Wang, H. (2014). Bearing behavior of wide-shallow bucket foundation for offshore wind turbines in drained silty sand. Ocean Engineering, 82. https://doi.org/10.1016/j.oceaneng.2014.02.034

Malhotra, S. (n.d.). Selection, Design and Construction of Offshore Wind Turbine Foundations. www.intechopen.com

McCarron, W. O., & Sukumaran, B. (2000). Ultimate capacities of suction caissons and pile elements for deepwater applications. Proceedings of the International Offshore and Polar Engineering Conference, 2.

Negro, V., López-Gutiérrez, J. S., Esteban, M. D., & Matutano, C. (2014). Uncertainties in the design of support structures and foundations for offshore wind turbines. Renewable Energy, 63. https://doi.org/10.1016/j.renene.2013.08.041

Petrasovits, & Award. (1972). Ultimate Lateral Resistance of a Rigid Pile in Cohesionless Soil. Fifth European Conference on Soil Mechanics and Foundation Engineering.

Potyondy, J. G. (1961). Skin friction between various soils and construction materials. Geotechnique, 11(4). https://doi.org/10.1680/geot.1961.11.4.339

Prasad, Y. V. S. N., & Chari, T. R. (1999). Lateral capacity of model rigid piles in cohesionless soils. Soils and Foundations, 39(2). https://doi.org/10.3208/sandf.39.2_21

Ronold, K. O., Landet, E., Hansen, V. L., Jørgensen, E. R., Godvik, M., & Hopstad, A. L. H. (2010). Guideline for offshore floating wind turbine structures. Proceedings of the International Conference on Offshore Mechanics and Arctic Engineering - OMAE, 3. https://doi.org/10.1115/OMAE2010-20344

Roy, K., Hawlader, B., Kenny, S., & Moore, I. (2016). Finite element modeling of lateral pipeline-soil interactions in dense sand. Canadian Geotechnical Journal, 53(3). https://doi.org/10.1139/cgj-2015-0171

Saigal, R. K., Dolan, D., der Kiureghian, A., Camp, T., & Smith, C. E. (2007). An assessment of structural design guidelines for offshore wind turbines. Proceedings of the International Conference on Offshore Mechanics and Arctic Engineering - OMAE, 5. https://doi.org/10.1115/OMAE2007-29629

Simulia. (2017). Abaqus 6.11 Theory Manual. Providence, RI, USA: DS SIMULIA Corp.

Simo, J. C., & Armero, F. (1992). Geometrically non-linear enhanced strain mixed methods and the method of incompatible modes. International Journal for Numerical Methods in Engineering, 33(7). https://doi.org/10.1002/nme.1620330705

Tiwari, B., & Al-Adhadh, A. R. (2014). Influence of Relative Density on Static Soil-Structure Frictional Resistance of Dry and Saturated Sand. Geotechnical and Geological Engineering, 32(2). https://doi.org/10.1007/s10706-013-9723-6

Villalobos, F. A., Byrne, B. W., & Houlsby, G. T. (2009). An experimental study of the drained capacity of suction caisson foundations under monotonic loading for offshore applications. Soils and Foundations, 49(3). https://doi.org/10.3208/sandf.49.477

Wang, H., Lehane, B. M., Bransby, M. F., Wang, L. Z., & Hong, Y. (2020). A simple approach for predicting the ultimate lateral capacity of a rigid pile in sand. Geotechnique Letters, 10(3). https://doi.org/10.1680/jgele.20.00006

Zhang, L. (2009). Nonlinear analysis of laterally loaded rigid piles in cohesionless soil. Computers and Geotechnics, 36(5). https://doi.org/10.1016/j.compgeo.2008.12.001

Zhao, L., Bransby, M. F., & Gaudin, C. (2020). Centrifuge observations on multidirectional loading of a suction caisson in dense sand. Acta Geotechnica, 15(6). https://doi.org/10.1007/s11440-020-00970-4

Zhu, B., Zhang, W., Ying, P., & Chen, Y. (2014). Deflection-Based Bearing Capacity of Suction Caisson Foundations of Offshore Wind Turbines. Journal of Geotechnical and Geoenvironmental Engineering, 140(5). https://doi.org/10.1061/(asce)gt.1943-5606.0001107

APPENDIX A

A.1 Domain analysis study

Sensitivity analyses were carried out to refine the mesh and extend the model domain size to mitigate the effect of boundary conditions and coarse mesh on the caisson anchor capacity. In the domain analysis study, different domain sizes were considered to ensure that the ultimate capacity of the foundation is not influenced by the domain size. Three domain sizes were considered 7D, 9D and 11D as shown in Figure A.1.

The results of the study are shown in Figure A.2. It can be noticed that the domain size effect is insignificant in the ultimate capacity for the three sizes which means the domain size of 7D is large enough.

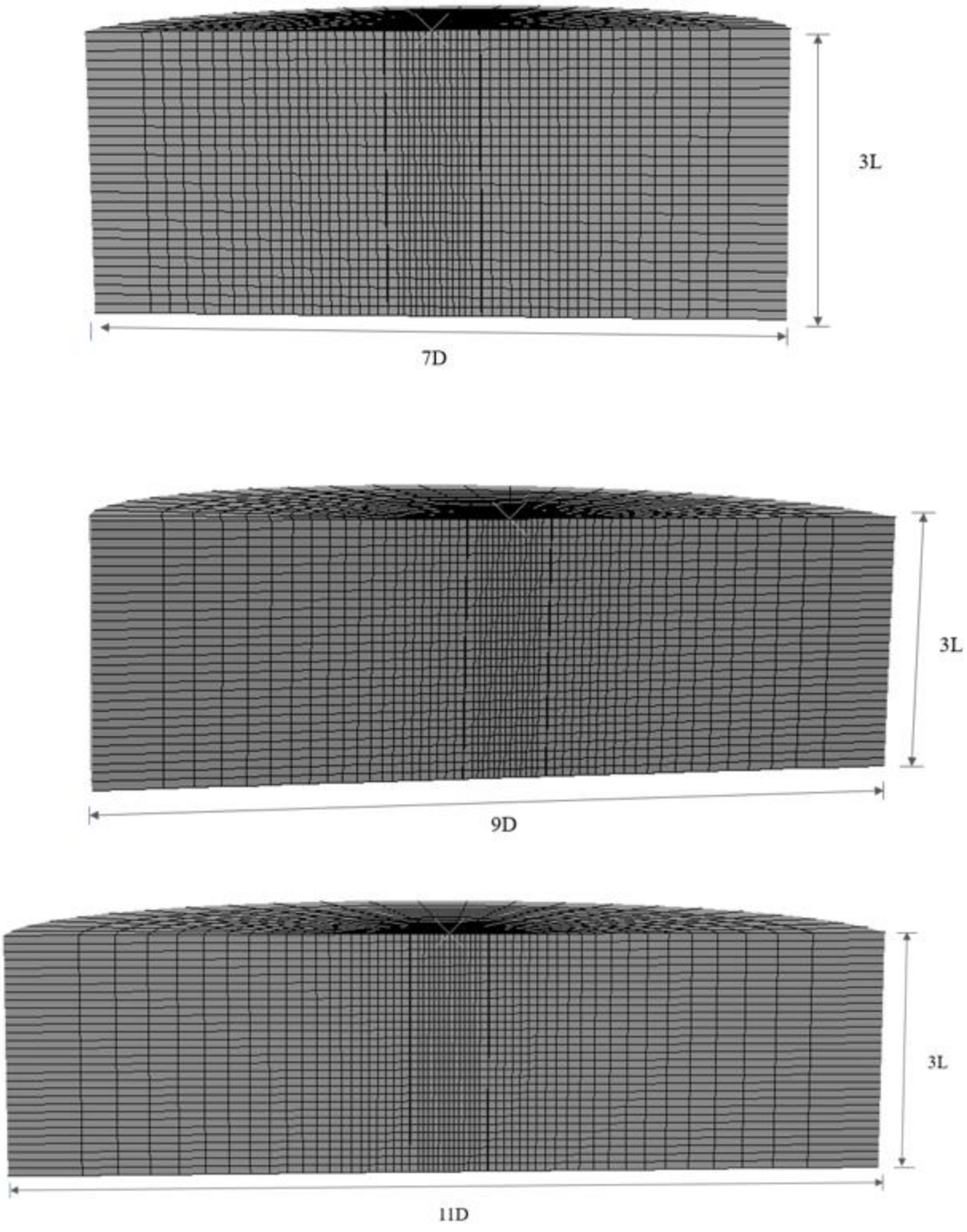

Figure A.1: domain sizes considered in the analysis.

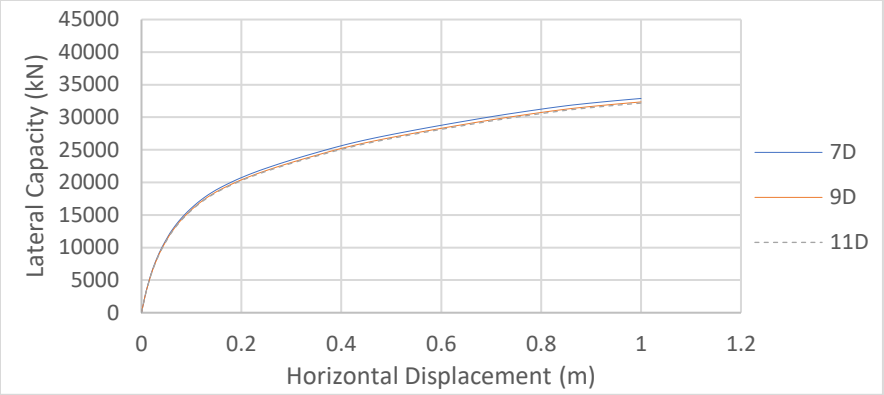

Figure A.2: caisson capacity for the different domain sizes.

A.2 Refinement analysis study

After finalizing the model domain size, the mesh must be refined around the anchor wall from the inside and outside. A mesh with 57600 elements and another mesh with 86400 elements were considered, as shown in Figure A.3.

The refinement study results are shown in Figure A.4. The ultimate capacity has reduced from the coarser mesh considered in A.1 but the difference between the two refined meshes is inconsequential, thus, an element dimension of b/D= 0.05 was used that meets the accuracy and storage requirements.

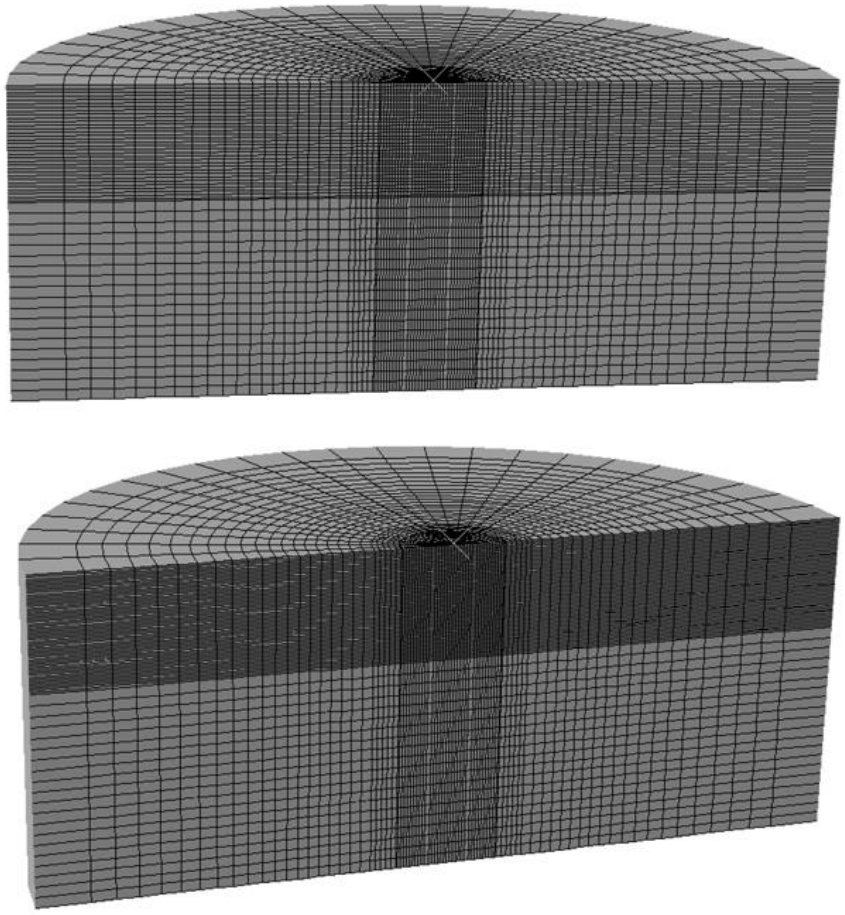

Figure A.3: Refinement study.

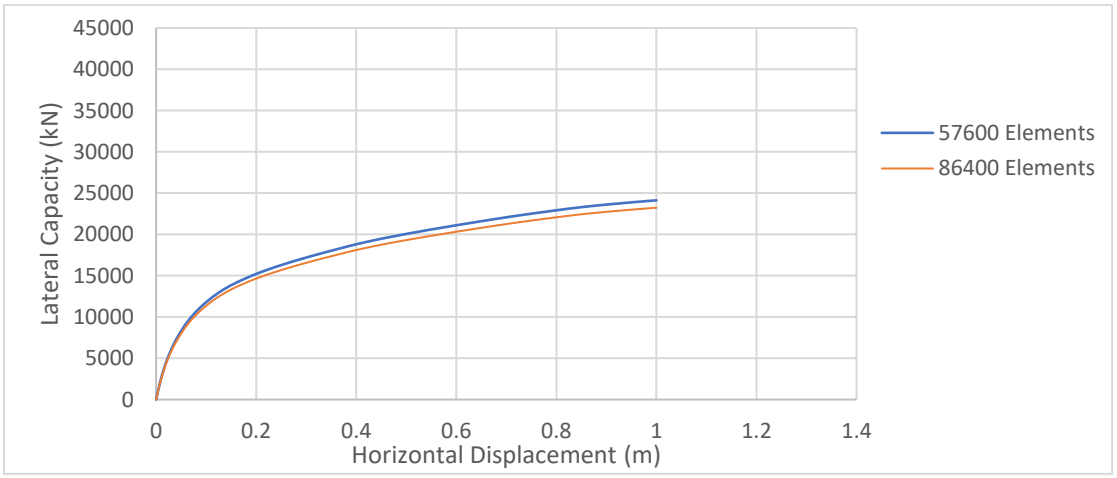

Figure A.4: caisson capacity for the two mesh refinements.